UNIVERSITY OF CALIFORNIA SAN DIEGO

Modeling of $I_{ds} - V_{ds}$ characteristics of short-channel double-gate (DG) MOSFETs

A Dissertation submitted in partial satisfaction of the requirements
for the degree Doctor of Philosophy

in

Electrical Engineering (Applied Physics)

by

Chuyang Hong

Committee in charge:

Professor Yuan Taur, Chair
Professor Prabhakar Bandaru
Professor Chung-Kuan Cheng
Professor Kenji Nomura
Professor Paul K. L. Yu

2022

The Dissertation of Chuyang Hong is approved, and it is acceptable in quality and form for publication on microfilm and electronically.

University of California San Diego

2022

DEDICATION

This dissertation is dedicated to my dear parents (Zhengsheng Hong and Lijuan Guo), my sister (Yanling Hong), lovely nephew (Peihang Zhang) and niece (Yihan Zhang) for their unbounded love.

TABLE OF CONTENTS

DISSERTATION APPROVAL PAGE……iii
DEDICATION iv
TABLE OF CONTENTS v
LIST OF FIGURES vii
LIST OF TABLES xiii
ACKNOWLEDGEMENTS xiv
VITA xv
ABSTRACT OF THE DISSERTATION xvi
CHAPTER 1 INTRODUCTION 1
1.1 SCALE LENGTH MODEL 1
1.2 ANALYTIC POTENTIAL MODEL 3
1.3 DRAIN REGION NON-GCA MODEL 9
1.3 SUMMARY 12
CHAPTER 2 AN ABOVE THRESHOLD MODEL FOR DOUBLE GATE (DG) MOSFETS 13
2.1 SHORT-CHANNEL NON-GCA MODEL FOR LOW DRAIN BIAS CASE 13
2.2 SHORT-CHANNEL NON-GCA MODEL FOR HIGH DRAIN BIAS CASE 27
2.3 VELOCITY SATURATION (N=1) 31
2.4 MATCHING MODEL WITH SOURCE-DRAIN DEPLETION 36
2.5 $n = 2$ VELOCITY SATURATION MODEL 48
2.6 SUMMARY 54
CHAPTER 3 SERIES RESISTANT MODEL FOR DG MOSFETS 56
3.1 SERIES RESISTANT MODEL 56
3.2 INTEL DATA VALIDATION 62
3.3 SUMMARY 64
CHAPTER 4 AN ABOVE THRESHOLD MODEL FOR BULK AND GROUND PLANE MOSFETS 65
4.1 SHORT-CHANNEL NON-GCA MODEL FOR BULK MOSFET 65
4.2 SHORT-CHANNEL NON-GCA MODEL FOR GROUND PLANE MOSFET 79
4.3 SUMMARY 82
CHAPTER 5 NUMERICAL METHODS FOR MODEL DEVELOPMENT 84
5.1 EULER METHOD 84
5.2 FINITE-DIFFERENCE METHOD 89
5.3 NEWTON'S METHOD 92
5.4 EXPERIENCE AND IMPROVEMENT 93
5.5 SUMMARY 95

CHAPTER 6 CONCLUSION AND FUTURE WORK 96
6.1 CONCLUSION 96
6.2 FUTURE WORK 97
REFERENCES 98

LIST OF FIGURES

Figure 1.1: The $I_{ds} - V_{gs}$ characteristics generated by Scale Length model are compared with TCAD simulation……..…..…….3

Figure 1.2: The $I_{ds} - V_{gs}$ characteristics generated by the analytic potential model (i.e., Black lines, denoted as "Analytical solution") for long channel device, compared with TCAD simulation (i.e., Black circles, denoted as "2-D numerical simulation"). …….6

Figure 1.3: The (a) $I_{ds} - V_{gs}$ characteristics and (b) the output conductance $g_{dc} \equiv dI_{ds}/dV_{ds}$, generated by analytic potential model ($n = 1$ velocity saturation). Here $L = 10nm\ and\ V_t = 0.247V$ ...……..……...8

Figure 1.4: The $I_{ds} - V_{gs}$ characteristics generated by drain region non-GCA model ($n = 1$ velocity saturation) are compared with TCAD simulation. $L = 50nm$ ...…….10

Figure 1.5: The output conductance $g_{dc} \equiv dI_{ds}/dV_{ds}$ as a function of channel length L generated by saturation region non-GCA model and compared with TCAD simulation……...…….. 11

Figure 1.6: The potential profile generated by the drain region non-GCA model (D.R.nonGCA) along the channel. The source-drain doping level is $N_{S-D} = 10^{21}cm^{-3}$ ...……..11

Figure 2.1: Schematic cross-section diagram of a undoped/lightly doped DG MOSFET. Assume $t_{si} = 4nm, t_i = 2nm, \varepsilon_{si} = \varepsilon_i = 11.8\varepsilon_0$. The channel length L ranges from $15nm$ to $7nm$. The gate work function is set to be $0.28eV$ below that of the intrinsic silicon so that $V_t = 0.247V$ ...…….…..14

Figure 2.2: Potential ψ in y −direction at a low drain bias voltage, by this short-channel non-GCA model (low drain biases). Here $L = 10nm$ ...……..17

Figure 2.3: Quasi-Fermi Potential $V(y)$ generated by this short-channel non-GCA model (low drain biases) for various V_{gs} given the same $I_{ds} = 1.5E-5A/um$. ……17

Figure 2.4: Comparison of the quasi-Fermi Potential $V(y)$ between the long- and short- channel cases. For long-channel case, no source-drain encroachment is considered. For short-channel case, with source-drain encroachment, the effective length is shortened by ΔL. $V_{gs} = 0.5V$ 19

Figure 2.5: $1/I_{ds}$ as a function of L for various gate voltage V_{gs}. Dash line are generated from the linear extrapolation of the model data, which is plotted as the solid line and symbol. Note the intercept of the line on the x-axis ΔL describes the effect of source-drain encroachment. $V_t = 0.247V$ ....……..20

Figure 2.6: $1/I_{ds}$ versus L generated from the drain region non-GCA model and the low drain short channel non-GCA model, compared with TCAD simulation. $V_t = 0.327V$ ....……...23

Figure 2.7: Comparison of ΔL versus V_{gs} extracted from Scale length model, the low drain short channel non-GCA model and TCAD simulations…….24

Figure 2.8 L_D as a function of gate overdrive $V_{gs} - V_t$…….26

Figure 2.9: The potential profile generated by the short-channel non-GCA model for low drain bias (e.g., $V_{ds} = 0.001V$) and high drain bias (e.g., $V_{ds} = 0.7V$)(constant mobility)……..29

Figure 2.10: Comparison of potential profile $\psi(y)$ for various V_{gs}. The low gate bias curve (i.e., $V_{gs} = 0V$) is generated by the scale length model while the high gate bias curves (i.e., $V_{gs} = 0.3V\ and\ 0.7V$) are generated by this short-channel non-GCA model……30

Figure 2.11: The quasi-Fermi potential profile $V(y)$ along y, generated by the high drain short-channel non-GCA model…….31

Figure 2.12: The $\psi(y)$ curves generated by the high drain short-channel non-GCA model for various V_{gs}. ……..….33

Figure 2.13: The potential profile $\psi(y)$ along y generated by the high drain short-channel non-GCA model for several values of L. …….33

Figure 2.14: Comparison of the potential profiles $\psi(y)$ along y generated by this short-channel non-GCA model and drain region non-GCA model……34

Figure 2.15: Comparison of the quasi-Fermi potential profiles $V(y)$ along y generated by different models……35

Figure 2.16: $I_{ds} - V_{ds}$ characteristics generated by solving the coupled Equations (2.20) and (2.21) with fixed boundary conditions (2.17) are compared to TCAD. The source-drain doping level is $10^{21} cm^{-3}$ ……..35

Figure 2.17: $g_{ds} \equiv dI_{ds}/dV_{ds}$ generated by solving the coupled Equations (2.20) and (2.21) with fixed boundary conditions (2.17) are compared to TCAD. The source-drain doping level is $10^{21} cm^{-3}$ ……..36

Figure 2.18: Potential profile $\psi(y)$ from the source contact to the drain contact generated by this matching model (i.e., with boundary conditions Equations (2.28), (2.31) and (2.32)). The source-drain doping concentration is $N_{S-D} = 10^{20} cm^{-3}$. The source and drain lengths are assumed to be $l_c = 3nm$ ……41

Figure 2.19: Quasi-Fermi Potential profile $V(y)$ from the source contact to the drain contact generated by the matching model with source-drain depletion……42

Figure 2.20: Comparison of Potential profile generated from the model with fixed boundary condition and with matching boundary condition. The source-drain doping levels are $N_{S-D} = 10^{21}$……...43

Figure 2.21: Comparison of quasi-Fermi Potential profile generated from the model with fixed boundary condition and with matching boundary condition. The source-drain doping levels are $N_{S-D} = 10^{21} cm^{-3}$ ……...43

Figure 2.22: Comparison of Potential profile generated from the model with fixed boundary condition and with matching boundary condition. The source-drain doping levels are $N_{S-D} = 10^{20} cm^{-3}$ ……44

Figure 2.23: Comparison of quasi-Fermi Potential profile generated from the model with fixed boundary condition and with matching boundary condition. The source-drain doping levels are $N_{S-D} = 10^{20} cm^{-3}$ ……...45

Figure 2.24: Comparison of $I_{ds} - V_{ds}$ generated from the model with fixed boundary condition and with matching boundary condition. The source-drain doping levels are $N_{S-D} = 10^{21} cm^{-3}$ and $V_{gs} = 0.7V$ ....……...46

Figure 2.25: Comparison of $I_{ds} - V_{ds}$ generated from the model with fixed boundary condition and with matching boundary condition. The source-drain doping levels are $N_{S-D} = 10^{20} cm^{-3} and$ $V_{gs} = 0.7V$. ……..46

Figure 2.26: $I_{ds} - V_{ds}$ characteristics generated by this matching model with the source-drain depletion, compared with TCAD……..47

Figure 2.27: $g_{ds} \equiv dI_{ds}/dV_{ds}$ generated by this matching model with the source-drain depletion, compared with TCAD……..47

Figure 2.28: $I_{ds} - V_{gs}$ characteristics generated by this matching model for various channel lengths, compared with TCAD. $V_{ds} = 0.7V$…….48

Figure 2.29: Comparison of Potential profile $\psi(y)$ generated from the $n = 1$ and $n = 2$ velocity saturation models. $N_{S-D} = 10^{20} cm^{-3}$. $V_{gs} = V_{ds} = 0.7V$ ....……...52

Figure 2.30: Comparison of quasi-Fermi Potential profile $V(y)$ generated from the $n = 1$ and $n = 2$ velocity saturation models. $N_{S-D} = 10^{20} cm^{-3}$. $V_{gs} = V_{ds} = 0.7V$ ....……53

Figure 2.31: $I_{ds} - V_{ds}$ characteristics generated by the $n = 2$ model (matching model with S-D depletion) are compared with TCAD simulations……..……..54

Figure 3.1: Schematic diagram showing the equivalent circuit of DG MOSFET with the source-drain series resistant……..57

Figure 3.2: $I_{ds} - V_{ds}$ characteristics generated by the short-channel non-GCA model with considering various R_{sd}…….60

Figure 3.3: $I_{ds} - V_{ds}$ characteristics generated by the short-channel non-GCA model are verified by Intel 14nm FinFET data……..64

Figure 4.1: Schematic of bulk MOSFET cross section. $V_{bs} = 0$ ....……...66

Figure 4.2: Comparison of $Q_i(V_{gs})$ generated by the charge sheet model, modified charge sheet model and TCAD simulations for device with a long channel length $L = 500nm$. $V_{ds} = 0.001V$……...……...…...68

Figure 4.3: Comparison of $I_{ds} - V_{gs}$ generated by the charge sheet model, modified charge sheet model and TCAD simulations for device with a long channel length $L = 1\mu m$. $V_{gs} = 1.2V$……...69

Figure 4.4: Comparison of $Q_i(V)$ generated by the modified charge sheet model, Equation (4.2) with C_{inv}'' and V_t'' extracted from Equations (4.11)-(4.12) and from Equations (4.15)-(4.16). $V_{gs} = 1.2V$……71

Figure 4.5: Comparison of $Q_i(V_{gs})$ generated by the modified charge sheet model, Equation (4.2) with C_{inv}'' and V_t'' extracted from Equations (4.15)-(4.16) at $V_{gs} = 1.2V$……..72

Figure 4.6: $I_{ds} - V_{ds}$ characteristics for MOSFETs generated by TCAD simulation with different junction depth x_j for various channel length L. $V_{gs} = 1.2V$ ...……..74

Figure 4.7: $I_{ds} - V_{ds}$ characteristics for MOSFETs generated by the modified charge sheet model, short-channel non-GCA model and TCAD simulation. $L = 1\mu m$ ...……75

Figure 4.8: $I_{ds} - V_{ds}$ characteristics for MOSFETs generated by the short-channel non-GCA model (n=1) and TCAD simulation for (a) $L = 1\mu m$, (b) $L = 200nm$, (c) $L = 100nm$ and (d) $L = 50nm$. $d_{si} = x_j = 25nm$ ...……..77

Figure 4.9: Comparison of $I_{ds} - V_{ds}$ characteristics generated by TCAD simulations and models with different d_{si}……..79

Figure 4.10: Schematic of ground plane MOSFET cross section. $V_{bs} = 0$ ...……80

Figure 4.11: Comparison of $I_{ds} - V_{ds}$ characteristics generated by TCAD simulations for bulk and ground plane MOSFETs. Here different work function values are set for them so that they have the same $I_{ds} - V_{ds}$ characteristics for a long channel length……81

Figure 4.12: $I_{ds} - V_{ds}$ characteristics generated by the short-channel non-GCA model are compared with TCAD simulations for the ground plane MOSFET……..82

Figure 5.1: $\psi(x)$ solved from Equation (5.8) using Euler method is compared with analytical solution. $\psi_0 = 0.5V$ 88

LIST OF TABLES

Table 2.1: Comparison between the Debye length L_D and ΔL value in Figure 2.7……26

Table 3.1: Comparison of I_{ds} from models with and without R_{sd} for various V_{gs} and V_{ds}. Here $R_s = R_d = 50\Omega - \mu m$ ....…….….60

Table 3.2: Comparison of I_{ds} from models with and without R_{sd} for various L……62

Table 3.3: Parameters used for fitting Intel 14nm FinFET data……..63

Table 4.1: $C_{inv}{}''$ and $V_t{}''$ extracted from the $Q_i(V)$ curves which are generated by the modified charge-sheet model.……...72

ACKNOWLEDGEMENTS

I would like to express my deepest gratitude to my advisor, Prof. Yuan Taur. Without his tremendous help and enlightening guidance during the past several years, I am unable to reach this milestone in my life. He is a great expert with 50 years' research experience and knowledge in the field of semiconductor physics. His deep insight and vast knowledge benefit me throughout the whole PhD study. The way he thinks and the attitude he has in pursuing the truth significantly influence me. I can take great advantage of all I learn from him for my whole life.

Tons of thanks should be given to my committee members, Prof. Paul K. L. Yu, Prof. Kenji Nomura, Prof. Prabhakar Bandaru and Prof. Chung-Kuan Cheng for taking their time to serve as committee members to review my dissertation and give me valuable comments.

Many thanks to my friends in UCSD, in particular, Mei-hua Hsu, Zhongjie Ren, Zhaoxin Hu, Yuguang Lin, Qinru Li, Chau Miu, Qingqing Wang, Florence Li and Suzie Li. The friendship means a lot to me.

Finally, and most importantly, I want to express my sincere gratitude to my parents and my sister for their endless love and support. To help me get my education, they sacrificed so much. This dissertation is dedicated to them.

Chapter 2, in full, is a reprint of the material as it appears in "An Above Threshold Model for Short-Channel DG MOSFETs," by David Chuyang Hong and Yuan Taur, IEEE Trans. Electron Devices, Jul. 2021. The dissertation author was the primary investigator and author of this paper.

VITA

2013 Bachelor of Engineering in Microelectronics, Guangdong University of Technology

2016 Master of Natural Science in Microelectronics and Solid State Electronics, Peking University, Shenzhen Graduate School

2022 Doctor of Philosophy in Electrical Engineering(Applied Physics), University of California San Diego

PUBLICATIONS

[1] **D. C. Hong** and Y. Taur, "An Above Threshold Model for Short-Channel DG MOSFETs," IEEE Trans. Electron Devices, vol. 68, no. 8, pp. 3734-3739, Jul. 2021.

[2] E. M. Su, **D. C. Hong**, S. Cristoloveanu and Y. Taur, "Effects of BOX thickness, silicon thickness, and backgate bias on SCE of ET-SOI MOSFETs," Microelectronic Engineering, vol. 238, pp. 111506, Jan. 2021.

FIELD OF STUDY

Major Field: Electrical Engineering
Focused Field: Applied Physics/Engineering Physics

ABSTRACT OF THE DISSERTATION

Modeling of $I_{ds} - V_{ds}$ characteristics of short-channel double-gate (DG) MOSFETs

by

Chuyang Hong

Doctor of Philosophy in Electrical Engineering (Applied Physics)

University of California San Diego, 2022

Professor Yuan Taur, Chair

In this dissertation, an above-threshold $I - V$ model framework is constructed for short-channel double-gate (DG) MOSFETs. This is a non-GCA model that takes the effect of the lateral field gradient into account. By applying the model to the low drain and high drain bias cases, useful physical insights are obtained. At low-drain bias voltages, the effect of encroachment of the source-drain bands into the channel (i.e., the source-drain encroachment

effect) appears as a reduction of the channel resistance, which is gate-voltage dependent. This effect is stronger in subthreshold region and weaker in above threshold region. At high-drain bias voltages, a point of "virtual cathode" (or minimum potential) at a small distance from the source is caused by the intersection of source band encroachment with the gate-controlled channel potential. This is in contrast to the drain region non-GCA model which is only applicable to device with a channel length of $L > 20nm$. The current model is also extended to incorporate the effect of band bending caused by the depletion of carriers in the source and drain regions and the source-drain series resistance effect. By implementing the velocity saturation in the current continuity equation, the $I_{ds} - V_{ds}$ and $I_{ds} - V_{gs}$ characteristics generated by the model are verified by TCAD simulations.

Moreover, the model is applied to the bulk and the ground plane MOSFETs. It shows that as an additional parameter affecting short-channel effect of bulk MOSFETs, the junction depth of the source and drain is not taken into account in the short-channel non-GCA model for DG MOSFETs. The charge sheet model is not accurate enough to fit parameters like C_{inv}, V_t for long channel MOSFETs and a modified charge sheet mode is developed. Moreover, the short-channel non-GCA model tends to underestimate the short-channel effect for practical source/drain junction depths like $x_j = 25nm$.

CHAPTER 1 INTRODUCTION

In the past decades, plenty of studies have been carried out to model the $I-V$ characteristics of double-gate (DG) [1]–[16]and bulk ground plane MOSFETs [17]–[30]. By approximately solving the potential or charge density profile from the Poisson's equation, those models achieve good accuracy [1], [16], [31]–[35]. For example, the scale length model[32], [36]–[38] employs the superposition technology to solve the two-dimensional Poisson's equation where the mobile charge term is neglected. It is only valid in the subthreshold region since the superposition is disallowed for the nonlinear Poisson's equation with mobile charge term in the above threshold region. The analytic potential model[1], [2] derives an analytical solution to the one-dimensional Poisson's equation based on the gradual channel approximation, which only works for the long channel device. In this chapter, we will briefly review three popular models focusing on DG MOSFETs and discuss their approximations and weaknesses.

1.1 Scale Length Model

In the scale length model (SLM)[32], [37], [38], the whole potential profile is divided into three parts: ψ^+ for the top oxide regions, ψ for the Si channel region and ψ^- for the bottom oxide region. They are governed by the different Poisson's equation in different regions[32]:

$$\frac{\partial^2\psi^{\pm}}{\partial x^2}+\frac{\partial^2\psi^{\pm}}{\partial y^2}=0 \tag{1.1}$$

$$\frac{\partial^2\psi}{\partial x^2}+\frac{\partial^2\psi}{\partial y^2}=\frac{q}{\varepsilon_{si}}N_a \tag{1.2}$$

where N_a is the p-type doping level of the channel. Those three parts are connected by the condition of the usual continuity of potential and normal displacement. Note that Equation (1.2) is a linear partial differential equation, which can be solved by using the superposition technology [38]:

$$\psi(x,y)=V_{gs}-\emptyset_{mi}-\frac{qN_at_{si}t_i}{2\varepsilon_i}-\frac{qN_a}{2\varepsilon_{si}}\left[\left(\frac{t_{si}}{2}\right)^2-x^2\right]$$
$$+\sum_{n=1}^{\infty}s_n\frac{\sinh[k_n(L-y)]}{\sinh(k_nL)}\cos(k_nx)+\sum_{n=1}^{\infty}d_n\frac{\sinh(k_ny)}{\sinh(k_nL)}\cos(k_nx) \tag{1.3}$$

where s_n, d_n and k_n are parameters that can be estimated by the orthogonality relation and potential and normal displacement continuity conditions. The total charge density per area is given as:

$$Q_t(y)=q\int_{-\frac{t_{si}}{2}}^{\frac{t_{si}}{2}}n_ie^{\frac{q[\psi(x,y)-V(y)]}{kT}}dx \tag{1.4}$$

For given V_{gs}, $\psi(x,y)$ is $x-$ and $y-$ dependent, indicating $Q_t(y)$ is $V_{gs}-$ and $y-$ dependent.

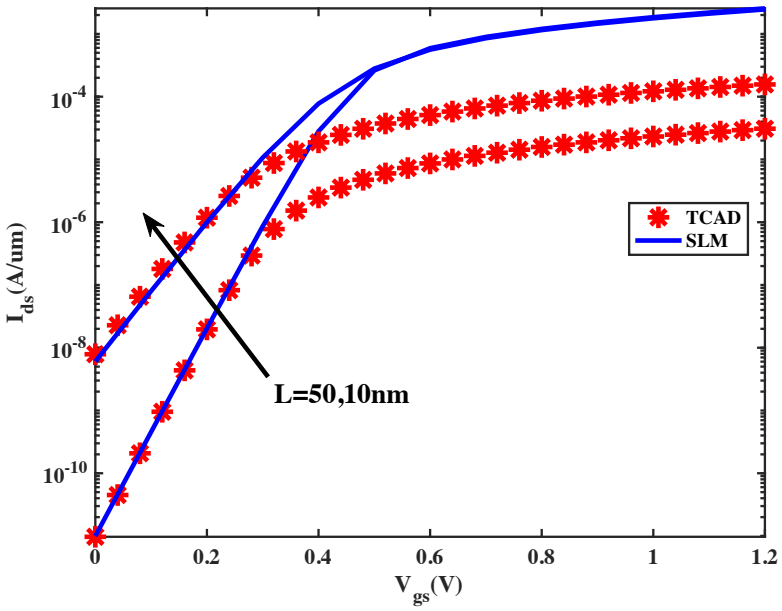

Figure 1.1: The $I_{ds} - V_{gs}$ characteristics generated by the scale length model[38] are compared with TCAD simulation.

Figure 1.1 shows the $I_{ds} - V_{gs}$ characteristics generated by the scale length model are compared with TCAD simulation. It is obvious that SLM is accurate in subthreshold region but large discrepancy is observed on the above threshold region. This is because the mobile charge term neglected in Equation (1.2) plays an important role in above threshold region[39].

1.2 Analytic Potential Model

For a undoped/lightly doped double gate (DG)/bulk MOSFET, the 2-dimensional Poisson's equation is given as:

$$\frac{\partial(\varepsilon_{si}E_x)}{\partial x}+\frac{\partial(\varepsilon_{si}E_y)}{\partial y}=\varepsilon_{si}\frac{\partial^2\psi}{\partial x^2}+\varepsilon_{si}\frac{\partial^2\psi}{\partial y^2}=qn(x,y) \tag{1.5}$$

where ψ is the potential and n is the carrier density. Equation (1.5) shows the total charge density $qn(x,y)$ consists of two parts: one is the charge part induced by the vertical field from the gate terminal (i.e., the first term of LHS) and the other is the charge part caused by the lateral field from the source and drain terminals (i.e., the second term of LHS)[40]–[43]. The gradual channel approximation (GCA) assumes that the vertical field (perpendicular to the channel) induced charge density is much greater than the lateral field (along the channel) induced charge density (i.e., $\varepsilon_{si}\frac{\partial^2\psi}{\partial x^2}\gg\varepsilon_{si}\frac{\partial^2\psi}{\partial y^2}$) so that the second term of Equation (1.5) is negligible[43]–[45]. According to GCA, the Poisson's equation can be simplified as:

$$\frac{d^2\psi}{dx^2}=\frac{q}{\varepsilon_{si}}n_i e^{q(\psi-V)/kT} \tag{1.6}$$

Unlike the scale length model, the analytic potential model is able to work in the above threshold region since the mobile charge term is kept[1], [2]. Equation (1.6) is a one-dimensional equation, of which the analytic solution can be gotten as[1][33]:

$$\psi(x)=V-\frac{2kT}{q}\ln\left[\frac{t_{si}}{2\beta}\sqrt{\frac{q^2n_i}{2\varepsilon_{si}kT}}cos\left(\frac{2\beta x}{t_{si}}\right)\right] \tag{1.7}$$

The charge density per area is given as[2]:

$$Q_t = 8\frac{kT}{q}\frac{\varepsilon_{si}}{t_{si}}\beta tan\beta \tag{1.8}$$

where β is estimated by:

$$V_{gs} - V_t - V = \frac{2kT}{q}\left[ln\beta - \ln(cos\beta) + 2\frac{\varepsilon_{si}t_i}{\varepsilon_i t_{si}}\beta tan\beta\right] \tag{1.9}$$

We can see that Q_t here is $V_{gs}-$ dependent but not explicitly $y-$ dependent. The drain current I_{ds} is estimated by carrying out Pao-Sah's integral[46]:

$$I_{ds} = \mu_{eff}\frac{W}{L}\frac{4\varepsilon_{si}}{t_{si}}(\frac{2kT}{q})^2\left[\beta tan\beta - \frac{\beta^2}{2} + \frac{\varepsilon_{si}t_i}{\varepsilon_i t_{si}}\beta^2 tan^2\beta\right]|_{\beta_d}^{\beta_s} \tag{1.10}$$

where μ_{eff} is the effective mobility.

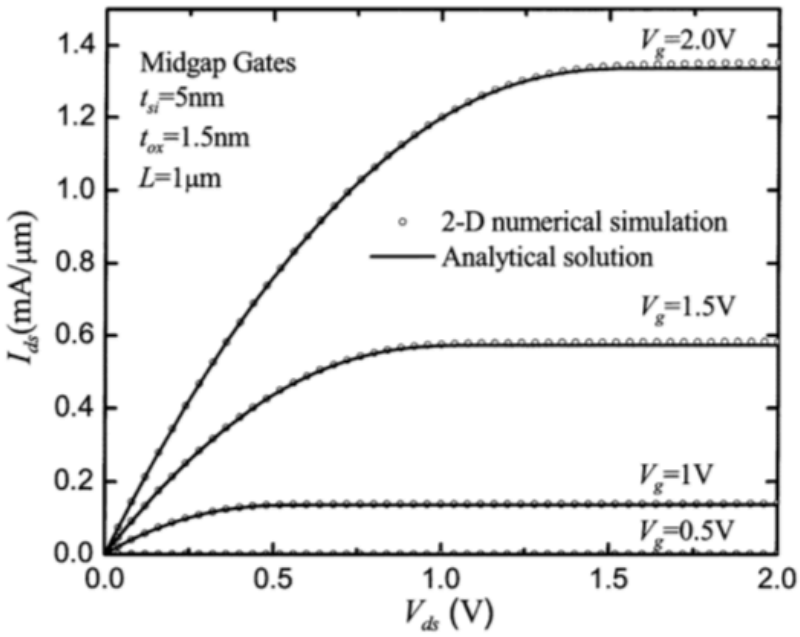

Figure 1.2: The $I_{ds} - V_{gs}$ characteristics generated by the analytic potential model (i.e., Black lines, denoted as "Analytical solution") for long channel device, compared with TCAD simulation (i.e., Black circles, denoted as "2-D numerical simulation")[2].

Figure 1.2 shows the $I_{ds} - V_{ds}$ characteristics generated by the analytic potential model is in consistent with the TCAD simulation for a long channel device (e.g., $L = 1\mu m$). As we discussed above, the gradual channel approximation (GCA) neglects the effect of lateral field gradient on carrier density in Poisson's equation[47]. It is unable to describe the two-dimensional nature of the field in the channel, which plays an important role in saturation region and for a short channel device [48], [49].

Figure 1.3 shows that the $I_{ds} - V_{ds}$ characteristics and the conduction $g_{dc} \equiv dI_{ds}/dV_{ds}$ generated by the analytic potential model. Here the $n = 1$ velocity saturation model is considered, i.e.:

$$I_{ds} = \frac{\mu_{eff} W \int_0^{V_{ds}} Q_i\,(V) dV}{L + (\mu_{eff}/v_{sat}) V_{ds}} \tag{1.11}$$

where $Q_i(V)$ as a function of V is calculated from Equations (1.8) and (1.9). In Figure 1.3, negative slope is also observed in the saturation region of each $I_{ds} - V_{ds}$ characteristic. This confirms that the drain current I_{ds} is underestimated by the GCA in the saturation region.

Hence, the analytic potential model works well only for long channel device with constant mobility assumption, but it may be not accurate in velocity saturation region and for short channel device.

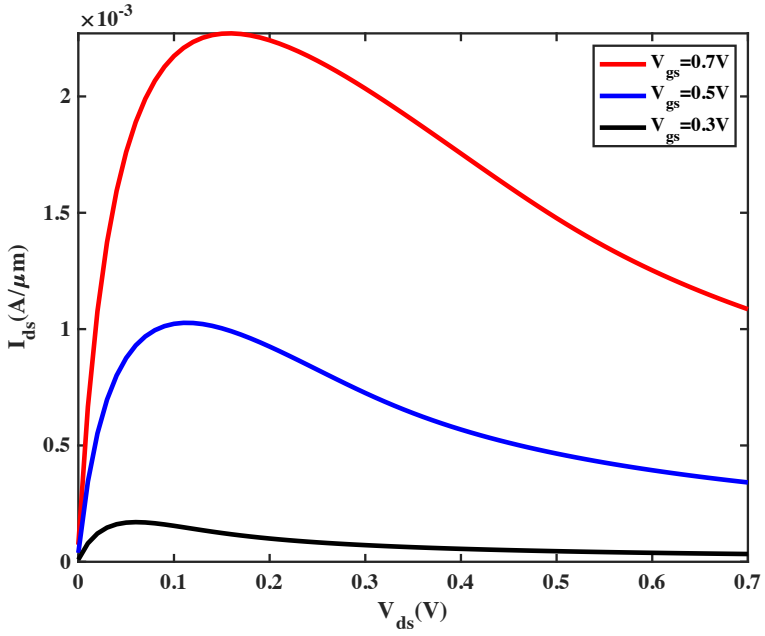

(a)

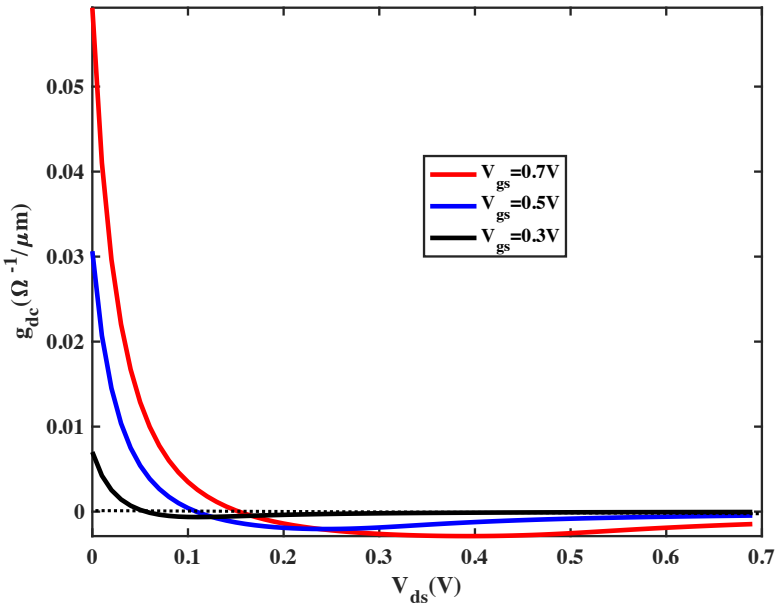

(b)

Figure 1.3: The (a) $I_{ds} - V_{gs}$ characteristics and (b) the output conductance $g_{dc} \equiv dI_{ds}/dV_{ds}$, generated by analytic potential model ($n = 1$ velocity saturation). Here $L = 10nm\ and\ V_t = 0.247V$.

1.3 Drain Region Non-GCA Model

To fix this problem of neglecting the effect of $\frac{\partial^2\psi}{\partial y^2}$ term in the Poisson's equation due to the gradual-channel approximation, an drain region non-GCA model[47], [50] is developed recently. In this model, the mobile charge density per area is given as[47]:

$$Q_t = Q_i + \Delta Q_i = 2C_{inv}\left(V_{gs} - V_t - V\right) + \varepsilon_{si}t_{si}\frac{d^2V}{dy^2} \tag{1.12}$$

where C_{inv} will be given by Equation (2.2) in Section 2. It contains two parts: one is the gate-induced charge density $Q_i = 2C_{inv}\left(V_{gs} - V_t - V\right)$[43], [50]; the other part is the additional charge density term that accounts for the effect of the lateral field gradient on carrier density $\Delta Q_i = \varepsilon_{si}t_{si}\frac{d^2V}{dy^2}$. The Q_t is more accurate since it is $V_{gs}-$ and $y-$ dependent, compared with the GCA model discussed before. The current continuity equation for $n = 1$ velocity saturation is given as[50]:

$$I_{ds} = \frac{\mu_{eff}W\left(Q_i + \varepsilon_{si}t_{si}\frac{d^2V}{dy^2}\right)\frac{dV}{dy}}{1 + \left(\frac{\mu_{eff}}{v_{sat}}\right)\frac{dV}{dy}} \tag{1.13}$$

For given I_{ds}, Equation (1.13) can be solved to get $V(y)$ as a function of y so $V_{ds} = V(L)$.

Figure 1.4 shows that the $I_{ds} - V_{ds}$ characteristics generated by the drain region non-GCA model is verified by the TCAD simulation for intermediate channel device. In Figure 1.5, the output conduction generated by the saturation region non-GCA model is compared with TCAD simulation for various channel length L. It shows that the drain region non-GCA model is accurate for intermediate channel length $L \geq 2\lambda,\ (e.g.,\ L \geq 20nm)$, where $\lambda = t_{si} + 2t_i$ is the scale length[38]. For a shorter channel, it no longer works since the short channel effect become prominent.

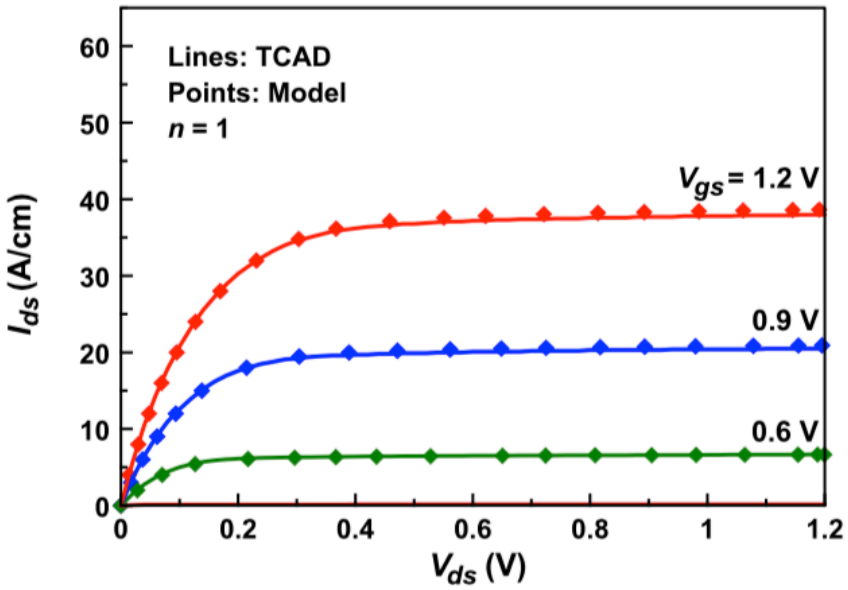

Figure 1.4: The $I_{ds} - V_{gs}$ characteristics generated by the drain region non-GCA model ($n = 1$ velocity saturation) are compared with TCAD simulation[50]. $L = 50nm$.

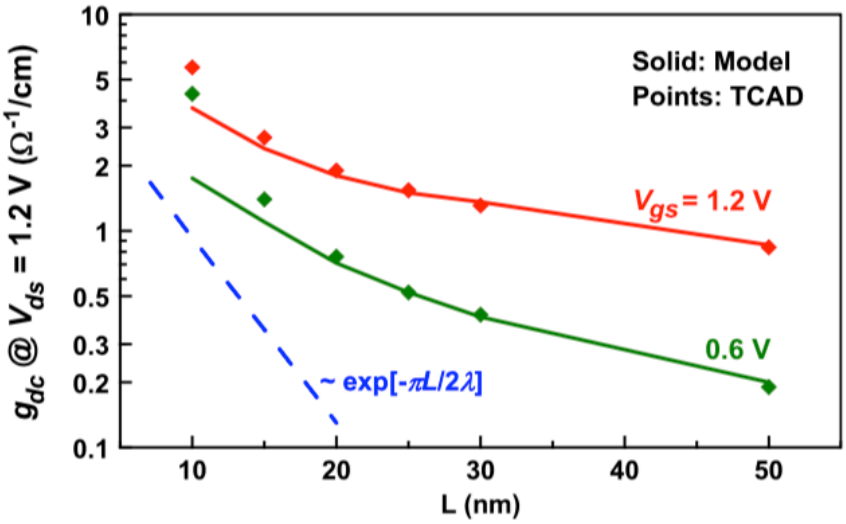

Figure 1.5: The output conductance $g_{dc} \equiv dI_{ds}/dV_{ds}$ as a function of channel length L generated by the drain region non-GCA model and compared with TCAD simulation[50].

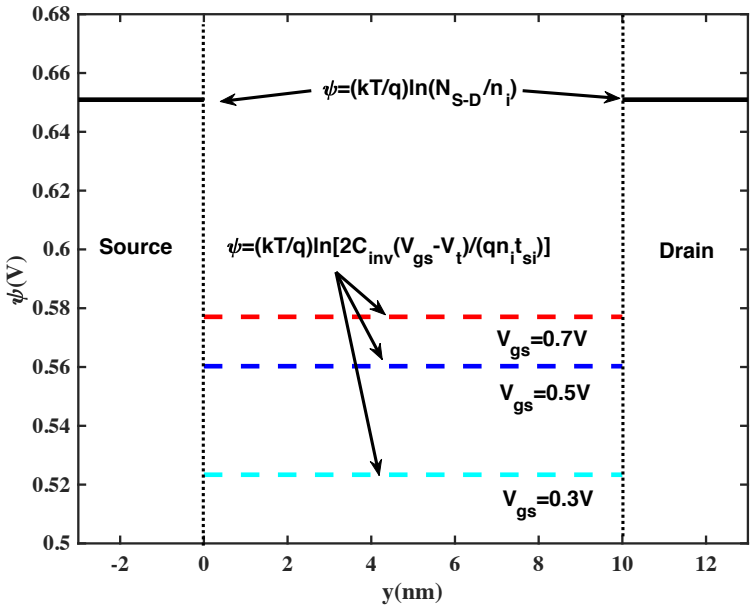

Figure 1.6: The potential profile generated by the drain region non-GCA model (D. R. non-GCA) [47], [50] along the channel. The source-drain doping level is $N_{S-D} = 10^{21} cm^{-3}$.

Figure 1.6 shows the depth averaged potential profile, $\varphi = (kT/q)\ln[2C_{inv}(V_{gs} - V_t)/(qn_i t_{si})]$, generated by the drain region non-GCA model along the channel. Note that the

potential $\psi = (kT/q)\ln(N_{S-D}/n_i)$ is independent of V_{gs} in the source and drain regions, while ψ generated by the drain region non-GCA model for the channel region is a function of V_{gs}. The band (i.e., ψ) and mobile charge density take the channel values at $y = 0\ and\ L$ right away, it is unphysical because of the discontinuity with those in the source-drain region. Since the drain region non-GCA model doesn't take the source-drain encroachment into account, it works only for the intermediate channel device above threshold region, but not for short channel device.

1.3 Summary

In this chapter, we briefly reviewed three popular models for DG MOSFET. The Scale length model neglects the mobile charge term in Poisson's equation, so it is accurate in the subthreshold region, but not for the above threshold region; the analytic potential model employs the gradual-channel approximation, so it works only for the long channel device with constant mobility assumption; the drain region non-GCA model fixed the weakness of GCA model by incorporating the effect of the lateral field gradient on the carrier density, but it doesn't take the source-drain encroachment into account and it works only for the intermediate channel device. In sum, no existing model works for short-channel device above threshold.

CHAPTER 2 AN ABOVE THRESHOLD MODEL FOR DOUBLE GATE (DG) MOSFETS

In this chapter, an above threshold current-voltage model for short channel DG MOSFETs is presented. In order to account for the contribution to the carrier density from the encroachment of the source-drain bands into the channel, a non-GCA term is incorporated in the model. We can gain interesting physical insights from the model: (1) At low-drain bias case, the reduction of the channel resistance is gate-voltage dependent, indicating the short-channel effects are weaker at low gate overdrives and stronger at high gate overdrives. (2) At high-drain bias case, a point of virtual cathode is observed at a short distance from the source side. This is caused by the intersection of the source band encroachment with the channel potential controlled by the gate terminal. (3) In short-channel devices at the scale of $L = 10nm$, a strong effect from the depletion in the source and drain sides to the channel potential is found. By taking the source/drain encroachment effect (short channel effect) into account, our model is constructed to generate the $I_{ds} - V_{ds}$ and $I_{ds} - V_{gs}$ characteristics, which are verified by TCAD simulations.

2.1 Short-Channel Non-GCA Model for Low Drain Bias Case

The schematic cross-section diagram of a undoped/lightly doped DG MOSFET is shown in Figure 2.1.

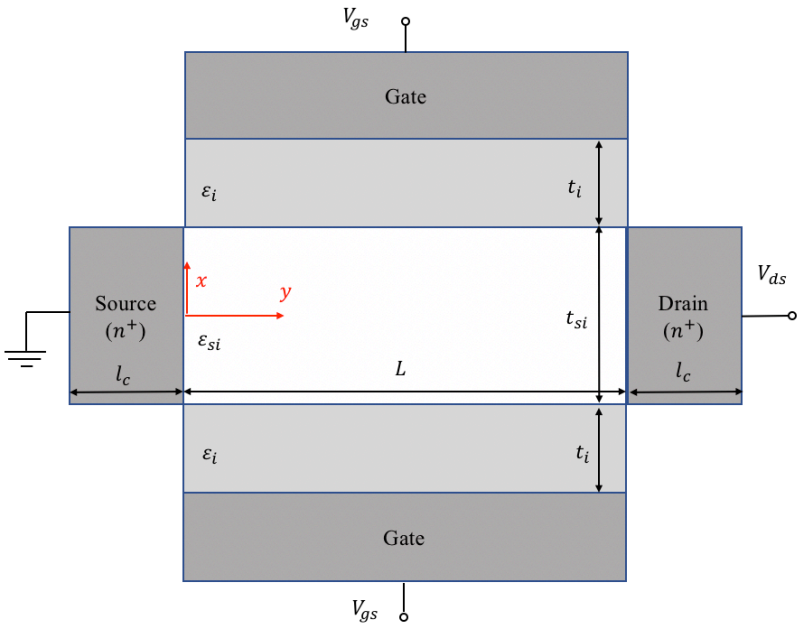

Figure 2.1: Schematic cross-section diagram of a undoped/lightly doped DG MOSFET. Assume $t_{si} = 4nm, t_i = 2nm, \varepsilon_{si} = \varepsilon_i = 11.8\varepsilon_0$. The channel length L ranges from $15nm$ to $7nm$. The gate work function is set to be $0.28eV$ below that of the intrinsic silicon so that $V_t = 0.247V$.

The 2-D Poisson's equation for undoped/lightly doped DG MOSFET is given as:

$$\frac{\partial^2 \psi}{\partial x^2} + \frac{\partial^2 \psi}{\partial y^2} = \frac{q}{\varepsilon_{si}} n_i e^{\frac{q(\psi - V)}{kT}} \tag{2.1}$$

where ψ is the potential and V is the quasi-Fermi potential. Under the gradual channel approximation (GCA), Equation (2.1) can be simplified to Equation (1.6), an ordinary differential equation in the $x-$ direction. Equation (1.6) is widely used in long channel DG MOSFETs modeling although the curvature of potential in the $y-$ direction is neglected [44], [51]–[54]. As discussed in Chapter 1, a simple form of the gate induced inversion charge density per unit area is

given as $Q_i = 2C_{inv}(V_{gs} - V_t - V)$ where C_{inv} takes into account the effect of inversion layer capacitor, which is less than the oxide capacity $C_{ox} = \frac{\varepsilon_i}{t_i}$. C_{inv} is slightly dependent on V_{gs} [50]:

$$\frac{C_{inv}}{C_{ox}} = \frac{2r\beta_s tan\beta_s}{ln\beta_s - \ln(cos\beta_s) + 2r\beta_s tan\beta_s} \tag{2.2}$$

where $r = \varepsilon_{si}t_i/\varepsilon_i t_{si}$ and β_s is the value of β at $V = 0$ from Equation (1.9). We can estimate the gate-induced charge effect by averaging Q_i into a volume charge density $\frac{Q_i}{t_{si}}$:

$$\frac{d^2\psi}{dx^2} = \frac{2C_{inv}(V_{gs} - V_t - V)}{\varepsilon_{si}t_{si}} \tag{2.3}$$

Note that the $x-$dependence on the RHS of Equation (2.3) is removed under this smoothing approximation. A non-GCA model in the $y-$direction can be developed by inserting Equation (2.3) back into (2.1):

$$\frac{d^2\psi}{dy^2} = \frac{q}{\varepsilon_{si}} n_i e^{q(\psi - V)/kT} - \frac{2C_{inv}(V_{gs} - V_t - V)}{\varepsilon_{si}t_{si}} \tag{2.4}$$

Here we use the solution to the one-dimensional ordinary differential equation in the gate direction to form a one-dimensional ordinary differential equation in the channel direction. Equation (2.4) describes the $y-$dependence of ψ, which is applicable to the short-channel DG MOSFETs.

To solve Equation (2.4), we have to couple it with the current continuity equation for $V(y)$ in general. Let's first consider a low drain bias case (e.g., $V_{ds} \ll kT/q$), where V is negligible so that Equation (2.4) can be simplified:

$$\frac{d^2\psi}{dy^2} = \frac{q}{\varepsilon_{si}} n_i e^{q\psi/kT} - \frac{2C_{inv}(V_{gs} - V_t)}{\varepsilon_{si} t_{si}} \tag{2.5}$$

Without $V(y)$, Equation (2.5) is de-coupled to the current continuity equation. Note that Equation (2.5) is a second-order ordinary differential equation that is easier to be solved, given the boundary conditions:

$$\psi(0) = \psi(L) = \left(\frac{kT}{q}\right) \ln\left(\frac{N_{S-D}}{n_i}\right) \tag{2.6}$$

where N_{S-D} is the source and drain doping concentration.

Figure 2.2 shows the potential profile generated by Equation (2.5) at various V_{gs}. A large flat portion of potential ψ over the middle region of the channel is observed, which is controlled by the gate voltage. It turns out that this depth averaged ψ is about $(1-2)kT/q$ lower than the surface potential (i.e., the maximum ψ at the surface), with a value corresponding to an inversion charge density $\frac{Q_i}{t_{si}}$. We can see ψ goes up rapidly near the source and drain ends of the channel, which is caused by the encroachment of the source and drain bands (a.k.a. carrier spillover) into the channel. This is the essence of the short channel effect. This source-drain encroachment effect appears as a gate-voltage dependent reduction of channel resistance, with stronger effect at low gate overdrives.

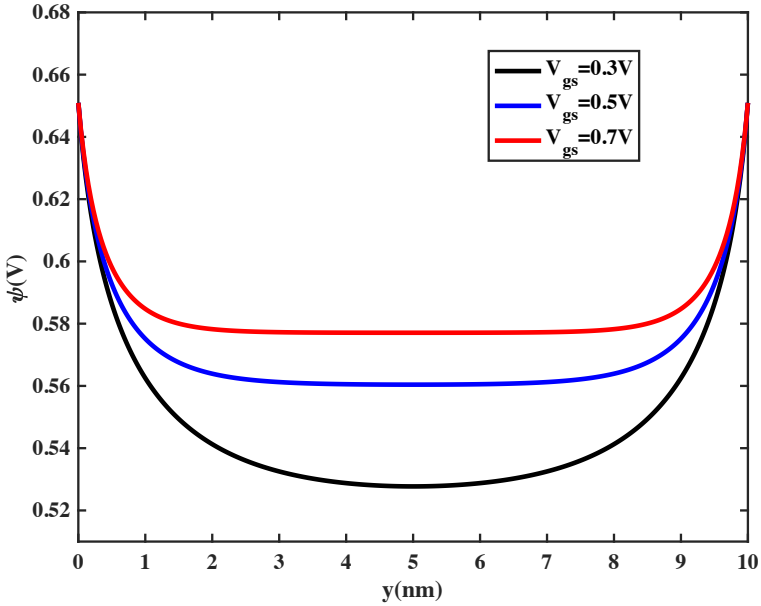

Figure 2.2: Potential ψ in y −direction at a low drain bias voltage, by this short-channel non-GCA model (low drain biases). Here $L = 10nm$.

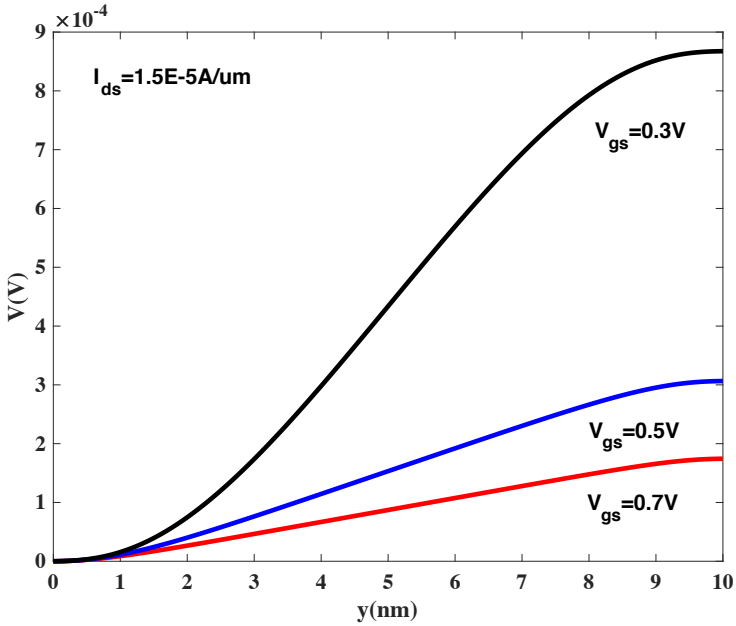

Figure 2.3: Quasi-Fermi Potential $V(y)$ generated by this short-channel non-GCA model (low drain biases) for various V_{gs} given the same $I_{ds} = 1.5E - 5A/um$.

After $\psi(y)$ is solved, the quasi-Fermi potential profile can be also determined:

$$V(y) = \int_0^y \frac{I_{ds}}{Wq\mu_{eff}t_{si}n_i e^{q\psi(y)/kT}}dy \tag{2.7}$$

Figure 2.3 shows the quasi-Fermi potential generated by this short-channel non-GCA model for different V_{gs}. It is obvious that the slope of $V(y)$ is not a constant. Figure 2.4 compares the quasi-Fermi potential $V(y)$ generated by our short-channel non-GCA model and the long channel model (i.e., no source-drain encroachment effect). In long channel case (no source-drain encroachment), only the gate induced inversion charge is considered:

$$V(y) = \frac{I_{ds}y}{2W\mu_{eff}C_{inv}(V_{gs} - V_t)} \tag{2.8}$$

This shows a linear relation between the quasi-Fermi potential V and y. For long channel, the device is a simple resistor with conductance $g_{dc} \propto 1/L$ due to the uniform resistivity[43]. For short channel, however, the source-drain encroachment effect results in a linear region channel conductance, which increases faster than $1/L$ in short channel devices. Unlike the long channel $V(y)$ with a constant dV/dy over the channel, the quasi-Fermi potential of short channel case shows lower slope near the source and drain sides, indicating the effect of the source-drain encroachment. The reduction of integrated resistance of short channel case due to the short channel effect can be quantified by ΔL, defined as the effective shortening of L in Figure 2.4, as far as the linear region channel resistance is concerned. The ΔL is due to the non-uniform resistivity with higher carrier density at the source and drain ends due to the encroachment. This means that the

source-drain encroachment acts like a fixed reduction of L such that the linear-region channel resistance $\frac{V_{ds}}{I_{ds}} \propto (L - \Delta L)$.

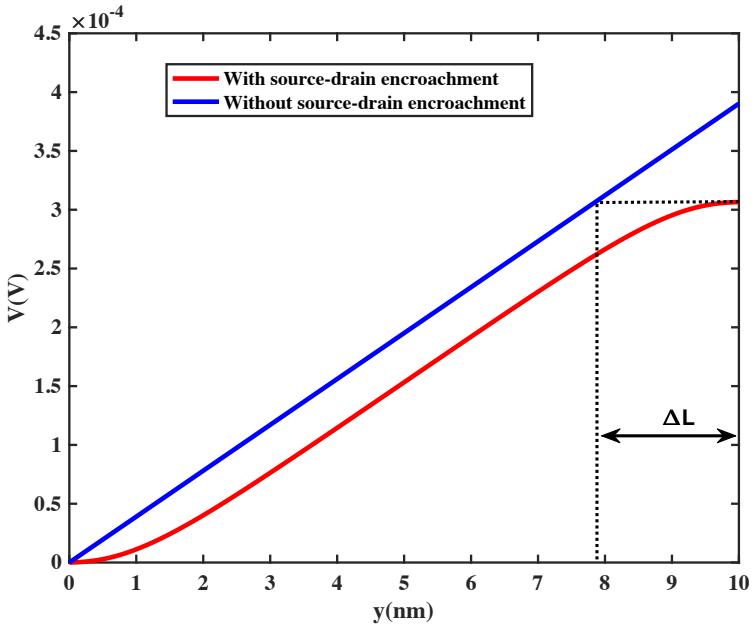

Figure 2.4: Comparison of the quasi-Fermi Potential $V(y)$ between the long- and short- channel cases. For long-channel case, no source-drain encroachment is considered. For short-channel case, with source-drain encroachment, the effective length is shortened by ΔL. $V_{gs} = 0.5V$.

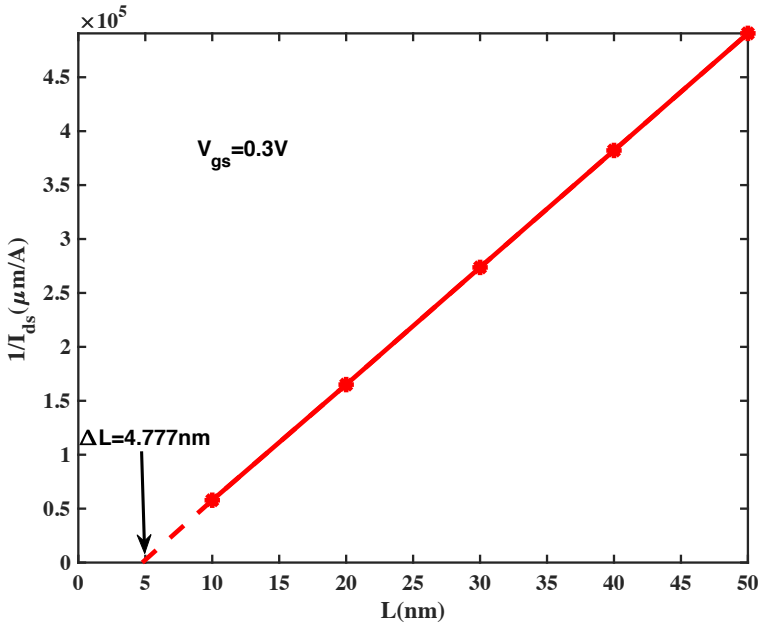

(a)

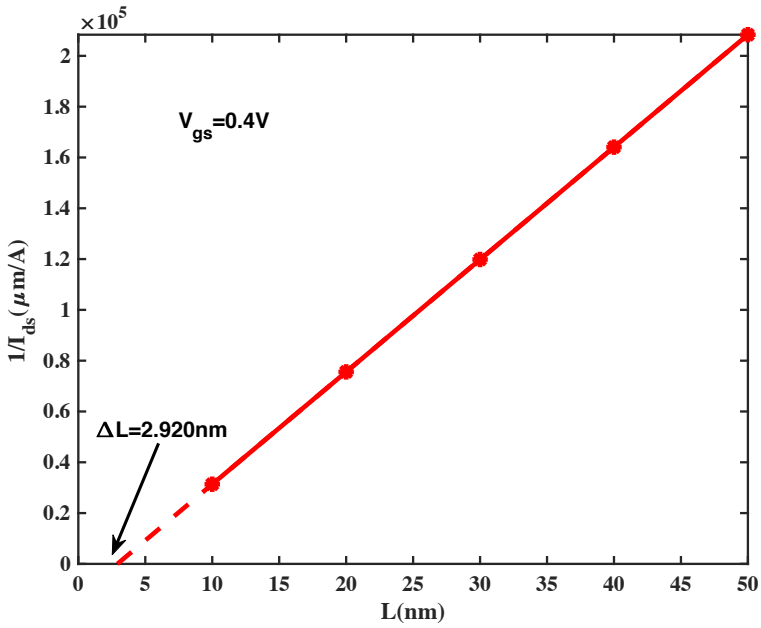

(b)

Figure 2.5: $1/I_{ds}$ as a function of L for various gate voltage V_{gs}. Dash line are generated from the linear extrapolation of the model data, which is plotted as the solid line and symbol. Note the intercept of the line on the $x-$axis ΔL describes the effect of source-drain encroachment. $V_t = 0.247V$.

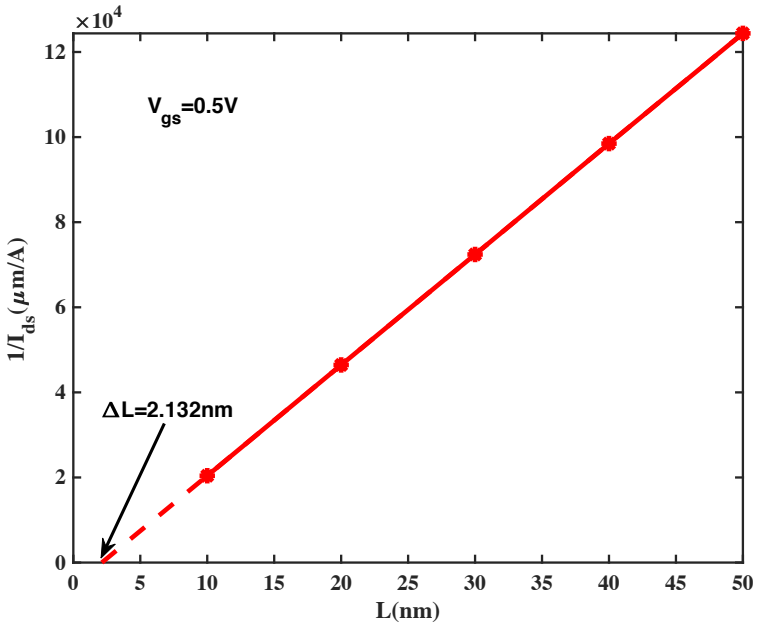

(c)

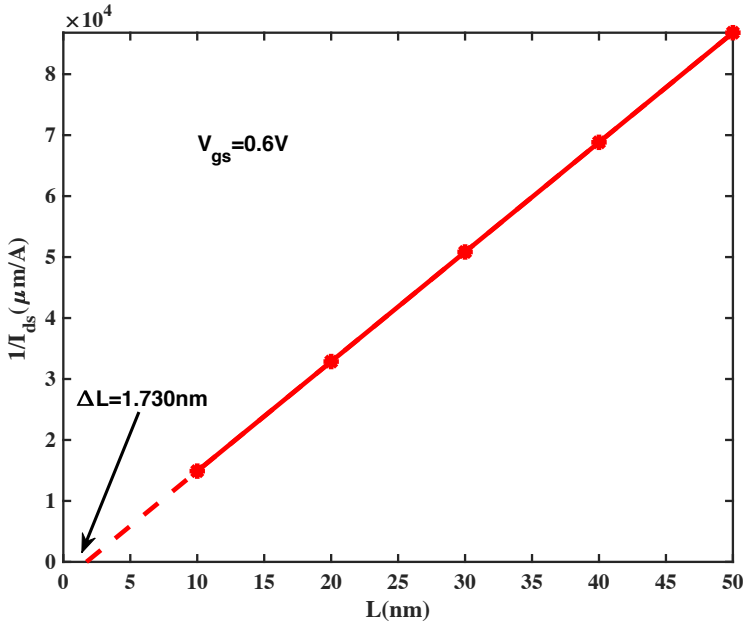

(d)

Figure 2.5: $1/I_{ds}$ as a function of L for various gate voltage V_{gs}, continued.

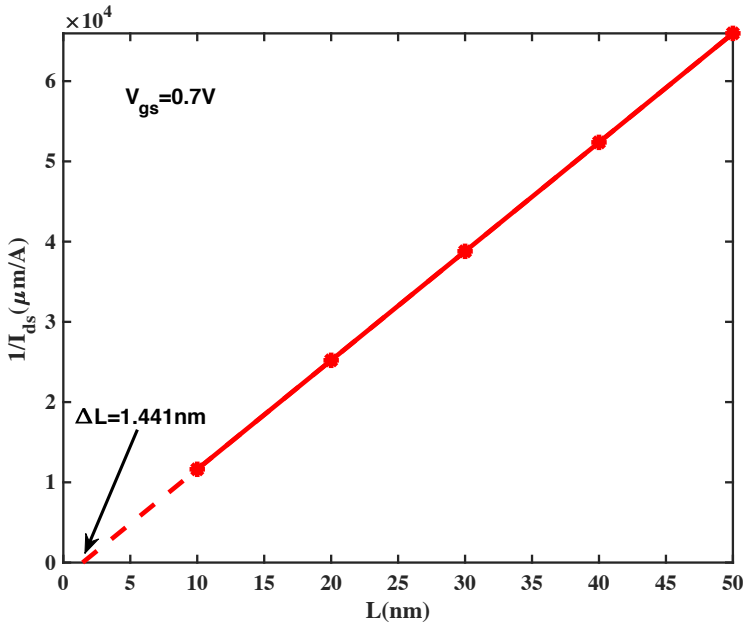

(e)

Figure 2.5: $1/I_{ds}$ as a function of L for various gate voltage V_{gs}, continued.

ΔL can also be extracted by plotting the low drain bias channel resistance or $1/I_{ds}$ versus L , and then linearly extrapolating the intercept with x −axis. Figure 2.5 shows $1/I_{ds}$ versus L for various V_{gs}. The solid line and symbol denote the data generated by the low drain non-GCA short channel model. The dash line is generated by the extrapolation of the model data. We can see for a higher gate voltage drive, a lower ΔL is obtained, showing the gate voltage dependence of the short channel effect.

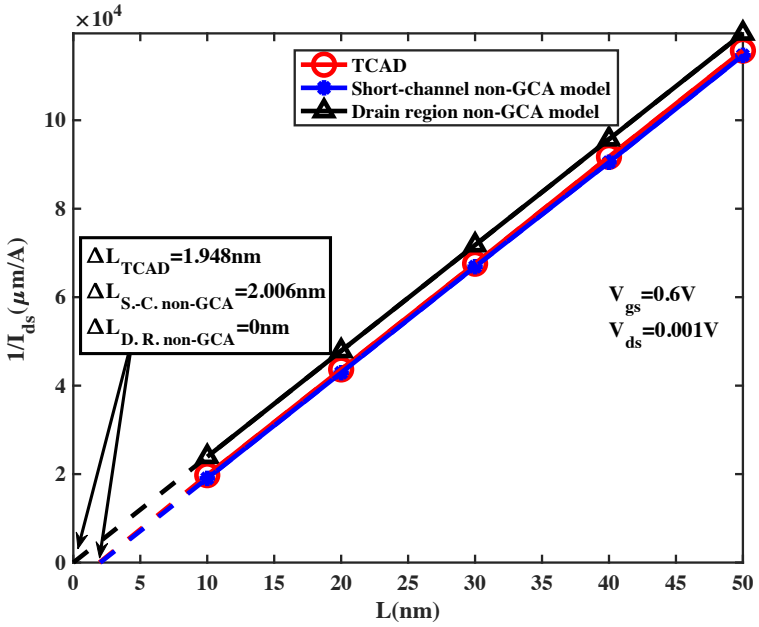

Figure 2.6: $1/I_{ds}$ versus L generated from the drain region non-GCA model[47] and the low drain short channel non-GCA model, compared with TCAD simulation[55]. $V_t = 0.327V$.

Figure 2.6 shows $1/I_{ds}$ as a function of L given $V_{gs} = 0.6V$ generated from the drain region non-GCA model[47] and this low drain short-channel non-GCA model and compared with TCAD simulation. The extrapolated intercept with $x-$ axis of the drain region non-GCA model data $\Delta L_{D.R.nonGCA}$ is 0, indicating that the source-drain encroachment effect is not taken into account. The result generated by the short-channel non-GCA model is consistent with TCAD simulation.

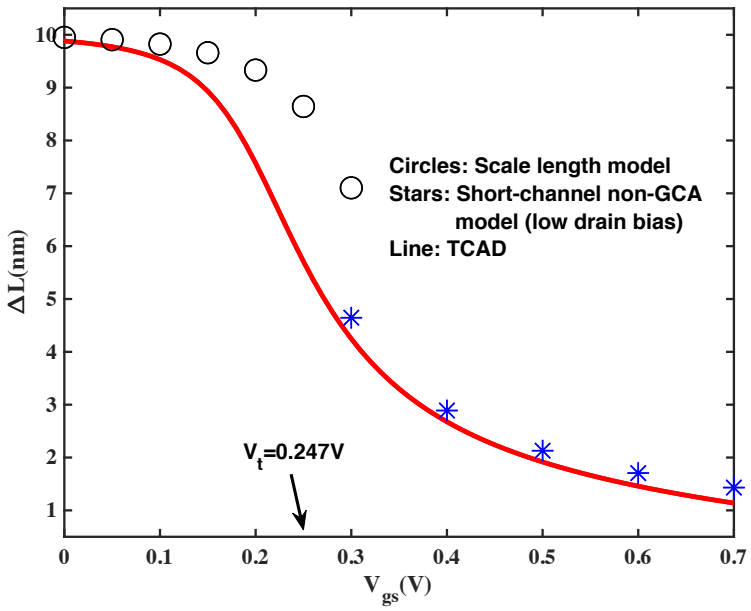

Figure 2.7: Comparison of ΔL versus V_{gs} extracted from Scale length model[32], [38], the low drain short channel non-GCA model and TCAD simulations.

Figure 2.7 shows ΔL versus V_{gs} extracted from scale length model[32][38], the low drain short channel non-GCA model and TCAD simulations. The scale length model achieves a good accuracy in subthreshold, but when V_{gs} goes up further, it no longer works. In the above threshold region, the short-channel non-GCA model is in good agreement with TCAD simulation. It is obvious the short channel effect (i.e., ΔL) is stronger in subthreshold and weaker above threshold.

We can come out with an analytical expression to describe the trend of changing ΔL with respect to V_{gs}. In Figure 2.2, we see the potential profile is symmetry over the channel, indicating $\frac{d\psi}{dy} = 0$ at the midpoint of the channel. For device that is not too short(e.g., $L \gg \sim 10 \times$ of L_D of Equation (2.12) below), the potential at midpoint $\psi\left(y = \frac{L}{2}\right) \equiv \psi_0$ can be estimated as:

$$\frac{q}{\varepsilon_{si}} n_i e^{\frac{q\psi_0}{kT}} = \frac{2C_{inv}(V_{gs} - V_t)}{\varepsilon_{si} t_{si}} \tag{2.9}$$

We can insert Equation (2.9) to Equation (2.5) and get:

$$\frac{d^2\psi}{dy^2} = \frac{qn_i e^{q\psi_0/kT}}{\varepsilon_{si}} \left[e^{\frac{q(\psi - \psi_0)}{kT}} - 1 \right] \tag{2.10}$$

Applying a first-order approximation on the RHS of Equation (2.10) obtains:

$$\frac{d^2\psi}{dy^2} \approx \frac{\psi - \psi_0}{{L_D}^2} \tag{2.11}$$

where

$$L_D = \sqrt{\frac{\varepsilon_{si} kT}{q^2 n_i e^{q\psi_0/kT}}} = \sqrt{\frac{\varepsilon_{si} kT t_{si}}{2qC_{inv}(V_{gs} - V_t)}} \tag{2.12}$$

is the Debye length corresponding to the mid-channel carrier concentration. Figure 2.8 plots the Debye length L_D as a function of gate overdrive. It predicts the changing trend that for a lower gate overdrive, it takes longer for the band to rise up to the source-drain potential, which is consistent with our previous analysis.

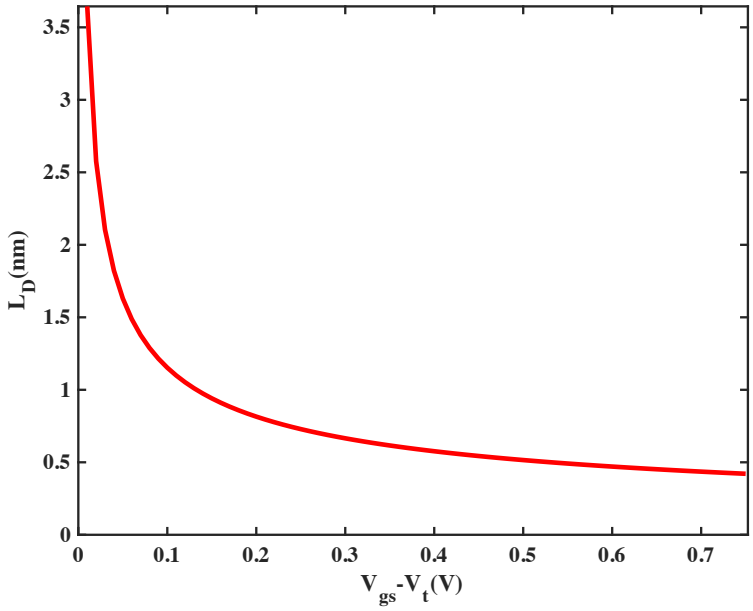

Figure 2.8 L_D as a function of gate overdrive $V_{gs} - V_t$.

Table 2.1: Comparison between the Debye length L_D and ΔL value in Figure 2.7.

$V_{gs}\ (V)$	$L_D(nm)$	$\Delta L(nm)$		
		$L = 10nm$	$L = 15nm$	$L = 20nm$
0.3	1.53	4.66	4.74	4.76
0.5	0.75	2.13	2.14	2.16
0.7	0.54	1.43	1.43	1.45

In Table 2.1, we compare the Debye length L_D with ΔL for various channel lengths L. The L_D values are $0.54nm$ for $V_{gs} = 0.7V$, $0.75nm$ for $V_{gs} = 0.5V$ and $1.53nm$ for $V_{gs} = 0.3V$. The corresponding $\Delta L/2$ values for various L are between $1.3\times$ and $1.6\times$ of L_D.

2.2 Short-Channel Non-GCA Model for High Drain Bias Case

For high drain bias case, to solve the potential and quasi-Fermi potential, we have to couple Equation (2.4) with the current continuity equation[2][43]:

$$I_{ds} = \mu_{eff} W q t_{si} n_i e^{\frac{q(\psi - V)}{kT}} \frac{dV}{dy} \tag{2.13}$$

We have four boundary conditions:

$$V(0) = 0 \tag{2.14a}$$

$$V(L) = V_{ds} \tag{2.14b}$$

$$\psi(0) = \left(\frac{kT}{q}\right) \ln\left(\frac{N_{s-D}}{n_i}\right) \tag{2.14c}$$

$$\psi(L) = \left(\frac{kT}{q}\right) \ln\left(\frac{N_{s-D}}{n_i}\right) + V_{ds} \tag{2.14d}$$

For given V_{ds}, $\psi(y)$ and $V(y)$ are generated from Equations (2.4) and (2.13) with an initial guess of I_{ds}. Then compare the value of $V(L)$ and V_{ds}. If they are not the same, we adjust I_{ds} and repeat the process until $V_{ds} = V(L)$ is satisfied.

This iteration process is time consuming. To avoid the cumbersome process, we can apply a variable transformation technology by introducing a new valuable $u(y) \equiv \psi(y) - V(y)$. The Equation (2.13) can be transformed as:

$$\frac{dV}{dy} = \frac{I_{ds}}{\mu_{eff} W q t_{si} n_i e^{\frac{qu}{kT}}} \tag{2.15}$$

Meanwhile, we can change Equation (2.4) as:

$$\frac{d^2u}{dy^2} = \frac{q}{kT} \frac{I_{ds}}{\mu_{eff} W q t_{si} n_i e^{\frac{qu}{kT}}} \frac{du}{dy} + \frac{q}{\varepsilon_{si}} n_i e^{\frac{qu}{kT}} - \frac{2C_{inv}\left(V_{gs} - V_t - V\right)}{\varepsilon_{si} t_{si}} \tag{2.16}$$

In this way, to solve the equations, three boundary conditions are needed:

$$u(0) = u_{max} \equiv (kT/q)\ln\left(N_{S-D}/n_i\right) \tag{2.17a}$$

$$u(L) = u_{max} \equiv (kT/q)\ln\left(N_{S-D}/n_i\right) \tag{2.17b}$$

$$V(0) = 0 \tag{2.17c}$$

Here V_{ds} is not included in those boundary conditions. A finite difference method implemented in a standard mathematics tool can be employed[56]–[61]. For a given I_{ds}, we can solve the coupled Equations (2.15) and (2.16) to get $\psi(y)$ and $V(y)$. V_{ds} is given by $V(L)$ so that $I_{ds} - V_{ds}$ relation can be constructed. During this process, no iteration is needed.

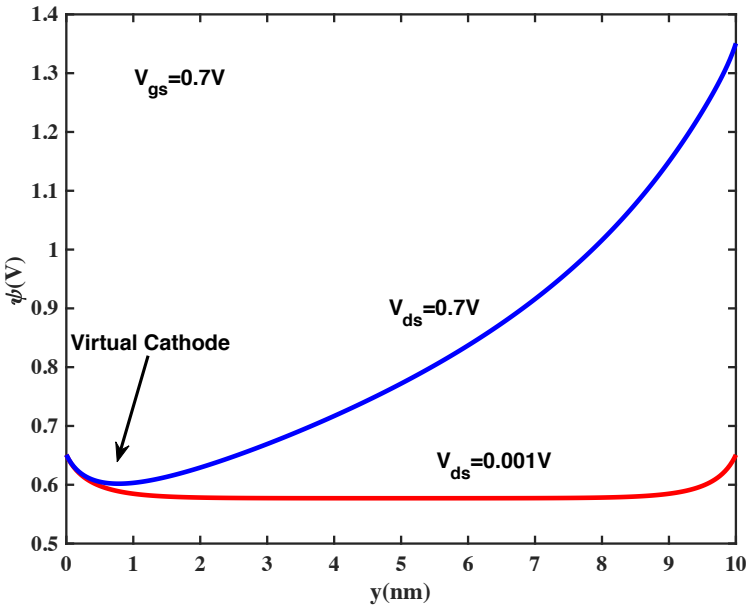

Figure 2.9: The potential profile generated by the short-channel non-GCA model for low drain bias (e.g., $V_{ds} = 0.001V$) and high drain bias (e.g., $V_{ds} = 0.7V$)(constant mobility).

Figure 2.9 compares the potential profiles generated from this short-channel non-GCA model for low and high drain bias cases. The intersection of the source band encroachment with the gate-controlled channel potential results in a point of minimum, or "virtual cathode"[62], a small distance from the source. The current is diffusion in nature before this point and drift in nature after this point. The Drain Induced Barrier Lowering (DIBL)[43] at the maximum barrier (virtual cathode) can be obviously observed.

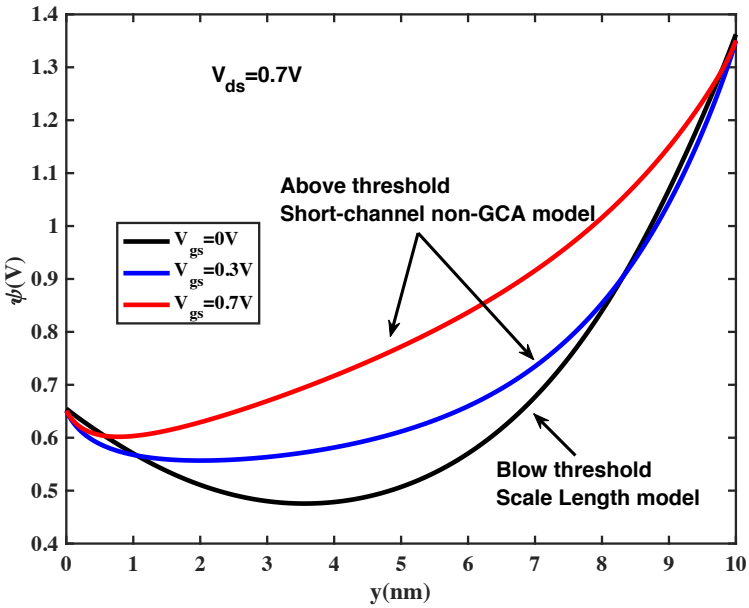

Figure 2.10: Comparison of potential profile $\psi(y)$ for various V_{gs}. The low gate bias curve (i.e., $V_{gs} = 0V$) is generated by the scale length model while the high gate bias curves (i.e., $V_{gs} = 0.3V\ and\ 0.7V$) are generated by this short-channel non-GCA model.

Figure 2.10 compares the potential profile $\psi(y)$ for various V_{gs}. The curve for V_{gs} below subthreshold (i.e., $V_{gs} = 0V$) is generated by the scale length model[32], [38] while the curves (i.e., $V_{gs} = 0.3V\ and\ 0.7V$) are generated by the short-channel non-GCA model. It is clear the position of the minimum potential is V_{gs} −dependent.

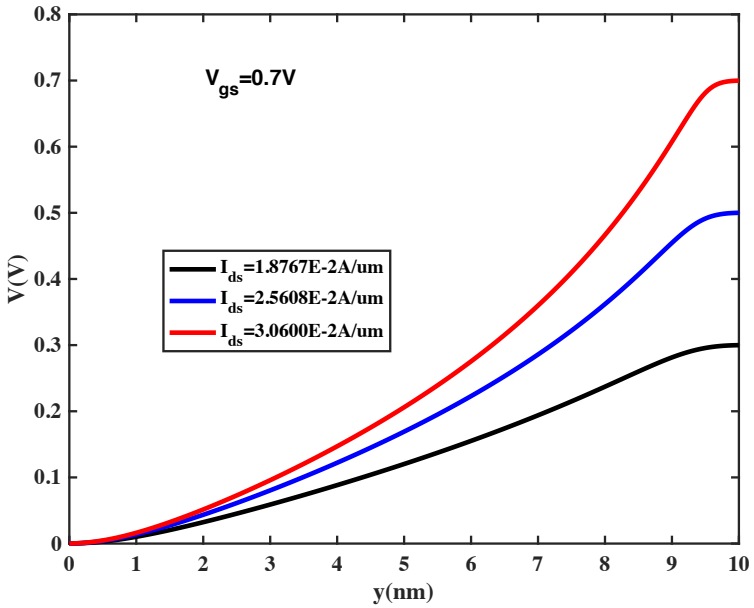

Figure 2.11: The quasi-Fermi potential profile $V(y)$ along y, generated by the high drain short-channel non-GCA model.

Figure 2.11 shows the quasi-Fermi potential V as a function of y for various I_{ds}, generated by the high drain short-channel non-GCA model. For each I_{ds}, we can select the value of V at $y = L = 10nm$ as $V_{ds.}$ For example, $V_{ds} = 0.3, 0.5\ and\ 0.7V$ are gotten for $I_{ds} = 1.8767E-2, 2.5608E-2\ and\ 3.0600E-2A/um$, respectively.

2.3 Velocity Saturation (n=1)

For high drain biases, with $n = 1$ the velocity saturation model, the current continuity equation is rewritten as:

$$I_{ds} = Wt_{si}qn_i e^{q(\psi - V)/kT} \frac{\mu_{eff} dV/dy}{1 + \left(\frac{\mu_{eff}}{v_{sat}}\right) dV/dy} \tag{2.18}$$

where v_{sat} is the saturation velocity[50], [63]–[65]. We can solve dV/dy from Equation (2.18):

$$\frac{dV}{dy} = \frac{I_{ds}/\mu_{eff}}{Wt_{si}qn_i e^{q(\psi - V)/kT} - I_{ds}/v_{sat}} \tag{2.19}$$

To solve $\psi(y)$ and $V(y)$, Equation (2.19) is coupled with (2.4) with four boundary condition given by (2.14a)-(2.14d). Given a V_{gs}, I_{ds} is an unknown parameter in Equation (2.19), which is needed to be solved. Similarly, we can change $\psi(y)$ to a new variable $u(y) \equiv \psi(y) - V(y)$ to avoid tedious iterative procedure. In this way, Equations (2.4) and (2.19) becomes:

$$\frac{d^2u}{dy^2} = \frac{\left(\frac{q}{kT}\right)\left(\frac{I_{ds}}{\mu_{eff}}\right)}{\left(Wt_{si}qn_i e^{\frac{qu}{kT}} - \frac{I_{ds}}{v_{sat}}\right)^2} Wt_{si}qn_i e^{\frac{qu}{kT}} \frac{du}{dy} + \frac{q}{\varepsilon_{si}} n_i e^{\frac{qu}{kT}} - \frac{2C_{inv}\left(V_{gs} - V_t - V\right)}{\varepsilon_{si} t_{si}} \tag{2.20}$$

$$\frac{dV}{dy} = \frac{I_{ds}/\mu_{eff}}{Wt_{si}qn_i e^{qu/kT} - I_{ds}/v_{sat}} \tag{2.21}$$

For a given I_{ds}, to solve $u(y)$ and $V(y)$, three boundary conditions needed are given by Equations (2.17a)-(2.17c). Figure 2.12 shows the potential $\psi(y)$ solved by this model for various V_{gs}. As V_{gs} increases, the minimum potential, the virtual cathode, shifts toward the source. For each V_{gs}, due to the Drain Induced Barrier Lowering (DIBL) effect, the minimum potential at mid-

channel in Figure 2.2 for low drain biases is always lower than the minimum potential at the virtual cathode.

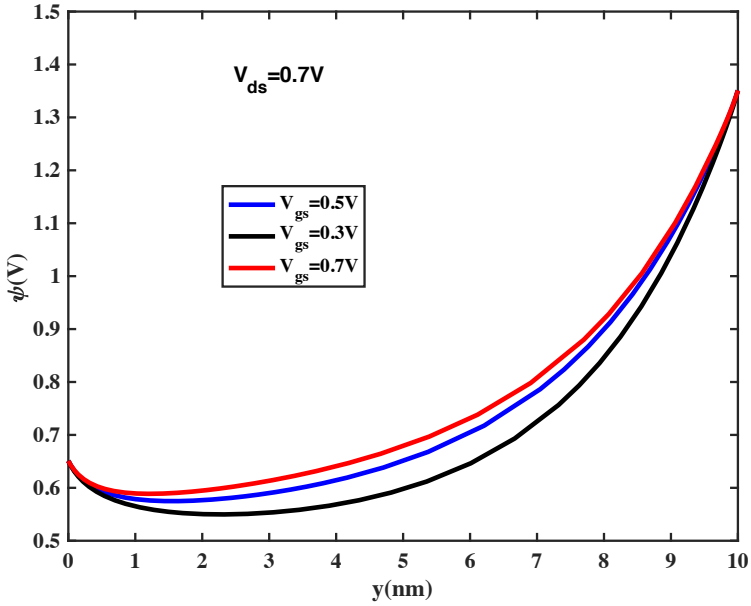

Figure 2.12: The $\psi(y)$ curves generated by the high drain short-channel non-GCA model for various V_{gs}.

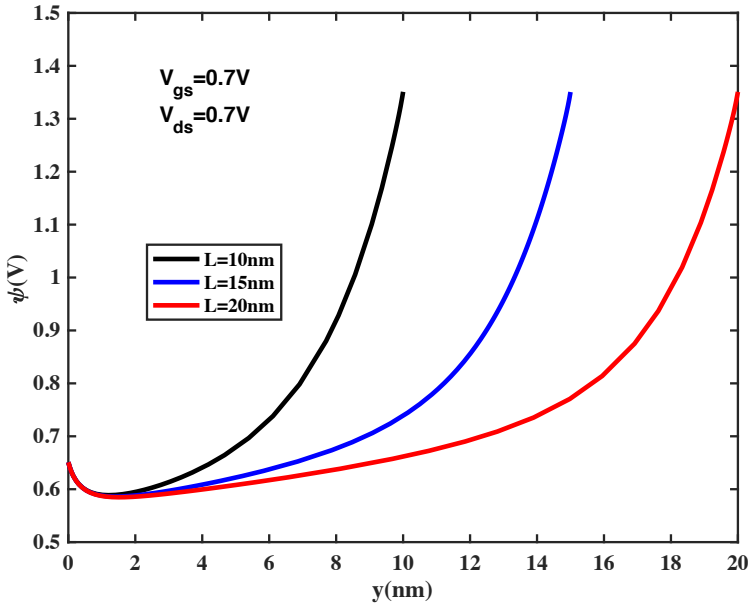

Figure 2.13: The potential profile $\psi(y)$ along y generated by the high drain short-channel non-GCA model for several values of L.

Figure 2.13 shows the model solved potential profile from the source to drain for $L = 10, 15, 20nm$. A virtual cathode point can be observed in each curve with channel length of L. The virtual cathode point is almost the same distant from the source given the same bias condition, regardless of the different lengths.

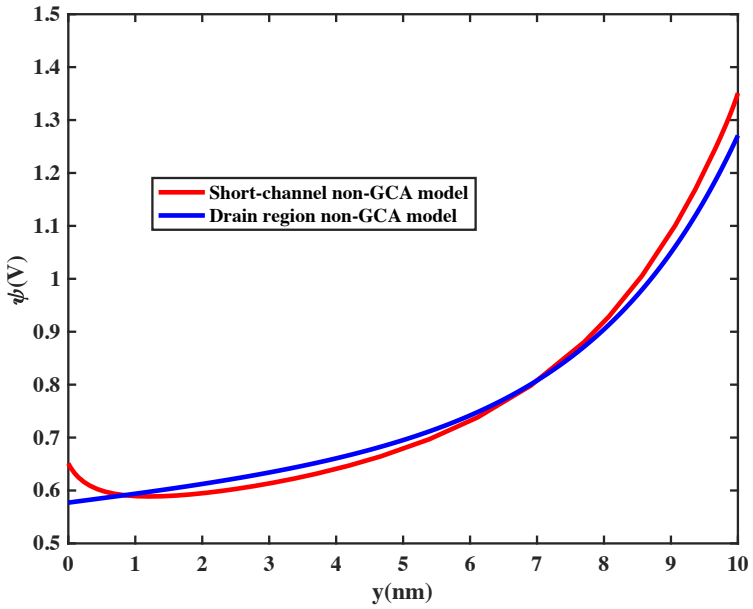

Figure 2.14: Comparison of the potential profiles $\psi(y)$ along y generated by this short-channel non-GCA model and drain region non-GCA model[50].

Figure 2.14 shows the comparison of the potential profile $\psi(y)$ generated by this short-channel non-GCA model and drain region non-GCA model[47], [50]. It is clear that there isn't a virtual cathode on the drain region non-GCA curve. Figure 2.15 compares the quasi-Fermi potential profiles generated by those two models. It is shown that this short-channel non-GCA model has a $dV/dy|_{y=0} \approx 0$ while the drain region non-GCA model has high value of $dV/dy|_{y=0}$ because the source-drain encroachment effect is not incorporated.

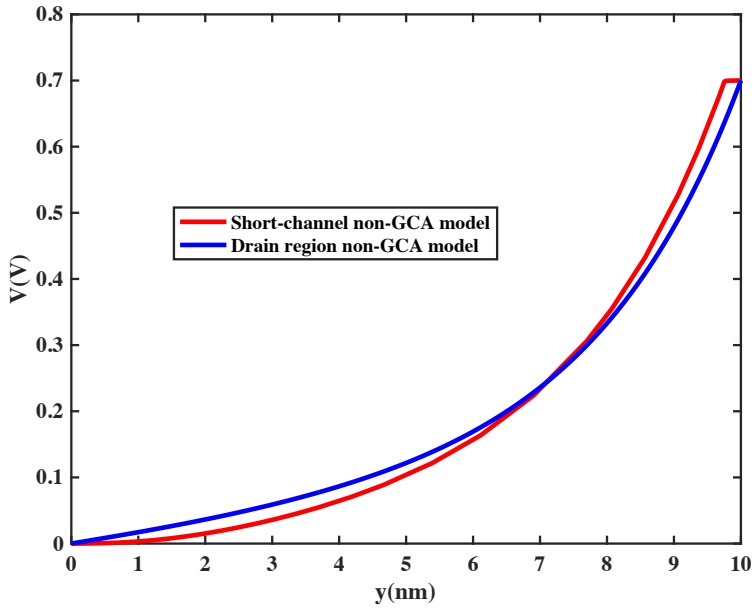

Figure 2.15: Comparison of the quasi-Fermi potential profiles $V(y)$ along y generated by different models.

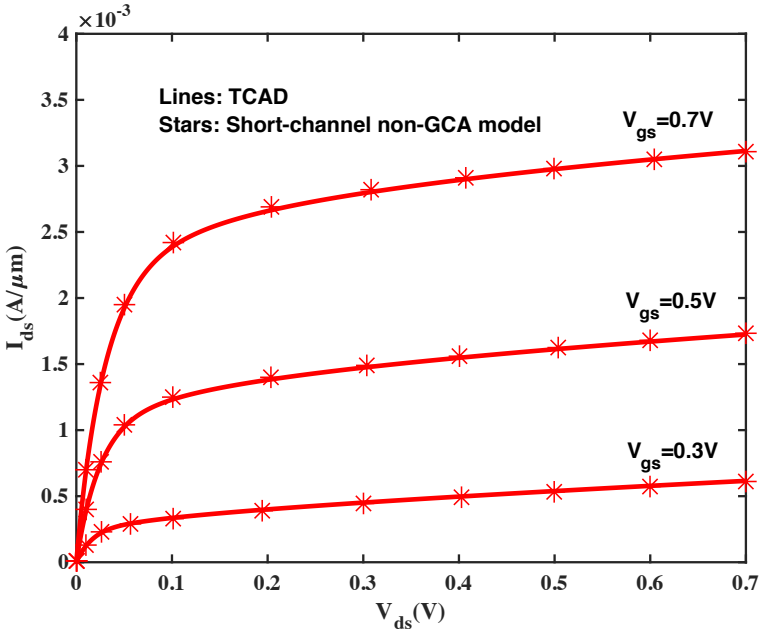

Figure 2.16: $I_{ds} - V_{ds}$ characteristics generated by solving the coupled Equations (2.20) and (2.21) with fixed boundary conditions (2.17) are compared to TCAD. The source-drain doping level is $10^{21} cm^{-3}$.

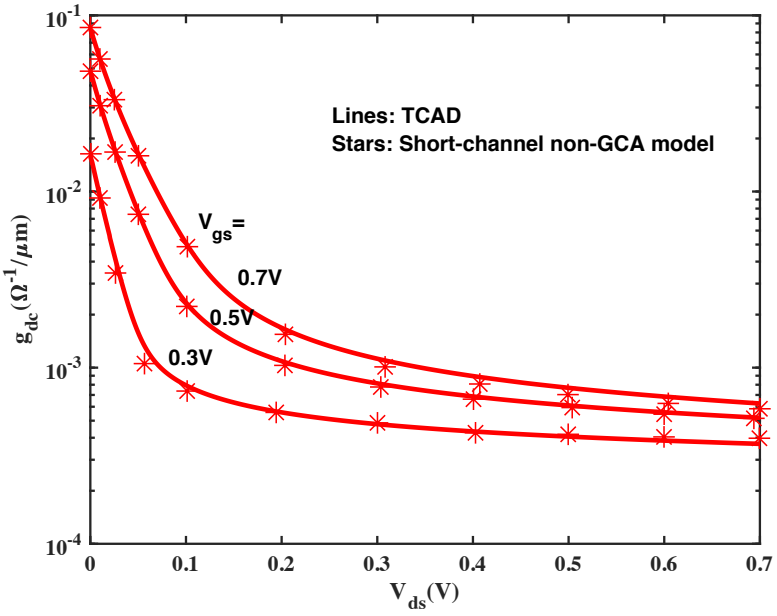

Figure 2.17: $g_{ds} \equiv dI_{ds}/dV_{ds}$ generated by solving the coupled Equations (2.20) and (2.21) with fixed boundary conditions (2.17) are compared to TCAD. The source-drain doping level is $10^{21} cm^{-3}$.

Figure 2.16 shows the $I_{ds} - V_{ds}$ characteristics generated by this short-channel non-GCA model are compared to the TCAD simulation with source-drain doping concentration of $10^{21} cm^{-3}$. Figure 2.17 shows the output conductance, $g_{dc} \equiv dI_{ds}/dV_{ds}$, between the short-channel non-GCA model and TCAD. High accuracy is achieved over the entire range of V_{ds}.

2.4 Matching Model with Source-Drain Depletion

In Section 2.3, we employed fixed boundary conditions, given by Equations (2.17a)-(2.17c), to solve the coupled equations sets. It turns out these boundary conditions worked well only for device with very high source-drain doping concentration (e.g., $N_{S-D} = 10^{21} cm^{-3}$) because the band bending and depletion widths in the source and drain regions are not taken into

account. It may overestimate I_{ds} for more moderate source-drain doping levels (e.g., $N_{S-D} = 10^{20} cm^{-3}$) since there are significant drops of the quasi-Fermi potential in the source and drain regions[66]–[72]. To model I_{ds} accurately, we have to reconstruct better boundary conditions so that they may match the potential and quasi-Fermi potential of the source and drain regions at $y = 0$ and L, respectively.

In the source and drain regions, Poisson's equation with the quasi-Fermi potential $V(y)$ is given as:

$$\frac{d^2\psi}{dy^2} = \frac{q}{\varepsilon_{si}}\left[n_i e^{\frac{q(\psi - V)}{kT}} - N_{S-D}\right] \tag{2.22}$$

The current continuity equation in the source and drain regions are the same as that of the channel, given by Equation (2.19). By changing $\psi(y)$ to $u(y) \equiv \psi(y) - V(y)$, we can transform Equations (2.19) to (2.21), and (2.22) to:

$$\frac{d^2u}{dy^2} = \frac{\left(\frac{q}{kT}\right)\left(\frac{I_{ds}}{\mu_{eff}}\right)}{[Wt_{si}qn_i e^{\frac{qu}{kT}} - I_{ds}/v_{sat}]^2} Wt_{si}qn_i e^{qu/kT}\frac{du}{dy} + \frac{q}{\varepsilon_{si}}\left[n_i e^{\frac{qu}{kT}} - N_{S-D}\right] \tag{2.23}$$

The contact-to-contact boundary conditions for the source and drain regions are:

$$u(-l_c) = u_{max} \equiv \left(\frac{kT}{q}\right)\ln\left(\frac{N_{S-D}}{n_i}\right) \tag{2.24a}$$

$$u(L + l_c) = u_{max} \equiv \left(\frac{kT}{q}\right)\ln\left(\frac{N_{S-D}}{n_i}\right) \tag{2.24b}$$

$$V(-l_c) = 0 \tag{2.24c}$$

Here, l_c is the source and drain region length. To avoid the cumbersome boundary conditions at $y = 0$ and L for solving the channel region, we introduce a new variable $u = u_{max} - \Delta u$ in the source-drain regions. Equation (2.23) turns to:

$$\frac{d^2\Delta u}{dy^2} - \frac{\left(\frac{q}{kT}\right)\left(\frac{I_{ds}}{\mu_{eff}}\right)}{\left[Wt_{si}qn_i e^{\frac{qu}{kT}} - \frac{I_{ds}}{v_{sat}}\right]^2} Wt_{si}qn_i e^{\frac{qu}{kT}} \frac{d\Delta u}{dy} - \frac{q^2 N_{S-D}}{\varepsilon_{si}kT}\Delta u = 0 \tag{2.25}$$

Here only the 1st-order of Δu is considered. On the source side, the second term on LHS can be neglected since the carrier velocity $\ll v_{sat}$. There is an analytic solution for Equation (2.25):

$$\Delta u = [u_{max} - u(0)]e^{\frac{y}{L_{D0}}} \tag{2.26}$$

where

$$L_{D0} = \sqrt{\frac{\varepsilon_{si}kT}{q^2 N_{S-D}}} \tag{2.27}$$

is the Debye length in the source side. Since $L_{D0} \ll l_c$, a boundray condition at $y = 0$ can be obtained:

$$\frac{du}{dy}|_{y=0} = -\frac{u_{max} - u(0)}{L_{D0}} \tag{2.28}$$

On the drain region, however, the second term in Equation (2.25) is not negligible because the carrier velocities may be comparable with v_{sat}. By approximating the $u(y)$ factor in that term constant as $u(L)$, we can also get a solution on the drain region:

$$u_{max} - u = [u_{max} - u(L)]e^{-K(y-L)} \tag{2.29}$$

where

$$K = \sqrt{\left\{\frac{\left(\frac{q}{kT}\right)\left(\frac{I_{ds}}{\mu_{eff}}\right)}{2\left[Wt_{si}qn_i e^{\frac{qu(L)}{kT}} - \frac{I_{ds}}{v_{sat}}\right]} Wt_{si}qn_i e^{\frac{qu(L)}{kT}}\right\}^2 + \frac{q^2 N_{S-D}}{\varepsilon_{si}kT}} - \frac{\left(\frac{q}{kT}\right)\left(\frac{I_{ds}}{\mu_{eff}}\right)}{2\left[Wt_{si}qn_i e^{\frac{qu(L)}{kT}} - \frac{I_{ds}}{v_{sat}}\right]} Wt_{si}qn_i e^{\frac{qu(L)}{kT}} \tag{2.30}$$

Here K is a function of $u(L)$. In one limit, we have:

$$K \approx \frac{1}{L_D} \tag{2.31}$$

In the other limit, we have:

$$K \approx \frac{\left[Wt_{si}qn_i e^{\frac{qu(L)}{kT}} - \frac{I_{ds}}{v_{sat}}\right]^2}{\frac{I_{ds}}{\mu_{eff}} Wt_{si} n_i \varepsilon_{si}} N_{S-D} e^{-\frac{qu(L)}{kT}} \tag{2.32}$$

Then we can get a boundary condition at $y = L$:

$$\frac{du}{dy}|_{y=L} = K[u_{max} - u(L)] \tag{2.33}$$

We still need another additional boundary condition to solve the channel coupled equations. We can take the average of the values of $\frac{dV}{dy}$ at $y = 0$ and $y = -l_c$ to estimate $V(0)$:

$$V(0) = \frac{l_c}{2}\left[\frac{dV}{dy}|_{y=0} + \frac{dV}{dy}|_{y=-l_c}\right] = \frac{l_c}{2}\left[\frac{\frac{I_{ds}}{\mu_{eff}}}{Wt_{si}qn_i e^{\frac{qu(0)}{kT}} - \frac{I_{ds}}{v_{sat}}} + \frac{\frac{I_{ds}}{\mu_{eff}}}{Wt_{si}qN_{S-D} - \frac{I_{ds}}{v_{sat}}}\right] \tag{2.34}$$

Now we can replace the fixed boundary conditions given by Equations (2.17a)-(2.17c) with the new ones by Equations (2.28), (2.33) and (2.34) for solving the coupled Equations (2.20) and (2.21) in channel region. To take the drop of quasi-Fermi potential in the drain region into account, we have to solve the equation (2.23) with two boundary conditions: one is given by Equation (2.24b) and the other one is $u(L)$ solved from the channel region. Then we can integrate Equation (2.21) from $y = L$ to $L + l_c$ to get the quasi-Fermi potential profile in the drain region. Note that V_{ds} is not $V(L)$ any more, like we did in the Section 2.3. Instead, we should add the drop of quasi-

Fermi potential in the drain region to $V(L)$ we solved from the channel region so $V_{ds} = V(L + l_c)$. This process generates a point on the $I_{ds} - V_{ds}$ characteristics.

Figure 2.18 shows the potential $\psi(y)$ generated by matching the potential in the source and the drain regions with depletion effects in the channel region. Unlike the slight drops of potential in the source, substantial drops is observed in the drain due to the high field and carrier velocity which approaches v_{sat}.

Figure 2.19 plots the quasi-Fermi potential $V(y)$ from the source contact to the drain contact, generated by our short-channel non-GCA model with matching boundary conditions, for various V_{ds}. When V_{ds} moves deeper into the saturation region, a more significant fraction of V_{ds} is dropped in the drain region.

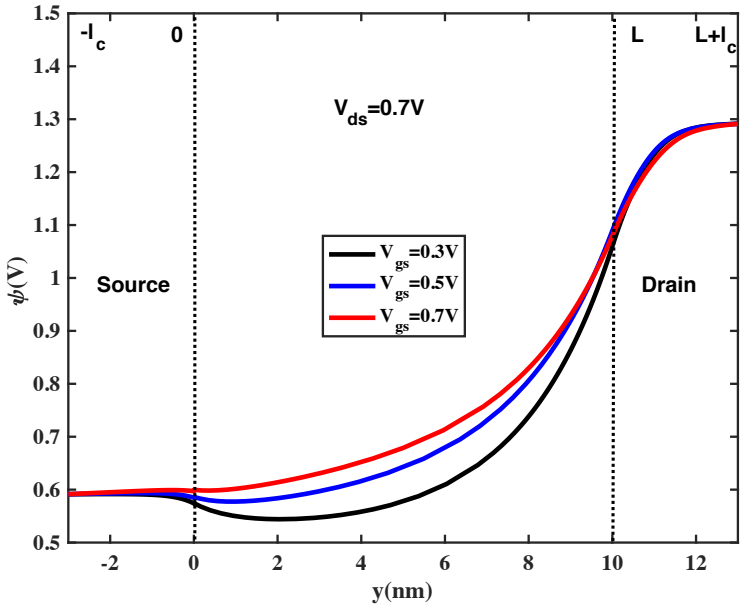

Figure 2.18: Potential profile $\psi(y)$ from the source contact to the drain contact generated by this matching model (i.e., with boundary conditions Equations (2.28), (2.31) and (2.32)). The source-drain doping concentration is $N_{S-D} = 10^{20} cm^{-3}$. The source and drain lengths are assumed to be $l_c = 3nm$.

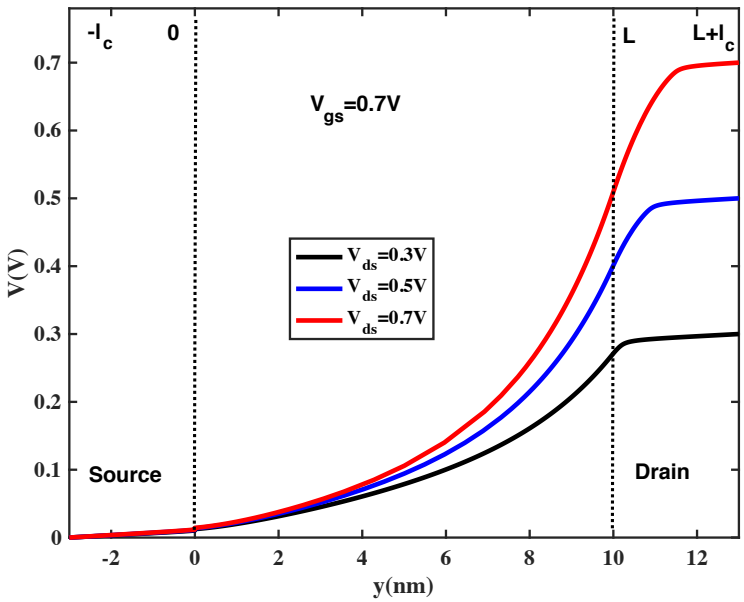

Figure 2.19: Quasi-Fermi Potential profile $V(y)$ from the source contact to the drain contact generated by the matching model with source-drain depletion.

Figure 2.20 compares the potential $\psi(y)$ from our short-channel non-GCA model with matching boundary conditions and fixed boundary conditions. The source-drain doping levels are $N_{S-D} = 10^{21} cm^{-3}$. Only very slight drops are observed in the source and drain regions from the matching model. Figure 2.21 compares the quasi-Fermi potential profiles $V(y)$ from those two models with the same high level of the source-drain doping. The potentials $\psi(y)$ and quasi-Fermi potentials $V(y)$ generated by the model with fixed boundary conditions are in close agreement with that of matching boundary conditions. This means the fixed boundary conditions are good approximations for a high source-drain doping concentration.

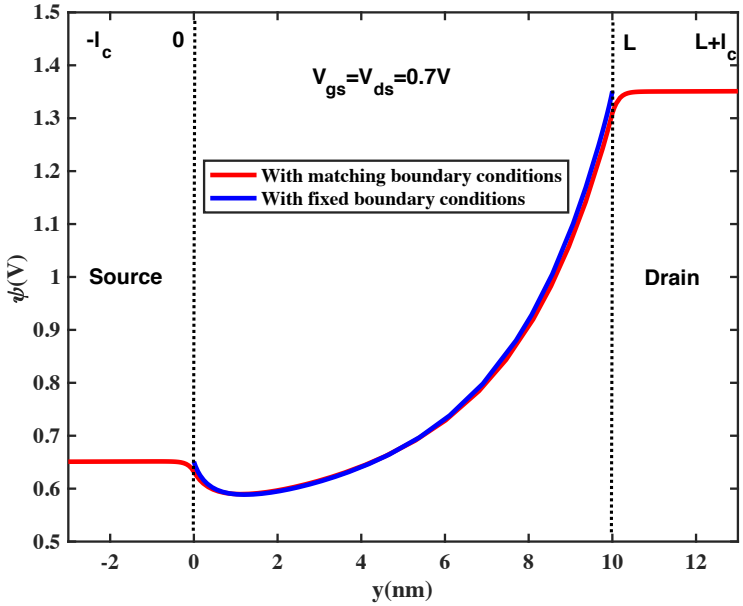

Figure 2.20: Comparison of Potential profile generated from the model with fixed boundary conditions and with matching boundary conditions. The source-drain doping levels are $N_{S-D} = 10^{21} cm^{-3}$.

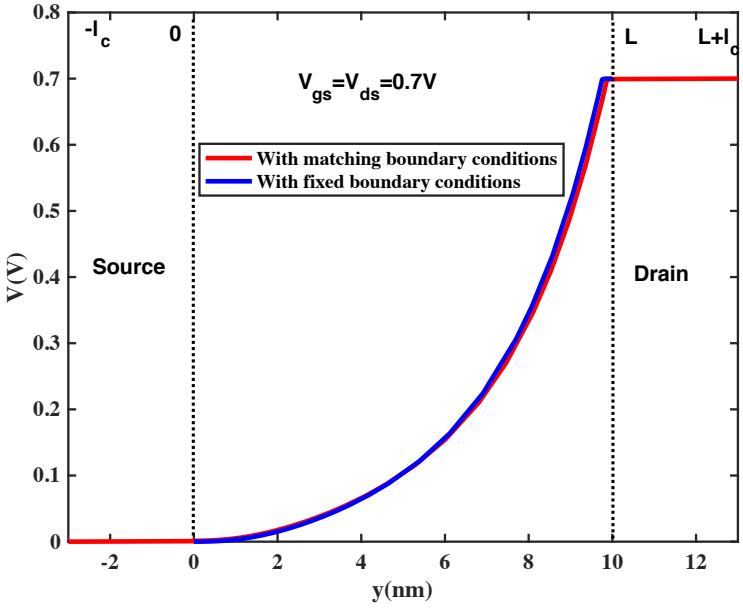

Figure 2.21: Comparison of quasi-Fermi Potential profile generated from the model with fixed boundary conditions and with matching boundary conditions. The source-drain doping levels are $N_{S-D} = 10^{21} cm^{-3}$.

Figure 2.22 compares the potential $\psi(y)$ from our short-channel non-GCA model with matching boundary conditions and fixed boundary conditions, with the source-drain doping concentration of $N_{S-D} = 10^{20} cm^{-3}$. Obviously, the fixed boundary conditions are unable to account for the large fraction of drops of potential in the drain side and overestimate the potential near the drain side. Figure 2.23 shows the quasi-Fermi potential $V(y)$ generated by the model with the two different boundary conditions. A large discrepancy on the value of $V(L)$ (e.g., $\sim 0.2V$) is observed from those two types of boundary conditions. This shows the fixed boundary conditions don't work for moderate source-drain doping levels (e.g., $N_{S-D} = 10^{20} cm^{-3}$).

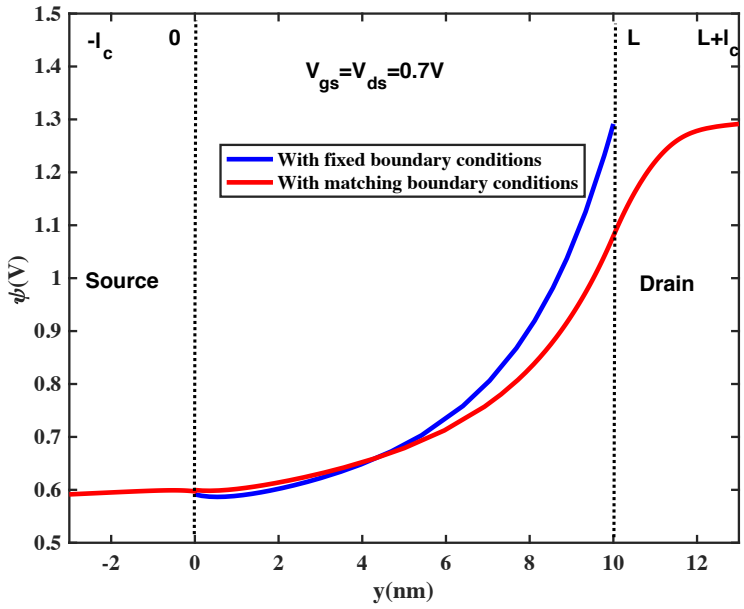

Figure 2.22: Comparison of Potential profile generated from the model with fixed boundary conditions and with matching boundary conditions. The source-drain doping levels are $N_{S-D} = 10^{20} cm^{-3}$.

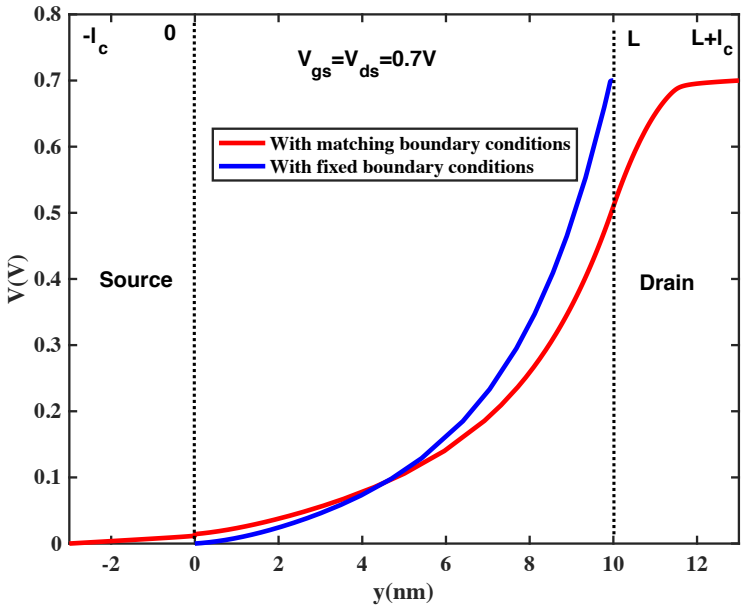

Figure 2.23: Comparison of quasi-Fermi Potential profile generated from the model with fixed boundary conditions and with matching boundary conditions. The source-drain doping levels are $N_{S-D} = 10^{20} cm^{-3}$.

Figures 2.24 and 2.25 compare $I_{ds} - V_{ds}$ generated from our short-channel non-GCA model with different boundary conditions, with the source-drain doping concentration of $N_{S-D} = 10^{20}$ and $10^{21} cm^{-3}$, respectively. For a high level of the source-drain doping concentrations, $I_{ds} - V_{ds}$ characteristics from those two types of boundary conditions are in close agreement to each other due to the consistent potential $\psi(y)$ and the quasi-Fermi potential $V(y)$, as discussed above. However, for the moderate level of the source-drain doping concentrations, the current of the fixed boundary conditions is significantly off (e.g., up to 9%) from that of the matching boundary conditions.

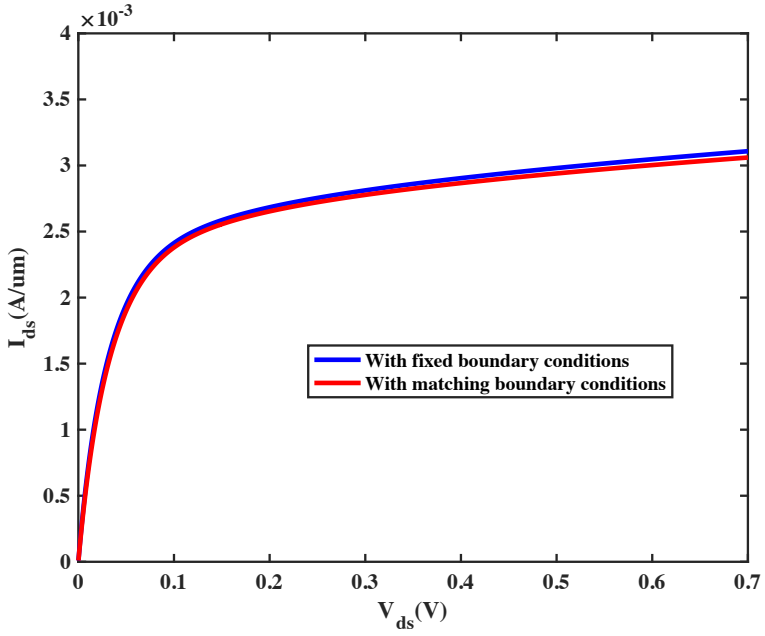

Figure 2.24: Comparison of $I_{ds} - V_{ds}$ generated from the model with fixed boundary conditions and with matching boundary conditions. The source-drain doping levels are $N_{S-D} = 10^{21} cm^{-3}$ and $V_{gs} = 0.7V$.

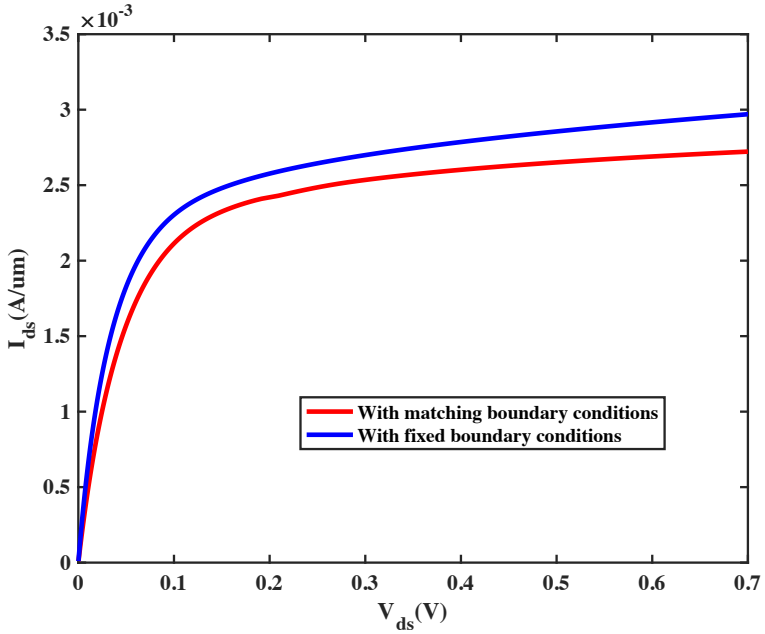

Figure 2.25: Comparison of $I_{ds} - V_{ds}$ generated from the model with fixed boundary conditions and with matching boundary conditions. The source-drain doping levels are $N_{S-D} = 10^{20} cm^{-3} and$ $V_{gs} = 0.7V$.

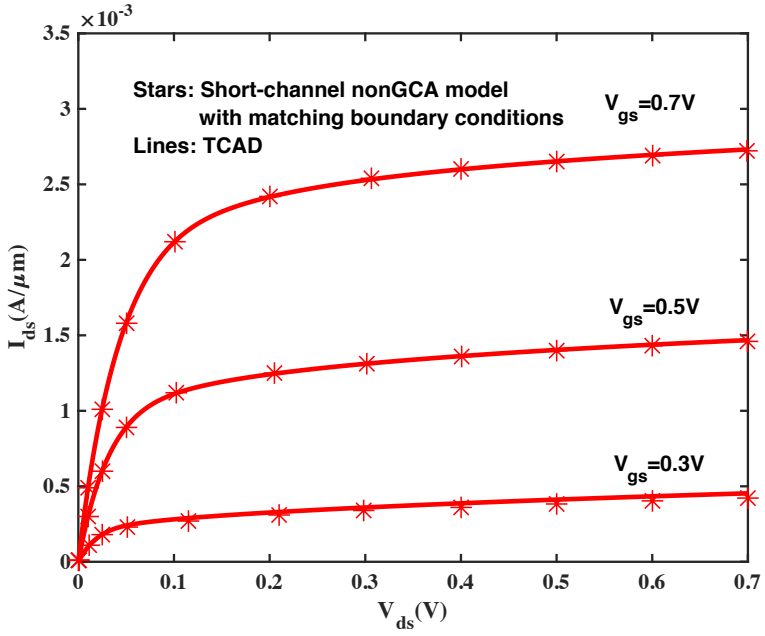

Figure 2.26: $I_{ds} - V_{ds}$ characteristics generated by this matching model with the source-drain depletion, compared with TCAD.

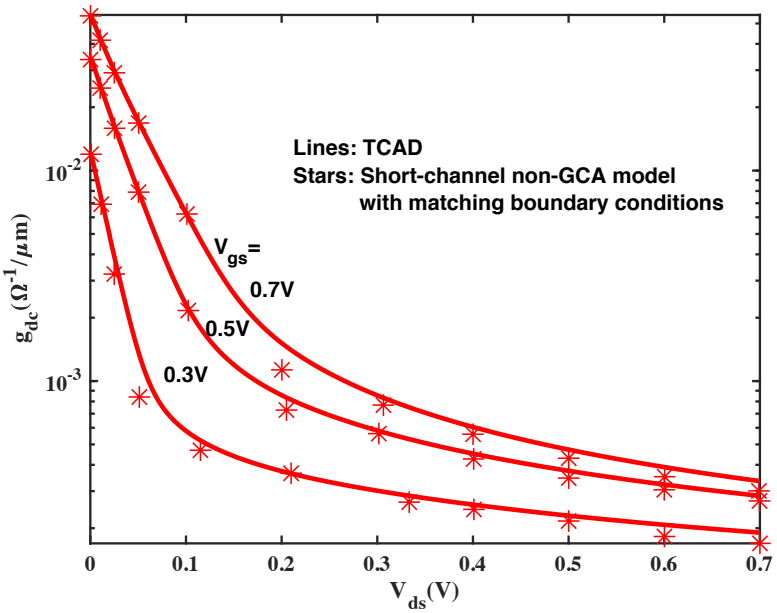

Figure 2.27: $g_{ds} \equiv dI_{ds}/dV_{ds}$ generated by this matching model with the source-drain depletion, compared with TCAD.

Figure 2.26 shows the $I_{ds} - V_{ds}$ characteristics generated by this model (matching model with the source-drain depletion). They are in good agreement with TCAD simulation results. Further verification of the output conductance $g_{dc} \equiv dI_{ds}/dV_{ds}$, by TCAD simulations are shown in Figure 2.27.

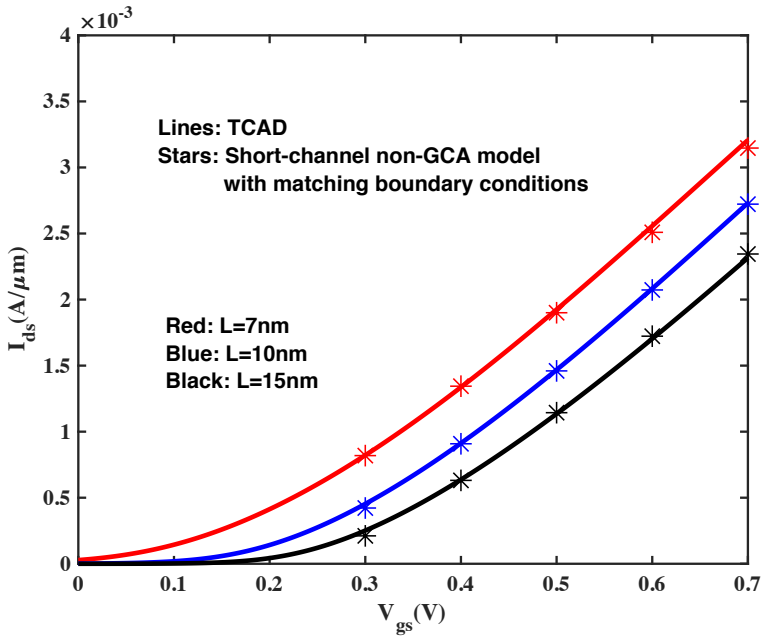

Figure 2.28: $I_{ds} - V_{gs}$ characteristics generated by this matching model for various channel lengths, compared with TCAD. $V_{ds} = 0.7V$.

Figure 2.28 shows the $I_{ds} - V_{gs}$ characteristics generated by this model for various channel lengths L at a fixed $V_{ds} = 0.7V$, which are consistent with TCAD simulations. The result of the device with length of $L = 7nm$ is slight off compared with TCAD simulations at high V_{gs} bias because the short-channel effect becomes rather severe.

2.5 $n = 2$ Velocity Saturation Model

In the $n = 1$ velocity saturation model, the current continuity Equation (2.18) is only applicable for the range of $\frac{dV}{dy} > 0$. When $\frac{dV}{dy} < 0$, the velocity-field relation becomes:

$$v = \frac{\mu_{eff} dV/dy}{1 - (\mu_{eff}/v_{sat}) dV/dy} \tag{2.35}$$

In other words, the current continuity equation for $n = 1$ velocity saturation model for the full range is given as:

$$I_{ds} = W t_{si} q n_i e^{q(\psi - V)/kT} \frac{\mu_{eff} dV/dy}{1 + \left(\frac{\mu_{eff}}{v_{sat}}\right) \left|\frac{dV}{dy}\right|} \tag{2.36}$$

It turns out that there is a discontinuity at $\frac{dV}{dy} = 0$ of Equation (2.36)[25]. To fix this problem, a $n = 2$ velocity saturation model can be employed where the current continuity equation (2.18) is replaced as[43], [62], [64], [65]:

$$I_{ds} = W t_{si} q n_i e^{\frac{q(\psi - V)}{kT}} \frac{\mu_{eff} \frac{dV}{dy}}{\sqrt{1 + \left(\frac{\mu_{eff}}{v_{sat}}\right)^2 \left(\frac{dV}{dy}\right)^2}} \tag{2.37}$$

Similarly, with the variable transformation technology, the coupled equation for solving $u(y)$ and $V(y)$ are constructed as:

$$\frac{d^2u}{dy^2} = \left(Wt_{si}qn_i\frac{\mu_{eff}}{I_{ds}}e^{\frac{qu}{kT}}\right)^2\frac{q}{kT}\frac{du}{dy}\left[\frac{\frac{I_{ds}}{\mu_{eff}}}{\sqrt{\left(Wqt_{si}n_ie^{\frac{qu}{kT}}\right)^2-\left(\frac{I_{ds}}{v_{sat}}\right)^2}}\right]^3$$

$$+\frac{q}{\varepsilon_{si}}n_ie^{\frac{qu}{kT}}-\frac{2C_{inv}(V_{gs}-V_t-V)}{\varepsilon_{si}t_{si}} \qquad (2.38)$$

$$\frac{dV}{dy} = \frac{\frac{I_{ds}}{\mu_{eff}}}{\sqrt{\left(Wqt_{si}n_ie^{\frac{qu}{kT}}\right)^2-\left(\frac{I_{ds}}{v_{sat}}\right)^2}} \qquad (2.39)$$

To avoid overestimating I_{ds} by the fixed boundary conditions discussed above, we also have to construct boundary conditions by matching the potential in the channel and that in the source and drain. The Poisson's equation in the source-drain regions is given as:

$$\frac{d^2u}{dy^2} = \left(Wt_{si}qn_i\frac{\mu_{eff}}{I_{ds}}e^{\frac{qu}{kT}}\right)^2\frac{q}{kT}\frac{du}{dy}\left[\frac{\frac{I_{ds}}{\mu_{eff}}}{\sqrt{\left(Wqt_{si}n_ie^{\frac{qu}{kT}}\right)^2-\left(\frac{I_{ds}}{v_{sat}}\right)^2}}\right]^3$$

$$+\frac{q}{\varepsilon_{si}}\left(n_ie^{\frac{qu}{kT}}-N_{S-D}\right) \qquad (2.40)$$

By expressing $u = u_{max} - \Delta u$ and keeping only the first-order of Δu, Equation (2.40) changes to:

$$\frac{d^2\Delta u}{dy^2}-\left(Wt_{si}qn_i\frac{\mu_{eff}}{I_{ds}}e^{\frac{qu}{kT}}\right)^2\frac{q}{kT}\left[\frac{\frac{I_{ds}}{\mu_{eff}}}{\sqrt{\left(Wqt_{si}n_ie^{\frac{qu}{kT}}\right)^2-\left(\frac{I_{ds}}{v_{sat}}\right)^2}}\right]^3\frac{d\Delta u}{dy}-\frac{q^2N_{S-D}}{\varepsilon_{si}kT}\Delta u=0 \quad (2.41)$$

In the source side, we can derive a boundary condition in a same form with Equation (2.28) at $y = 0$. In the drain side, we a solution for Equation (2.41) can also be constructed as:

$$u_{max}-u=[u_{max}-u(L)]e^{-K_2(y-L)} \quad (2.42)$$

where

$$K_2=-\frac{1}{2}\left[Wt_{si}qn_i\frac{\mu_{eff}}{I_{ds}}e^{\frac{qu(L)}{kT}}\right]^2\frac{q}{kT}\left[\frac{\frac{I_{ds}}{\mu_{eff}}}{\sqrt{\left(Wqt_{si}n_ie^{\frac{qu(L)}{kT}}\right)^2-\left(\frac{I_{ds}}{v_{sat}}\right)^2}}\right]^3$$

$$+\sqrt{\left\{\frac{1}{2}\left[Wt_{si}qn_i\frac{\mu_{eff}}{I_{ds}}e^{\frac{qu(L)}{kT}}\right]^2\frac{q}{kT}\left[\frac{\frac{I_{ds}}{\mu_{eff}}}{\sqrt{\left(Wqt_{si}n_ie^{\frac{qu(L)}{kT}}\right)^2-\left(\frac{I_{ds}}{v_{sat}}\right)^2}}\right]^3\right\}^2+\frac{q^2N_{S-D}}{\varepsilon_{si}kT}} \quad (2.43)$$

So that the boundary condition at $y = L$ is given as:

$$\frac{du}{dy}|_{y=L}=K_2[u_{max}-u(L)] \quad (2.44)$$

Another boundary condition of $V(0)$ can be written as:

$$V(0) = \frac{l_c}{2}\left[\frac{dV}{dy}|_{y=0} + \frac{dV}{dy}|_{y=-l_c}\right]$$

$$= \frac{l_c}{2}\left\{\frac{\frac{I_{ds}}{\mu_{eff}}}{\sqrt{\left[Wqt_{si}n_i e^{\frac{qu(0)}{kT}}\right]^2 - \left(\frac{I_{ds}}{v_{sat}}\right)^2}} + \frac{\frac{I_{ds}}{\mu_{eff}}}{\sqrt{(Wqt_{si}N_{S-D})^2 - \left(\frac{I_{ds}}{v_{sat}}\right)^2}}\right\} \quad (2.45)$$

By following the same approach of the matching model described in Section 2.4, we can construct the $I_{ds} - V_{ds}$ characteristics for $n = 2$ velocity saturation case.

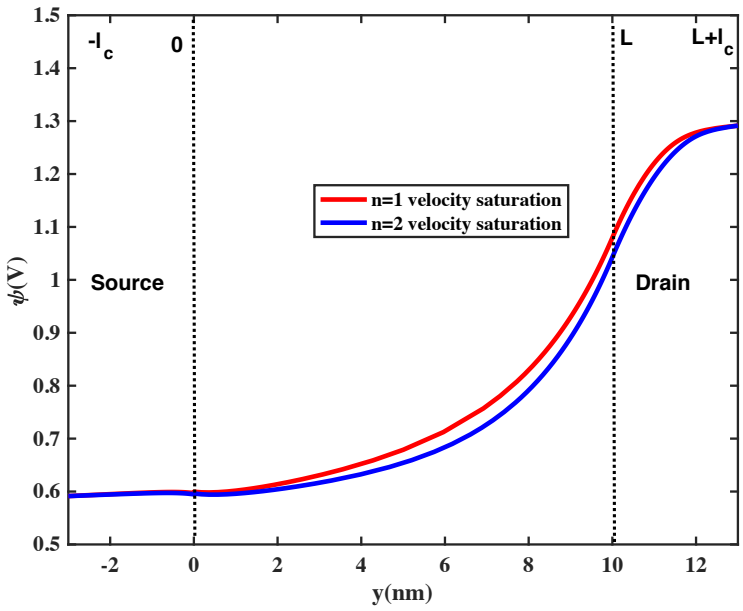

Figure 2.29: Comparison of Potential profile $\psi(y)$ generated from the $n = 1$ and $n = 2$ velocity saturation models. $N_{S-D} = 10^{20}cm^{-3}.V_{gs} = V_{ds} = 0.7V$.

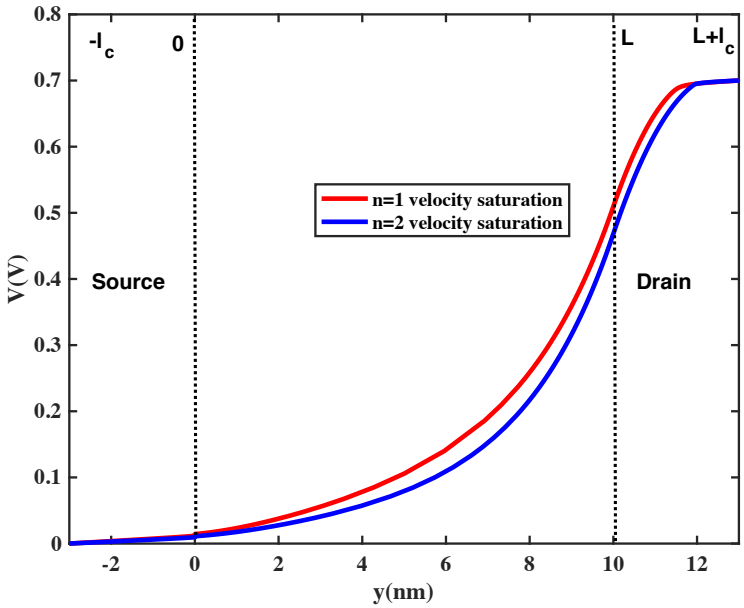

Figure 2.30: Comparison of quasi-Fermi Potential profile $V(y)$ generated from the $n = 1$ and $n = 2$ velocity saturation models. $N_{S-D} = 10^{20} cm^{-3}$. $V_{gs} = V_{ds} = 0.7V$.

Figures 2.29 and 2.30 show the potential $\psi(y)$ and quasi-Fermi potential $V(y)$, respectively, generated from the $n = 1$ and $n = 2$ velocity saturation models. It shows that both $n = 1$ and $n = 2$ models are able to describe the significant drops of potential and quasi-Fermi potential in the drain region. Figure 2.31 shows the $I_{ds} - V_{ds}$ characteristics generated by the $n = 2$ velocity saturation model, which is in consistent with TCAD simulations.

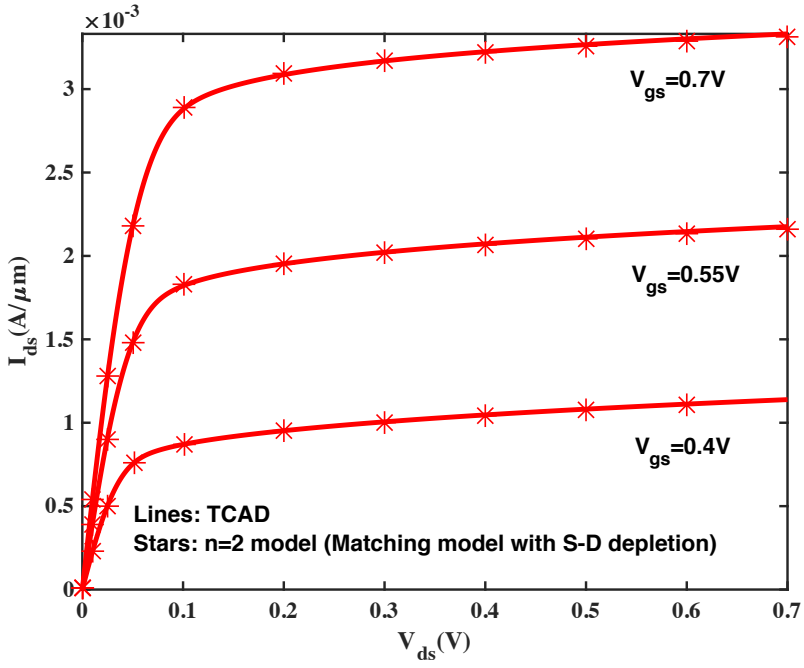

Figure 2.31: $I_{ds} - V_{ds}$ characteristics generated by the $n = 2$ model (matching model with S-D depletion) are compared with TCAD simulations.

2.6 Summary

In this chapter, an above-threshold $I_{ds} - V_{ds}$ model for short-channel double-gate (DG) MOSFETs is developed by taking into account the contribution from the source-drain encroachment effect to the carrier density. At low-drain biases, the source-drain encroachment effect (short-channel effect) appears as a gate-voltage dependent reduction of channel resistance. It is strong in subthreshold and weak in above threshold. At high-drain bias voltages, the encroachment of the source-drain bands intersects with the gate-controlled channel potential, resulting in a point of "virtual cathode", or minimum potential, at a small distance from the source. This non-GCA model is also extended to incorporate the effect of band bending caused by the

depletion of carriers in the source and drain region. By applying the $n = 1$ and $n = 2$ velocity saturation model, the $I_{ds} - V_{ds}$ and $I_{ds} - V_{gs}$ characteristics are generated and verified by TCAD simulations.

Chapter 2, in full, is a reprint of the material as it appears in "An Above Threshold Model for Short-Channel DG MOSFETs," by David Chuyang Hong and Yuan Taur, IEEE Trans. Electron Devices, Jul. 2021. The dissertation author was the primary investigator and author of this paper.

CHAPTER 3 SERIES RESISTANT MODEL FOR DG MOSFETS

On Chapter 2, we developed an above threshold $I_{ds} - V_{ds}$ model for short-channel DG MOSFET. High accuracies are achieved for both $n = 1$ and $n = 2$ velocity saturation models. It is worthwhile to note that what we discussed before are about the intrinsic DG MOSFETs[43], where the internal terminals are applied by the bias voltages V_{gs} and V_{ds} directly. Here perfectly conducting source and drain terminals are assumed so that there is no voltage drop showing in those regions. This is not valid in practice since there are finite metal contact resistance and silicon resistivity needed to be considered[43], [73]–[75]. The effect of the source-drain series resistant may significantly degrade the current when it is comparable with the channel resistance, which usually happens in the short-channel devices. In this chapter, we will first extend our short-channel non-GCA model to incorporate the source-drain series resistant effect. Then we will verify our model by the experimental data from Intel FinFET at 14nm[76].

3.1 Series Resistant Model

A real DG MOSFET can be modeled as an intrinsic part in series with the two parasitic resistances[43]. The schematic of the equivalent circuit of a real DG MOSFET is shown in Figure 4.1. R_d and R_s are the source and drain resistant, respectively. V_{gs} and V_{ds} are the external

applied bias voltages. $V_{gs}{}'\ and\ V_{ds}{}'$ are the internal voltage applied to the terminals of an intrinsic DG MOSFET. Two relations between them can be easily found:

$$V_{gs} = V_{gs}{}' + R_s I_{ds} \tag{3.1}$$

$$V_{ds} = V_{ds}{}' + R_{sd} I_{ds} = V_{ds}{}' + (R_s + R_d) I_{ds} \tag{3.2}$$

where $R_{sd} = R_s + R_d$.

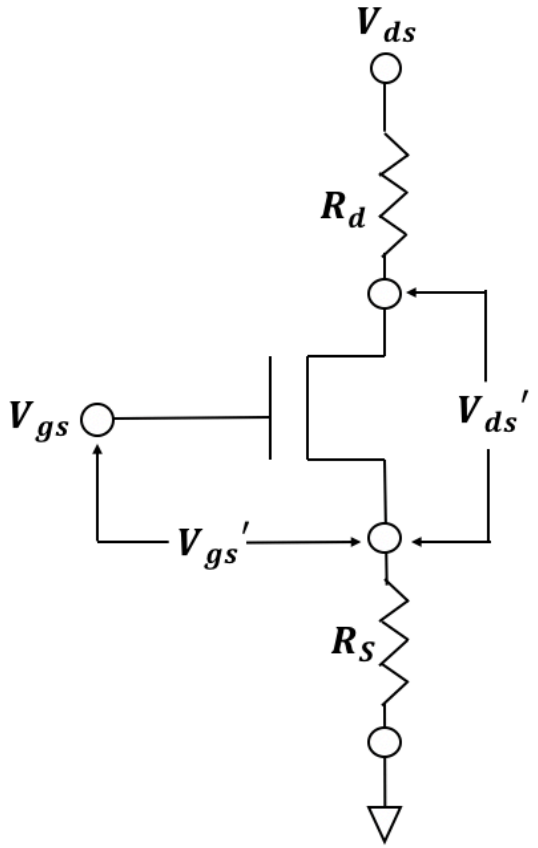

Figure 3.1: Schematic diagram showing the equivalent circuit of DG MOSFET with the source-drain series resistant[43].

In TCAD[55] and other conventional models[8], [77], [78], $I_{ds} - V_{ds}$ characteristics are generated by finding I_{ds} for given V_{gs} and V_{ds}. This indicates the unknown $V_{gs}{}'$ and $V_{ds}{}'$ has to be solved iteratively because they are needed parameters in Equations (3.1) and (3.2) and the model equations for intrinsic DGMOSFET. This iteration process is cumbersome and computationally expensive. In contrast, in our short-channel non-GCA model described in Chapter 2, $I_{ds} - V_{ds}$ characteristics are constructed by solving V_{ds} for given I_{ds} and V_{gs} so no iteration is needed.

Given I_{ds} and V_{gs}, we can get $V_{gs}{}'$ from Equation (3.1). With I_{ds} and $V_{gs}{}'$, the short-channel non-GCA model can be applied to calculate $V_{ds}{}'$, hence V_{ds} can be obtained from Equation (3.2). Finally, $I_{ds} - V_{ds}$ characteristic can be constructed. We can incorporate this process into our short-channel non-GCA model.

For $n = 1$ velocity saturation case, Equation (2.20) should be replaced as:

$$\frac{d^2u}{dy^2} = \frac{\left(\frac{q}{kT}\right)\left(\frac{I_{ds}}{\mu_{eff}}\right)}{\left(Wt_{si}qn_i e^{\frac{qu}{kT}} - \frac{I_{ds}}{v_{sat}}\right)^2} Wt_{si}qn_i e^{\frac{qu}{kT}} \frac{du}{dy} + \frac{q}{\varepsilon_{si}} n_i e^{\frac{qu}{kT}} - \frac{2C_{inv}{}'\left(V_{gs} - I_{ds}R_s - V_t - V\right)}{\varepsilon_{si}t_{si}} \quad (3.3)$$

where

$$C_{inv} = C_{ox} \frac{2r\beta_s{}' tan\beta_s{}'}{ln\beta_s{}' - \ln(cos\beta_s{}') + 2r\beta_s{}' tan\beta_s{}'} \quad (3.4)$$

and $\beta_s{}'$ is determined by:

$$V_{gs} - I_{ds}R_s - V_t = \frac{2kT}{q}[ln\beta_s' - \ln(\cos\beta_s') + 2r\beta_s' \tan\beta_s'] \tag{3.5}$$

After solving quasi-Fermi potential $V(y)$ from the coupled equation Equations (3.3) and (2.21), we get:

$$V_{ds}' = V(L + l_c) \tag{3.6}$$

Hence,

$$V_{ds} = V(L + l_c) + (R_s + R_d)I_{ds}. \tag{3.7}$$

Similarly, for $n = 2$ velocity saturation model, Equation (2.38) needs to be replaced by:

$$\frac{d^2u}{dy^2} = \left(Wt_{si}qn_i\frac{\mu_{eff}}{I_{ds}}e^{\frac{qu}{kT}}\right)^2 \frac{q}{kT}\frac{du}{dy}\left[\frac{\frac{I_{ds}}{\mu_{eff}}}{\sqrt{\left(Wqt_{si}n_ie^{\frac{qu}{kT}}\right)^2 - \left(\frac{I_{ds}}{v_{sat}}\right)^2}}\right]^3 + \frac{q}{\varepsilon_{si}}n_ie^{\frac{qu}{kT}} - \frac{2C_{inv}'\left(V_{gs} - I_{ds}R_s - V_t - V\right)}{\varepsilon_{si}t_{si}} \tag{3.8}$$

The coupled equations to solve the potential $\psi(y)$ and quasi-Fermi potential $V(y)$ are given by Equation (2.39) and (3.8). Then we can get one point on the $I_{ds} - V_{ds}$ characteristics by estimating V_{ds} from Equation (3.7).

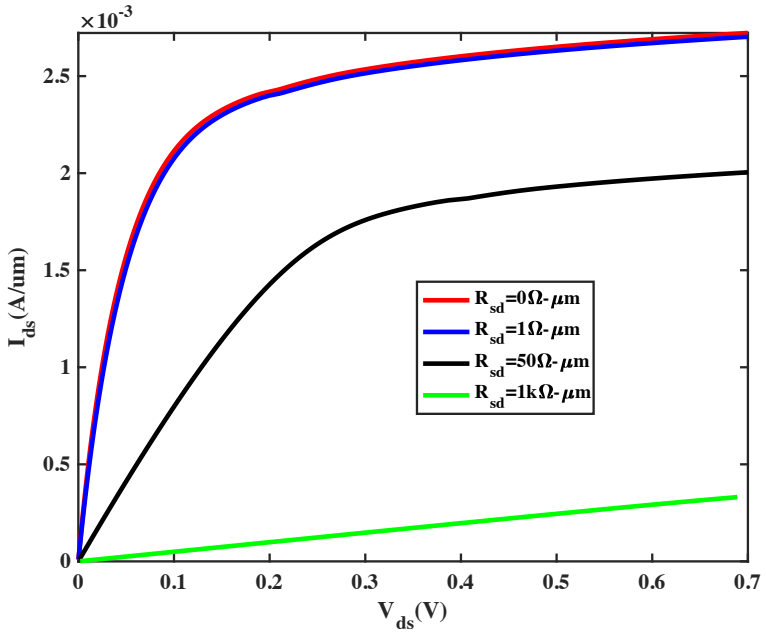

Figure 3.2: $I_{ds} - V_{ds}$ characteristics generated by the short-channel non-GCA model with considering various R_{sd}.

Table 3.1: Comparison of I_{ds} from models with and without R_{sd} for various V_{gs} and V_{ds}. Here $R_s = R_d = 50\Omega - \mu m$.

		I_{ds} *without* R_{sd} (A/um)	I_{ds} *with* R_{sd} (A/um)	*Decresed by*
$V_{gs} = 0.3V$	$V_{ds} = 0.01V$	1.0×10^{-4}	5.26×10^{-5}	47.4%
	$V_{ds} = 0.7V$	4.2205×10^{-4}	3.2648×10^{-4}	22.644%
$V_{gs} = 0.7V$	$V_{ds} = 0.01V$	4.8×10^{-4}	8.42×10^{-5}	82.458%
	$V_{ds} = 0.7V$	2.7223×10^{-3}	2.0045×10^{-3}	26.367%

Figure 3.2 shows plots the $I_{ds} - V_{ds}$ characteristics generated by the model with various R_{sd}. It shows that the source-drain resistant causes the degradation of current I_{ds} for various V_{gs}. When current I_{ds} flows into the device, it leads to some voltage drops in the source and drain due to the source-drain resistant. The resulted lower V_{gs} and V_{ds} applied in the intrinsic DG MOSFET (i.e., V_{gs}' and V_{ds}') causes the lowering of I_{ds} [43]. The slope of the curve in the linear region become lower for a higher R_{sd}. When the source-drain resistant is large (e.g., $1k\Omega - \mu m$ for this example), the device basically acts like a resistant. Table 3.1 compares the degree of I_{ds} degradation for various V_{gs} and V_{ds}. $V_{ds} = 0.01\ and\ 0.7V$ corresponds to the linear and the saturation regions, respectively. We can get two observations easily: (1) For the same V_{gs}, I_{ds} degradation is more severe in the linear region, compared with the saturation region. For example, for $V_{gs} = 0.7V$, 82.458% and 26.367% of I_{ds} degradations are observed for linear and saturation, respectively. (2) For the same V_{ds}, a more severe degradation occurs for higher gate-voltage overdrive. For example, $V_{ds} = 0.01V$, 47.4% and 82.458% of I_{ds} degradations are observed for $V_{gs} = 0.3\ and\ 0.7V$. This is because the channel resistance is lower in the linear region and for a higher V_{gs}, and the effect of the source-drain resistant becomes more prominent. Those observations are in consistent with our physical insights[43].

Table 3.2: Comparison of I_{ds} from models with and without R_{sd} for various L.

	$I_{ds}\ without\ R_{sd}$ (A/um)	$I_{ds}\ with\ R_{sd}$ (A/um)	$Decresed\ by$
$L = 7nm$	6.019×10^{-4}	8.73×10^{-5}	85.496%
$L = 10nm$	4.8×10^{-4}	8.42×10^{-5}	82.458%
$L = 15nm$	3.6×10^{-4}	7.95×10^{-5}	77.916%
$L = 20nm$	2.88×10^{-4}	7.53×10^{-5}	73.854%

Table 3.2 compares the I_{ds} degradation for various channel length L. It is clear that for a shorter channel, the effect of the source-drain resistant is more prominent, since the channel resistance is lower[43].

3.2 Intel Data Validation

To further validate our short-channel non-GCA model, we can fit it to the experimental data from Intel 14nm FinFET[76]. The parameters used in our model are given by Table 3.3. Note the effective channel length is estimated as $L = 20nm$. $R_s = R_d = 98\Omega - \mu m$ is used. Figure 3.2 compares the $I_{ds} - V_{ds}$ characteristics from the data and the result from our model. Close agreement is achieved.

Table 3.3: Parameters used for fitting Intel 14nm data[76].

$Parameters$	$Values$
ε_{si}	$11.8 \times \varepsilon_0$
ε_i	$6 \times \varepsilon_0$
t_{si}	$8nm$
t_i	$1nm$
v_{sat}	10^{-7}
μ_{eff}	200
L	$20nm$
N_{S-D}	$10^{-20}cm^{-3}$
l_c	$3nm$
V_t	$0.3185V$
R_s	$98\Omega - \mu m$
R_d	$98\Omega - \mu m$

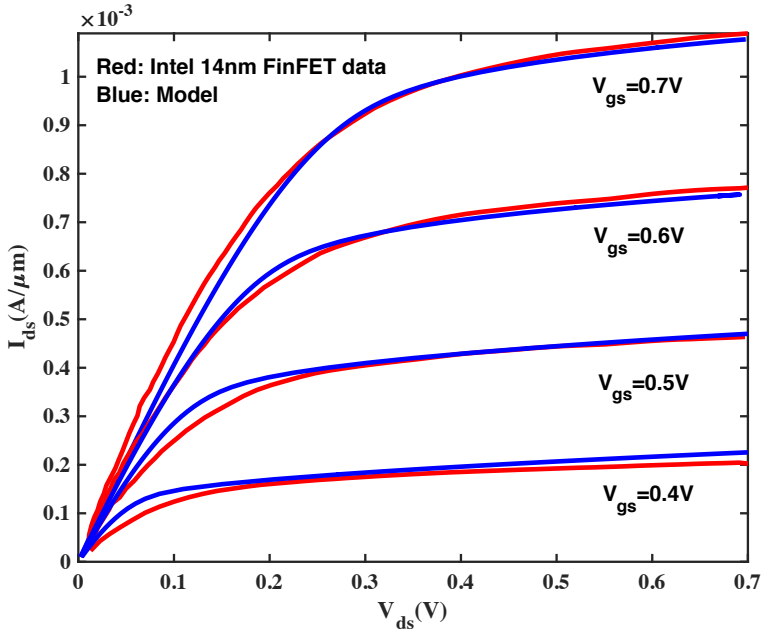

Figure 3.3: $I_{ds} - V_{ds}$ characteristics generated by the short-channel non-GCA model are verified by Intel 14nm FinFET data[76].

3.3 Summary

In this chapter, we incorporated the source-drain resistant effect into the short-channel non-GCA model. The effect of the source-drain resistant on the I_{ds} degradation is discussed. It shows the current degradation due to this effect becomes more severe in the linear region and for a higher V_{gs}. We also validate our model by fitting to the experimental data from the Intel 14nm FinFET. Close agreement is yielded.

CHAPTER 4 AN ABOVE THRESHOLD MODEL FOR BULK AND GROUND PLANE MOSFETS

In Chapter 2, we developed a short channel non-GCA model for DG MOSFET. It achieves great performance in predicting the above threshold $I_{ds} - V_{ds}$ characteristics. To apply the model to bulk and ground plane MOSFETs, we may encounter two problems: (1) The device structures of DG, bulk and ground plane MOSFETs are different, there are two gates for DG MOSFET while only one for bulk and ground plane MOSFETs. Some parameters like t_{si} is only applicable for DG MOSFET. (2) Unlike the DG MOSFET we discussed in Chapters 2 and 3 where the channel is undoped/lightly doped, the substrate of the bulk MOSFET is heavily/moderately doped in general[39], [43]. This means the fixed charge term in Poisson's equation for bulk MOSFET is not negligible. For ground plane MOSFET, the doping profile is even more complex[79], [80]. By keeping those in mind, we have to start from Poisson's equation again and develop a new short-channel non-GCA model framework for bulk and ground plane MOSFETs.

4.1 Short-Channel Non-GCA Model for Bulk MOSFET

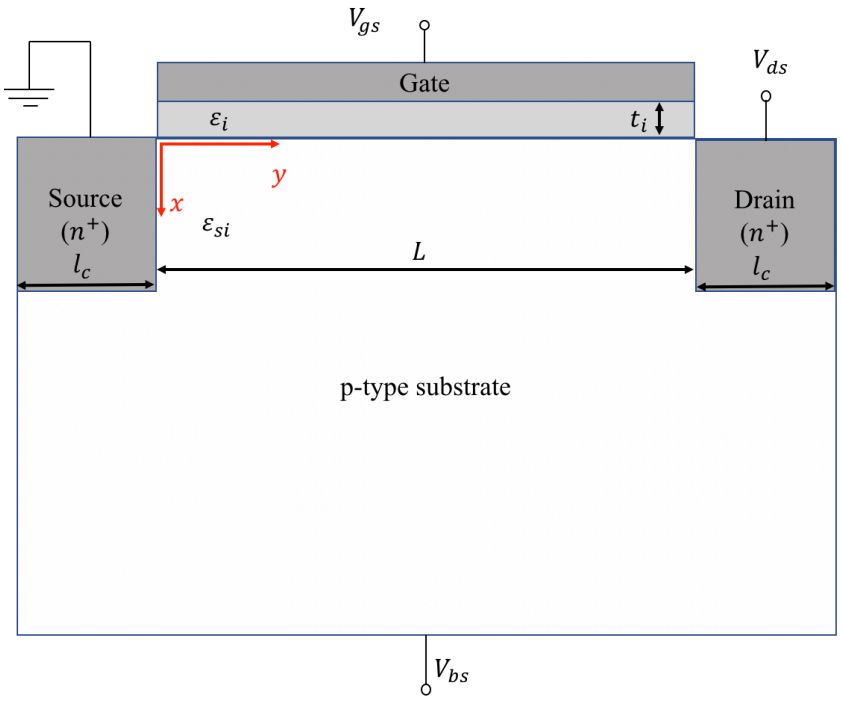

Figure 4.1: Schematic of bulk MOSFET cross section. $V_{bs} = 0$.

Figure 4.1 shows schematic of a bulk MOSFET cross section. Poisson's equation with the fixed charge term is given as:

$$\frac{\partial^2\psi}{\partial x^2} + \frac{\partial^2\psi}{\partial y^2} = \frac{q}{\varepsilon_{si}}\left[N_a + n_i e^{\frac{q(\psi - V)}{kT}}\right] \tag{4.1}$$

where N_a is the acceptor concentration of the p-type substrate[43]. The inversion charge density per area induced by the gate is written as:

$$Q_i = C_{inv}''\left(V_{gs} - V_t'' - mV\right) \tag{4.2}$$

where

$$m = 1 + \frac{\sqrt{\varepsilon_{si} q N_a / 4\psi_B}}{C_{ox}} \tag{4.3}$$

is the body effect coefficient and $\psi_B = (kT/q)\ln(N_a/n_i)$ [43]. C_{inv}'' and V_t'' are adjustable parameters that can be chosen for best fitting of the $Q_i(V_{gs})$ or $Q_i(V)$ curve for bulk MOSFETs.

For given V, Q_i is a function of V_{gs}, given by the charge-sheet model[44], [81], [82]:

$$Q_i = C_{ox}(V_{gs} - V_{fb} - \psi_s) - \sqrt{2\varepsilon_{si} q N_a \psi_s} \tag{4.4}$$

where V_{fb} is the flatband voltage and ψ_s is the surface potential which can be determined by[83]:

$$V_{gs} = V_{fb} + \psi_s + \frac{\sqrt{2\varepsilon_{si} kT N_a}}{C_{ox}} \left[\frac{q\psi_s}{kT} + \frac{{n_i}^2}{{N_a}^2} e^{\frac{q(\psi_s - V)}{kT}} \right]^{1/2} \tag{4.5}$$

Figure 4.2 shows that the charge sheet model tends to underestimate the total charge density Q_i in the above threshold region for device with long channel length. The key assumption of the charge sheet model is that the depletion charge is given by $Q_d = \sqrt{2\varepsilon_{si} q N_a \psi_s}$ for the entire bias range. While it is accurate below threshold, it overestimates Q_d above threshold because even though ψ_s increases slightly above threshold, Q_d stays constant once beyond the strong inversion region. We can derive a modified charge sheet model by replacing ψ_s in Q_d with $2\psi_B + V$:

$$Q_i = C_{ox}(V_{gs} - V_{fb} - \psi_s) - \sqrt{2\varepsilon_{si} q N_a (2\psi_B + V)} \tag{4.6}$$

It would be not valid below threshold, as shown in Figure 4.2 where the $Q_i < 0$ in the subthreshold region, but we are concerned with the above threshold only. It is obvious that $Q_i(V_{gs})$ generated by the modified charge sheet model is more accurate in the above threshold region.

Figure 4.3 compares the $I_{ds} - V_{ds}$ characteristic generated by the charge sheet model and modified charge sheet model and TCAD simulation. Due to the underestimation of Q_i, the charge sheet model predicted I_{ds} is off on the above threshold region. The modified charge sheet model is able to accurately predict the I_{ds} in the linear region. When the device enters into the saturation region, the modified charge sheet model also underestimates the I_{ds}. It is not a problem since we only utilize the result of the modified charge sheet model in the linear region to estimate C_{inv}'' and V_t'', which will be discussed later.

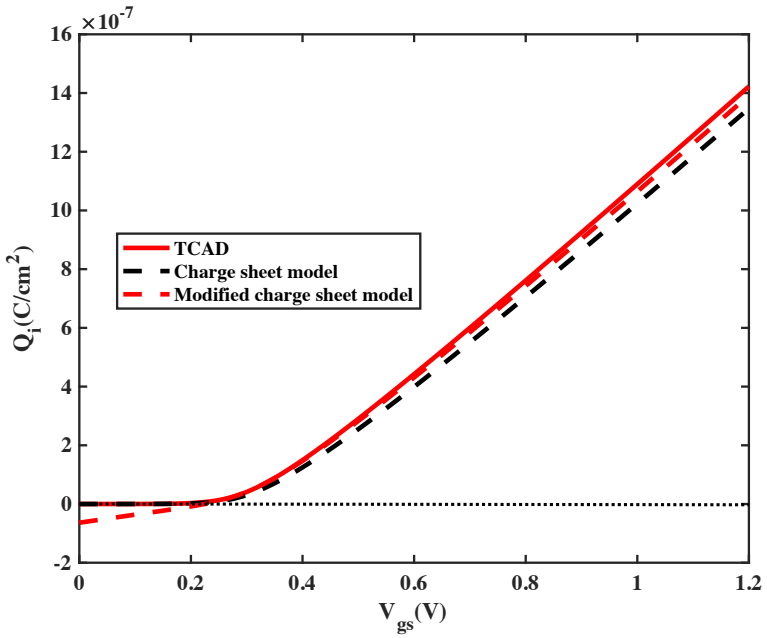

Figure 4.2: Comparison of $Q_i(V_{gs})$ generated by the charge sheet model[44], [83], modified charge sheet model and TCAD simulations for device with a long channel length $L = 500nm$. $V_{ds} = 0.001V$.

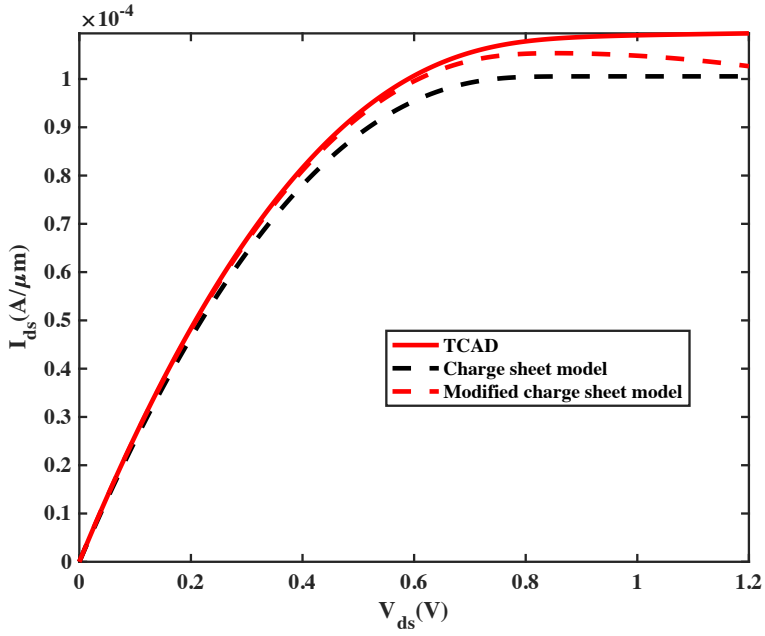

Figure 4.3: Comparison of $I_{ds} - V_{gs}$ generated by the charge sheet model[44], [83], modified charge sheet model and TCAD simulations for device with a long channel length $L = 1\mu m$. $V_{gs} = 1.2V$.

After generating a $Q_i(V)$ curve for a given V_{gs} from the modified charge sheet model (i.e., Equations (4.5) and (4.6)), we can extract two parameters:

$$a = Q_i|_{V=0} \tag{4.7}$$

$$b = -\frac{dQ_i}{dV}|_{V=0} \tag{4.8}$$

to fit a linear relation to the curve. From Equation (4.2), we have:

$$a = C_{inv}''\left(V_{gs} - V_t''\right) \tag{4.9}$$

$$b = mC_{inv}'' \tag{4.10}$$

Then we can extract:

$$C''_{inv} = \frac{-\frac{dQ_i}{dV}|_{V=0}}{m} \tag{4.11}$$

$$V''_t = V_{gs} - m\frac{Q_i|_{V=0}}{-\frac{dQ_i}{dV}|_{V=0}} \tag{4.12}$$

from each V_{gs} curve. Figure 4.4 shows that the fitting linear relation of Q_i from Equation (4.2) with C''_{inv} and V''_t extracted from Equations (4.11) and (4.12) are accurate when V_{ds} is not very large (e.g., $V_{ds} \leq 0.3V$), because C''_{inv} and V''_t are chosen to fit the value and slope of $Q_i(V)$ curve at $V = 0V$. When V_{ds} becomes larger, it may underestimate the Q_i and hence the saturation current:

$$I_{ds\_sat} = \mu_{eff}\left(\frac{W}{L}\right) * \int_0^{+\infty} Q_i(V)dV \tag{4.13}$$

A better improvement is to change to define a new variable b' such that the maximum area under the linear approximation $Q_{i\_lin}(V) = a - b'V$ curve, i.e., $a^2/(2b')$, equals $\int_0^{+\infty} Q_i(V)dV$ from the charge sheet model. In other words, b' is chosen such that $\mu_{eff}\left(\frac{W}{L}\right) * \frac{a^2}{2b'}$ equals I_{ds_sat} of charge sheet model given from Equation (4.13). Considering that the $Q_i(V)$ from modified charge sheet model becomes negative in the saturation region, we define b' as:

$$b' = \frac{a^2}{2\int_0^{V'} Q_i(V)dV} \tag{4.14}$$

here V' is the value of Q_i at V where $Q_i(V) = 0$. Hence, C_{inv}'' and V_t'' are extracted as:

$$C_{inv}'' = \frac{(Q_i|_{V=0})^2}{2m\int_0^{V'} Q_i(V)dV} \tag{4.15}$$

$$V_t'' = V_{gs} - m\frac{2\int_0^{V'} Q_i(V)dV}{Q_i|_{V=0}} \tag{4.16}$$

As shown in Figure 4.4, Equation (4.2) with Equations (4.15) and (4.16) is a good approximation of Q_i on the above threshold region. Figure 4.5 further verify the approximation by comparing it to the TCAD simulation.

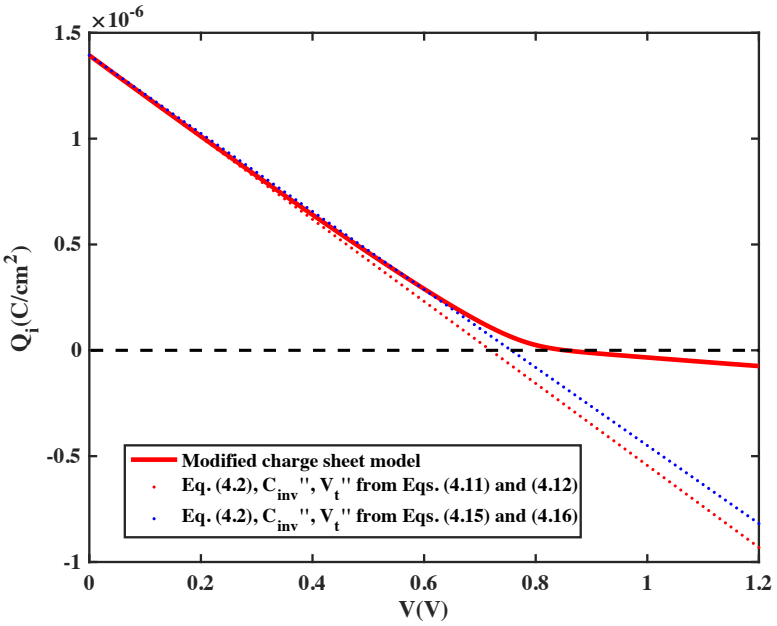

Figure 4.4: Comparison of $Q_i(V)$ generated by the modified charge sheet model, Equation (4.2) with C_{inv}'' and V_t'' extracted from Equations (4.11)-(4.12) and from Equations (4.15)-(4.16). $V_{gs} = 1.2V$.

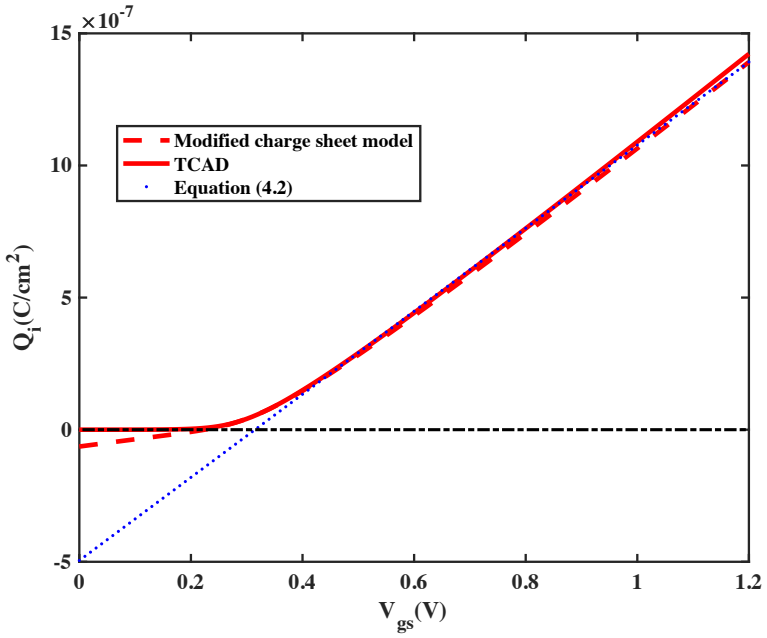

Figure 4.5: Comparison of $Q_i(V_{gs})$ generated by the modified charge sheet model, Equation (4.2) with C_{inv}'' and V_t'' extracted from Equations (4.15)-(4.16) at $V_{gs} = 1.2V$.

Equations (4.15) and (4.16) indicates the C_{inv}'' and V_t'' are $V_{gs}-$ dependent. We have to estimate C_{inv}'' and V_t'' for a given V_{gs}. Table 4.1 lists the C_{inv}'' and V_t'' extracted from the modified charge sheet model for several V_{gs}.

Table 4.1: C_{inv}'' and V_t'' extracted from the $Q_i(V)$ curves which are generated by the modified charge-sheet model.

	$C_{inv}''\ (\times 10^{-6} C/(cm^2 \cdot V))$	$V_t''\ (V)$
$V_{gs} = 1.2V$	1.5734	0.3143
$V_{gs} = 0.9V$	1.5290	0.3082
$V_{gs} = 0.6V$	1.3923	0.2890

Note that Q_i given by Equation (4.2) corresponds to the x-curvature term in the Equation (4.1). We can write down a 1-Dimensional equation in the x-direction:

$$\frac{d^2\psi}{dx^2} = \frac{q}{\varepsilon_{si}} N_a + \frac{C_{inv}''(V_{gs} - V_t'' - mV)}{\varepsilon_{si} d_{si}} \tag{4.17}$$

where d_{si} is the effective thickness, which is similar to t_{si} for DG MOSFET. In default, we set the value of d_{si} as x_j and x_j is the junction depth of the source-drain region. The junction depth x_j is an additional parameter that effects the short-channel effect of bulk MOSFETs, which is not taken into account in the short-channel non-GCA model for DG MOSFETs. Figure 4.6 compares the $I_{ds} - V_{ds}$ characteristics generated by TCAD simulation with different junction depth x_j. As the channel length scales down, the junction depth plays a more important role in $I_{ds} - V_{ds}$ characteristics. A shorter junction depth leads to a lower output conductance $g_{dc} \equiv dI_{ds}/dV_{ds}$ [84], [85].

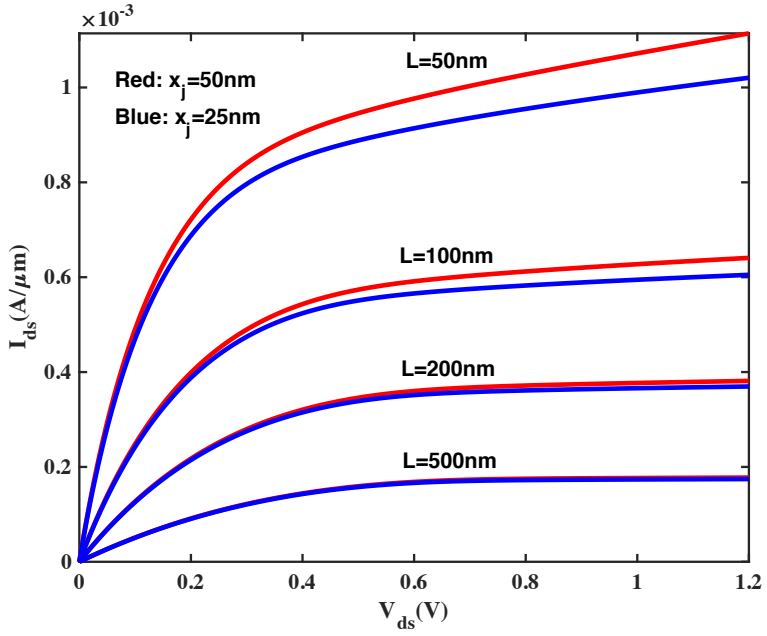

Figure 4.6: $I_{ds} - V_{ds}$ characteristics for MOSFETs generated by TCAD simulation with different junction depth x_j for various channel length L. $V_{gs} = 1.2V$.

Inserting Equation (4.17) into (4.1) yields:

$$\frac{d^2\psi}{dy^2} = \frac{q}{\varepsilon_{si}} n_i e^{q(\psi - V)/kT} - \frac{C_{inv}''(V_{gs} - V_t'' - mV)}{\varepsilon_{si} d_{si}} \tag{4.18}$$

Equation (4.18) is in a similar form as Equation (2.4) for DG MOSFET. The only difference is the second term in RHS. There is a "$2\times$" factor for DG MOSFET due to the symmetric structure along the x −direction. Moreover, for DG MOSFET, there is no body effect hence $m = 1$.

To construct the $I_{ds} - V_{ds}$ characterics, Equation (4.18) has to be coupled with the current continuity equation to solve the potential $\psi(y)$ and the quasi-Fermi potential $V(y)$. To avoid the tedious iterative calculation process, we can transform the variable to $u \equiv \psi - V$. For the constant mobility case, the coupled equations are given as:

$$\frac{d^2u}{dy^2} = \frac{q}{kT}\frac{I_{ds}}{\mu_{eff}Wqd_{si}n_i e^{\frac{qu}{kT}}}\frac{du}{dy} + \frac{q}{\varepsilon_{si}}n_i e^{\frac{qu}{kT}} - \frac{C_{inv}''\left(V_{gs} - V_t'' - mV\right)}{\varepsilon_{si}d_{si}} \tag{4.19}$$

$$\frac{dV}{dy} = \frac{I_{ds}}{\mu_{eff}Wqd_{si}n_i e^{\frac{qu}{kT}}} \tag{4.20}$$

Figure 4.7 compares the $I_{ds} - V_{ds}$ characteristics generated by the modified charge sheet model, short-channel non-GCA model and TCAD simulation for a device with long channel length $L = 1\mu m$. The short-channel non-GCA model is accurate, although the C_{inv}'' and V_t'' are extracted from the modified charge sheet model from which the I_{ds} predicted is off in the saturation region.

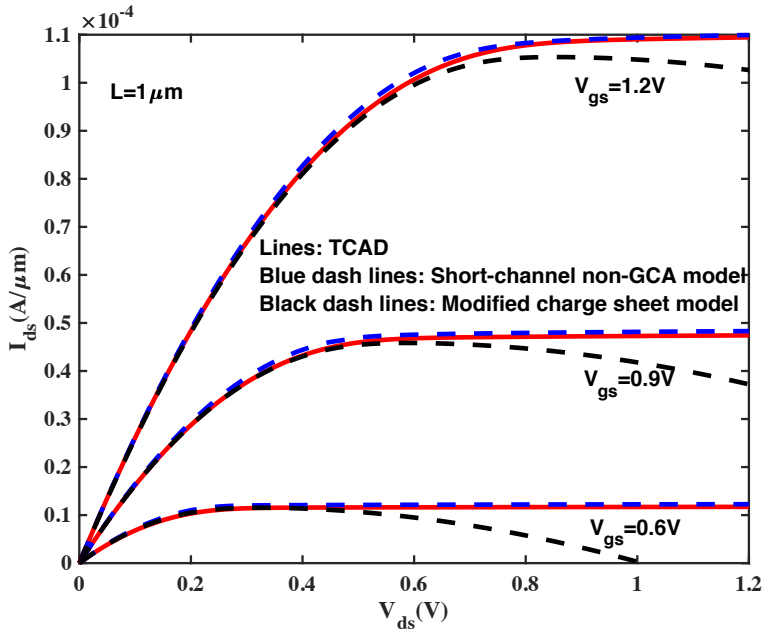

Figure 4.7: $I_{ds} - V_{ds}$ characteristics for MOSFETs generated by the modified charge sheet model, short-channel non-GCA model and TCAD simulation. $L = 1\mu m$.

For $n = 1$ velocity saturation case, the coupled equations are given as:

$$\frac{d^2u}{dy^2} = \frac{\left(\frac{q}{kT}\right)\left(\frac{I_{ds}}{\mu_{eff}}\right)}{\left(Wd_{si}qn_ie^{\frac{qu}{kT}} - \frac{I_{ds}}{v_{sat}}\right)^2} Wd_{si}qn_ie^{\frac{qu}{kT}}\frac{du}{dy} + \frac{q}{\varepsilon_{si}}n_ie^{\frac{qu}{kT}} - \frac{C_{inv}''\left(V_{gs} - V_t'' - mV\right)}{\varepsilon_{si}d_{si}} \quad (4.21)$$

$$\frac{dV}{dy} = \frac{I_{ds}/\mu_{eff}}{Wd_{si}qn_ie^{qu/kT} - I_{ds}/v_{sat}} \quad (4.22)$$

The three boundary conditions are given by Equations (2.17a)-(2.17c). For given I_{ds}, after the quasi-Fermi potential $V(y)$ is solved, we choose the value of $V(L)$ as V_{ds} so one point on the $I_{ds} - V_{ds}$ characteristics is gotten.

Figures 4.8(a)-(d) compare the $I_{ds} - V_{ds}$ characteristics generated by the short-channel non-GCA model ($n = 1$) and TCAD simulation. For a long channel device, the model is able to achieve high accuracy. But as the channel length becomes shorter, the result becomes worse. It shows that this model tends to underestimate SCE.

There are possible ways to further explore and improve: (1) The parameter d_{si} is simply assumed to be x_j by default, which is not accurate enough to predict the current behavior of the devices. Figure 4.9 shows that d_{si} plays an important role on the $I_{ds} - V_{ds}$ characteristics. A smaller d_{si} leads to a lower conductance $g_{dc} \equiv dI_{ds}/dV_{ds}$. High accuracy of prediction can only be achieved with a good choice of d_{si}. (2) Another possible reason for the inaccuracy of the model for bulk MOSFET is that the depletion charge N_a is not partitioned properly. The model considers all N_a to be gate depleted, whereas in reality part of N_a may be source-drain depleted. These point to a new direction of future work.

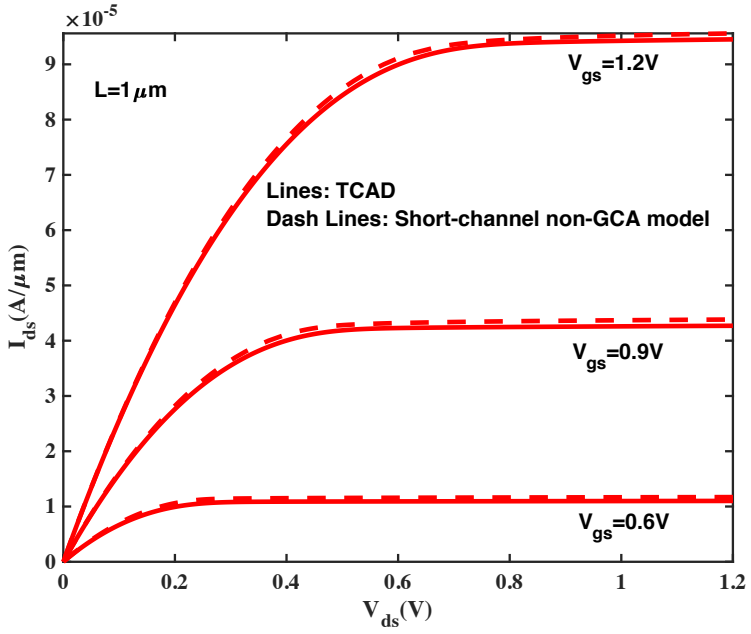

(a)

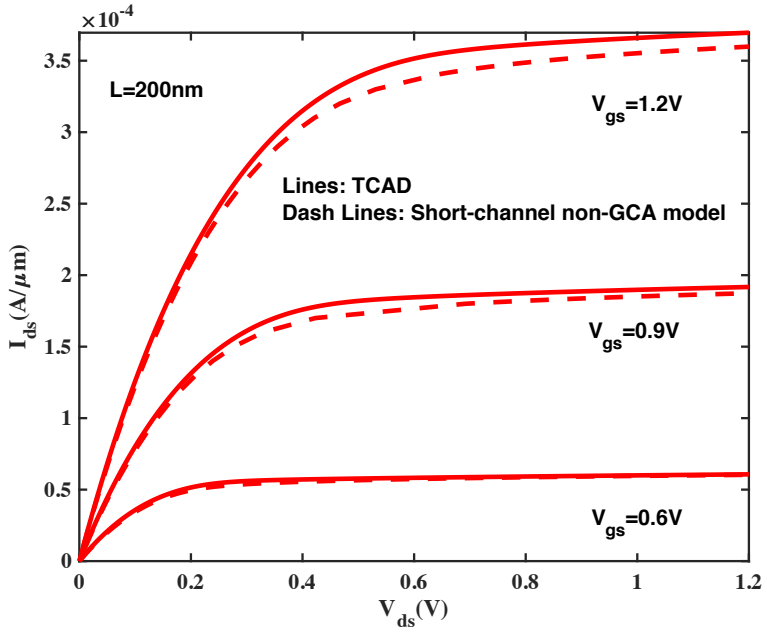

(b)

Figure 4.8: $I_{ds} - V_{ds}$ characteristics for MOSFETs generated by the short-channel non-GCA model (n=1) and TCAD simulation for (a) $L = 1\mu m$, (b) $L = 200nm$, (c) $L = 100nm$ and (d) $L = 50nm$. $d_{si} = x_j = 25nm$.

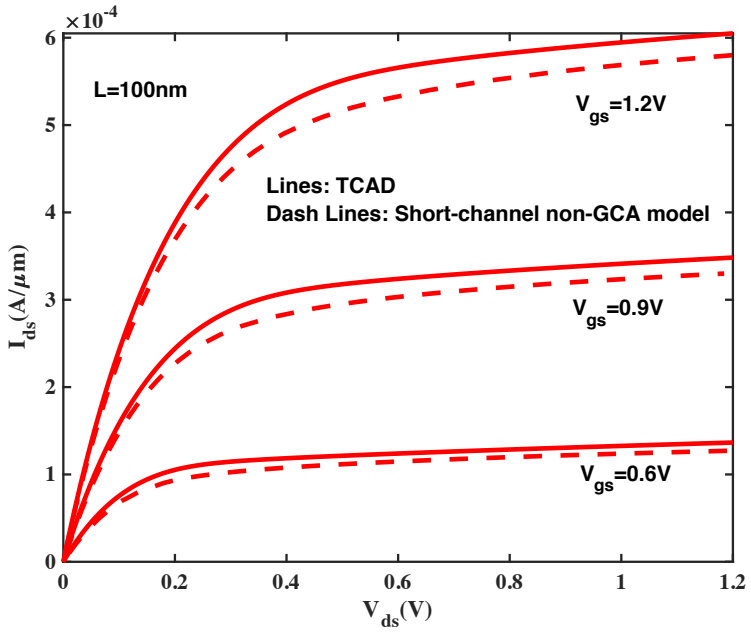

(c)

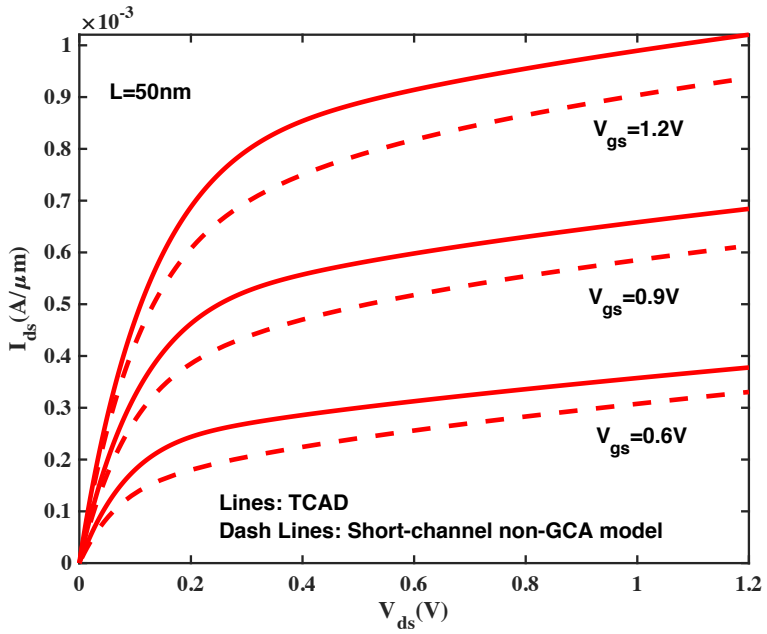

(d)

Figure 4.8: $I_{ds} - V_{ds}$ characteristics for MOSFETs generated by the short-channel non-GCA model (n=1) and TCAD simulation, continued.

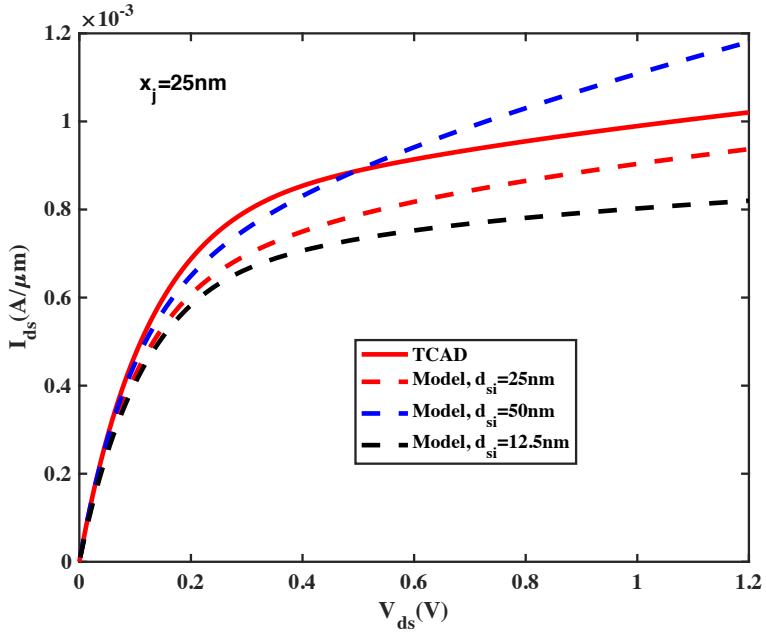

Figure 4.9: Comparison of $I_{ds} - V_{ds}$ characteristics generated by TCAD simulations and models with different d_{si}.

4.2 Short-Channel Non-GCA Model for Ground Plane MOSFET

Figure 4.10 shows the schematic of a ground plane MOSFET. Unlike the bulk MOSFET where the substrate is uniformly doped, an ideal ground plane MOSFET introduces a retrograde channel layer and a p^+ substrate layer above the p^- substrate layer so that the channel doping profile is of a low-high-low type[86]–[88]. Since the p^- substrate layer under p^+ substrate layer is for purpose of the junction capacitance reduction with no effect on SCE or $I_{ds} - V_{ds}$ characteristics, we can simplify the device structure with the doping profile of a low-high type, as shown in Figure 4.10. In the retrograde layer, the doping level is set to be 0. The doping

concentration of p^+ substrate layer is sufficiently high so that the depletion depth of the channel is the same as the retrograde layer depth t_u. This leads to a better performance of the ground plane MOSFET on the SCE, compared with the bulk MOSFET[37][89]. Figure 4.11 compares the $I_{ds} - V_{ds}$ characteristics for bulk and ground plane MOSFETs. Different gate work function values are set for the bulk and the ground plane MOSFETs so that their $I_{ds} - V_{ds}$ characteristics are the same for a long channel length. It shows that the ground plane MOSFET has a lower output conductance $g_{dc} \equiv dI_{ds}/dV_{ds}$ hence better performance.

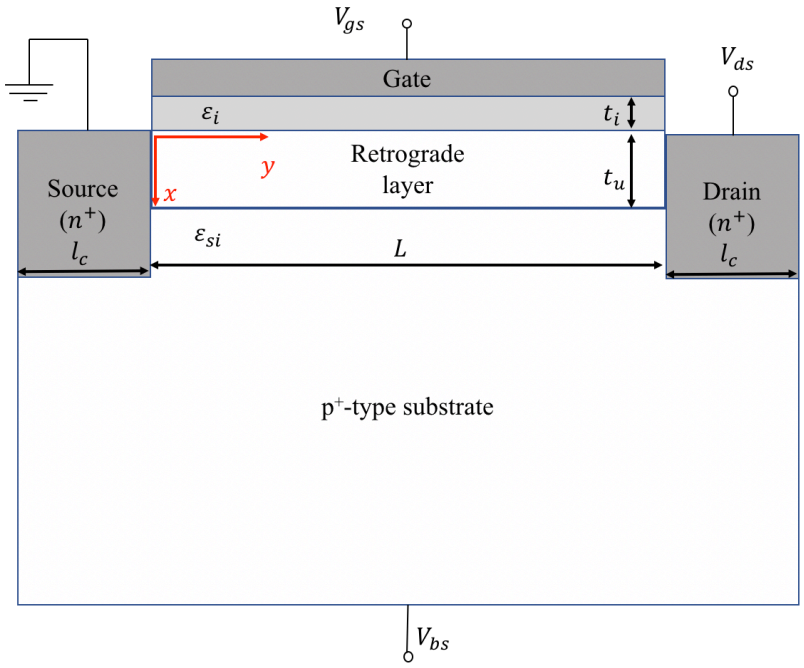

Figure 4.10: Schematic of ground plane MOSFET cross section. $V_{bs} = 0$.

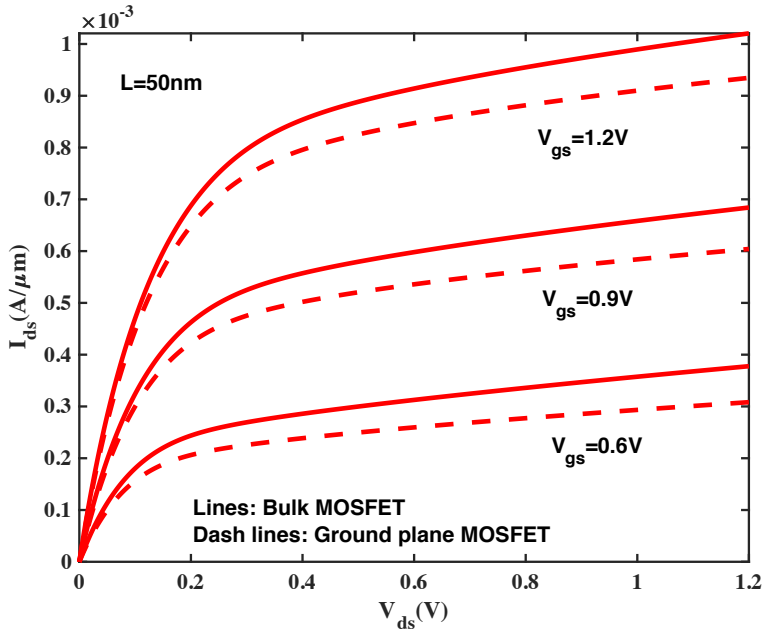

Figure 4.11: Comparison of $I_{ds} - V_{ds}$ characteristics generated by TCAD simulations for bulk and ground plane MOSFETs. Here different work function values are set for them so that they have the same $I_{ds} - V_{ds}$ characteristics for a long channel length.

Due to the similar structures between two types of MOSFETs, the model for bulk MOSFETs is also applicable for ground plane MOSFET, e.g., Equations. (4.21)-(4.22), where m is given by $m = 1 + \frac{3t_{ox}}{t_u}$. The parameters a and b (hence, $C_{inv}{}''$ and $V_t{}''$) are adjusted to fit the long channel (e.g., $L = 1\mu m$) $I_{ds} - V_{ds}$ characteristics. Figure 4.12 shows the $I_{ds} - V_{ds}$ characteristics generated by the short-channel non-GCA model are compared with TCAD simulation. Good agreement is observed while the conductance of the model is slightly higher than that of the TCAD simulation.

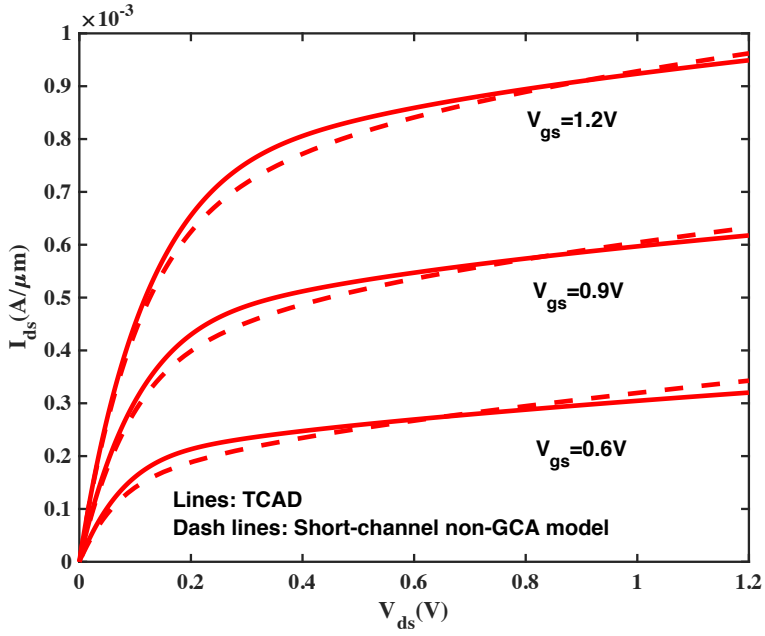

Figure 4.12: $I_{ds} - V_{ds}$ characteristics generated by the short-channel non-GCA model are compared with TCAD simulations for the ground plane MOSFET.

4.3 Summary

In the chapter, we applied the above threshold non-GCA model to short-channel bulk and ground plane MOSFETs. The source-drain encroachment effect is taken into account. It shows that junction depth is an additional parameter that affects SCE of bulk MOSFETs, which is not taken into account in the short-channel non-GCA model for DG MOSFETs. The charge sheet model is not accurate enough to fit C_{inv}, V_t for long channel MOSFETs and a modified charge sheet model is developed. For practical junction depths like $x_j = 25nm$, the short-channel non-GCA model tends to underestimate SCE. This points to a direction of future work.

Chapter 4, in part, is a reprint of the material as it appears in Section 6.2.1.5 “Fundamentals of Modern VLSI Devices, third edition” by Yuan Taur and Tak H. Ning, 2021. The dissertation author helped to complete this section.

CHAPTER 5 NUMERICAL METHODS FOR MODEL DEVELOPMENT

In previous Chapters, we developed multiple models, constructed by ordinary differential equation systems with initial conditions or boundary conditions in general. In most cases, we are unable to derive an analytic solution to the complicated differential equation system, so we have to solve it numerically. In this chapter, we will introduce two types of useful numerical methods for solving ordinary differential equations: Euler method and finite difference method. Then we will provide some practical suggestions and tradeoff discussions for using those methods.

5.1 Euler Method

Euler method is a well-known numerical method to solve ordinary differential equation system with initial condition[90]–[92]. Consider the general form of a first-order ordinary equation:

$$\frac{dz}{dx} = f(z(x), x) \tag{5.1}$$

with boundary condition:

$$z(a) = z_0{}' \tag{5.2}$$

Applying the Taylor Expansion of $z(x)$ around x_0 and using the first order approximation to express $\frac{dz}{dx}$ gets:

$$\frac{dz}{dx}|_{x=x_0} \approx \frac{z(x_0+h)-z(x_0)}{h} \tag{5.3}$$

where h is the step size. Substituting Equation (5.1) at $x = x_0$ into Equation (5.3) yields:

$$z(x_0+h) = z(x_0) + hf(z(x_0), x_0) \tag{5.4}$$

Equation (5.4) provides an approximate way to estimate the value of z at a point (i.e., $x_0 + h$) based on its value at its previous point (i.e., x_0). This is how the Euler method (or Forward Euler method) works. For higher order differential equation, the general form is given as:

$$\frac{d^n z}{dx^n} = f\left(z(x), \frac{dz}{dx}, \frac{d^2z}{dx^2}, \dots, \frac{d^{n-1}z}{dx^{n-1}};\ x\right) \tag{5.5}$$

We can apply variable transformation:

$$p_1 = z(x)$$

$$p_2 = \frac{dz}{dx}$$

$$\vdots$$

$$p_{n-1} = \frac{d^{n-2}z}{dx^{n-2}}$$

$$p_n = \frac{d^{n-1}z}{dx^{n-1}} \tag{5.6}$$

so that Equation (5.5) transform to a first-order system that can be solved by Euler method:

$$\frac{d\boldsymbol{p}}{dx} = \begin{pmatrix} \frac{dp_1}{dx} \\ \frac{dp_2}{dx} \\ \vdots \\ \frac{dp_{n-1}}{dx} \\ \frac{dp_n}{dx} \end{pmatrix} = \begin{pmatrix} p_2 \\ p_3 \\ \vdots \\ p_n \\ f(p_1, p_2, p_3, \dots, p_n, x) \end{pmatrix} \tag{5.7}$$

For example, in Ref [1], a second-order differential equation to be solved is given as:

$$\frac{d^2\psi}{dx^2} = \frac{q}{\varepsilon_{si}} n_i e^{q\psi/kT} \tag{5.8}$$

with the initial condition:

$$\psi(x = 0) = \psi_0 \tag{5.9a}$$

$$\frac{d\psi}{dx}|_{x=x_0} = 0 \tag{5.9a}$$

The analytical solution is given as:

$$\psi = \psi_0 - \frac{2kT}{q} \ln\left[cos\left(\sqrt{\frac{q^2 n_i}{2\varepsilon_{si} kT}} e^{\frac{q\psi_0}{2kT}} x\right)\right] \tag{5.10}$$

If we use Euler method to solve it numerically, we can construct the first-order system:

$$\frac{d\boldsymbol{p}}{dx} = \begin{pmatrix} \frac{dp_1}{dx} \\ \frac{dp_2}{dx} \end{pmatrix} = \begin{pmatrix} p_2 \\ \frac{q}{\varepsilon_{si}} n_i e^{qp_1/kT} \end{pmatrix} \tag{5.11}$$

where

$$p_1 = \psi \tag{5.12a}$$

$$p_2 = \frac{d\psi}{dx} \tag{5.12a}$$

The iterative equation is given by:

$$\boldsymbol{p}(x_0 + h) = \begin{pmatrix} p_1(x_0 + h) \\ p_2(x_0 + h) \end{pmatrix} = \begin{pmatrix} p_1(x_0) \\ p_2(x_0) \end{pmatrix} + h \begin{pmatrix} p_2(x_0) \\ \frac{q}{\varepsilon_{si}} n_i e^{qp_1(x_0)/kT} \end{pmatrix} \tag{5.13}$$

Figure 5.1 shows the $\psi(x)$ solved from Equation (5.8) using Euler method is in great consistent with analytical solution.

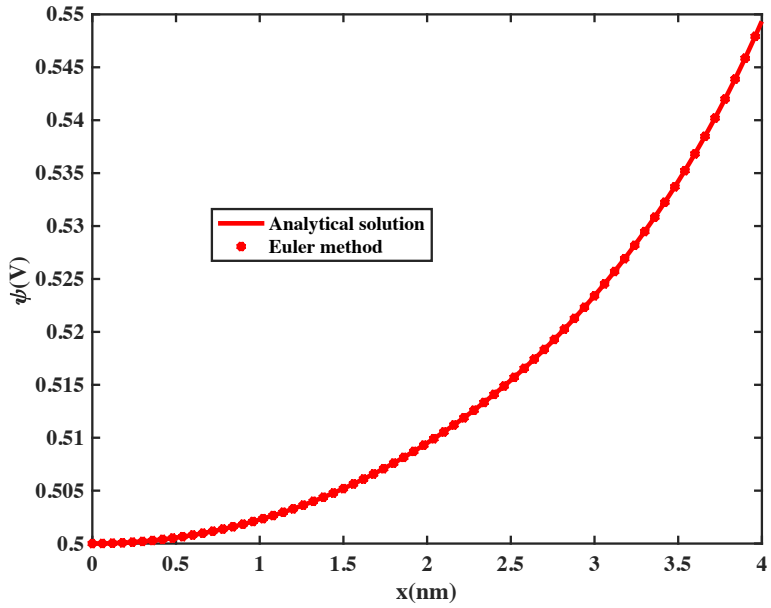

Figure 5.1: $\psi(x)$ solved from Equation (5.8) using Euler method is compared with analytical solution. $\psi_0 = 0.5V$.

Although Euler method is explicit and simple, it has two limitations: (1) It is numerical unstable, when there are some terms in the equation that may cause the solution to change rapidly[93]–[95]. To avoid this stability problem, some other variants can be considered, like backward Euler method[91] and midpoint method[96], etc. (2) It is applicable for problem with initial conditions, rather than boundary condition[92], [95]. In our low drain case in the short-channel non-GCA model for DG MOSFET, the second-order differential equation (i.e., Equation (2.5)) is similar with Equation (5.8). However, it is not easy to be solve using Euler method, because it is with Dirichlet boundary condition[97] (i.e., Equation (2.6)) and the initial value of $p_2 = \frac{d\psi}{dy}$ is difficult to be found. To fix this problem, some other method, like the Shooting method[98], [99] and Finite differences method[56], [100]–[102], can be tried.

5.2 Finite-Difference Method

In finite-difference method, the differential equation is solved by approximating the derivative as the finite difference[100]–[103]. Consider a first order differential equation in the form of Equation (5.1) in the domain of $[a, b]$ with initial condition (5.2), the finite-difference method first partitions the domain into a sequence of subdomain. The length of each subdomain is h. The ith domain's end point is denoted as x_i and its corresponding function value is z_i. The $\frac{dz}{dx}$ at x_i is approximated as:

$$\frac{dz}{dx}|_{x=x_i} = \frac{z_{i+1} - z_{i-1}}{2h} \tag{5.14}$$

Equations (5.1) and (5.2) turn to be:

$$F_0(z_0, z_1, z_2, z_3, \dots, z_{n-1}, z_n, z_{n+1}, \boldsymbol{x}) = z_0 - z_0' \tag{5.15a}$$

$$F_i(z_0, z_1, z_2, \dots, z_n, z_{n+1}, \boldsymbol{x}) = z_{i-1} + 2hf(z_i, x_i) - z_{i+1} = 0, i = 1,2,3,4 \dots n, n+1. \tag{5.15b}$$

Equation (5.15) forms a system of equations:

$$\boldsymbol{F}(\boldsymbol{z}, \boldsymbol{x}) = \begin{pmatrix} F_0(z_0,z_1,z_2,z_3,\dots,z_{n-1},z_n,z_{n+1},\boldsymbol{x}) \\ F_1(z_0,z_1,z_2,z_3,\dots,z_{n-1},z_n,z_{n+1},\boldsymbol{x}) \\ F_2(z_0,z_1,z_2,z_3,\dots,z_{n-1},z_n,z_{n+1},\boldsymbol{x}) \\ \vdots \\ F_n(z_0,z_1,z_2,z_3,\dots,z_{n-1},z_n,z_{n+1},\boldsymbol{x}) \\ F_{n+1}(z_0,z_1,z_2,z_3,\dots,z_{n-1},z_n,z_{n+1},\boldsymbol{x}) \end{pmatrix} = \boldsymbol{0} \tag{5.16}$$

The assignment turns to find a root vector $\boldsymbol{z} = (z_0, z_1, z_2, z_3, \dots, z_{n-1}, z_n, z_{n+1})^T$ for linear/nonlinear system (5.16). This can be solved numerically by Newton's method that will be discussed in next subsection. For a second order differential equation,

$$\frac{d^2z}{dx^2} = f\left(z(x), \frac{dz}{dx}, x\right) \tag{5.17}$$

with two boundary conditions:

$$z(a) = z_a \tag{5.18a}$$

$$z(b) = z_b \tag{5.18a}$$

We can introduce a second-order finite difference approximation:

$$\frac{d^2z}{dx^2}\Big|_{x=x_i} = \frac{z_{i+1} - 2z_i + z_{i-1}}{h^2} \tag{5.19}$$

Equations (5.17)-(5.18) transformed to:

$$F_i(z_0, z_1, \dots, z_n, z_{n+1}, \boldsymbol{x}) = \frac{z_{i+1} - 2z_i + z_{i-1}}{h^2} - f\left(z_i, \frac{z_{i+1} - z_{i-1}}{2h}, x_i\right) = 0,$$

$$i = 1,2,3 \dots n. \tag{5.20a}$$

$$F_0(z_0, z_1, \dots, z_n, z_{n+1}, \boldsymbol{x}) = z_0 - z_a = 0 \tag{5.20b}$$

$$F_{n+1}(z_0, z_1, \dots, z_n, z_{n+1}, \boldsymbol{x}) = z_{n+1} - z_b = 0 \tag{5.20c}$$

Equation (5.20) constructed an equation system in the form of (5.16) to be solved. We can take the short-channel non-GCA model in the low drain bias (i.e., Equation (2.5) with boundary condition (2.6)) as an example. The nonlinear system to be solved is built as:

$$\boldsymbol{F}(\boldsymbol{\psi}, \boldsymbol{x}) = \begin{pmatrix} F_0(\psi_0, \psi_1, \dots, \psi_n, \psi_{n+1}, \boldsymbol{x}) \\ F_1(\psi_0, \psi_1, \dots, \psi_n, \psi_{n+1}, \boldsymbol{x}) \\ F_2(\psi_0, \psi_1, \dots, \psi_n, \psi_{n+1}, \boldsymbol{x}) \\ \vdots \\ F_n(\psi_0, \psi_1, \dots, \psi_n, \psi_{n+1}, \boldsymbol{x}) \\ F_{n+1}(\psi_0, \psi_1, \dots, \psi_n, \psi_{n+1}, \boldsymbol{x}) \end{pmatrix}$$

$$= \begin{pmatrix} \psi_0 - \left(\frac{kT}{q}\right) \ln\left(\frac{N_{S-D}}{n_i}\right) \\ \frac{\psi_2 - 2\psi_1 + \psi_0}{h^2} - \frac{q}{\varepsilon_{si}} n_i e^{\frac{q\psi_1}{kT}} + \frac{2C_{inv}(V_{gs} - V_t)}{\varepsilon_{si} t_{si}} \\ \frac{\psi_3 - 2\psi_2 + \psi_1}{h^2} - \frac{q}{\varepsilon_{si}} n_i e^{\frac{q\psi_2}{kT}} + \frac{2C_{inv}(V_{gs} - V_t)}{\varepsilon_{si} t_{si}} \\ \vdots \\ \frac{\psi_{n+1} - 2\psi_n + \psi_{n-1}}{h^2} - \frac{q}{\varepsilon_{si}} n_i e^{\frac{q\psi_n}{kT}} + \frac{2C_{inv}(V_{gs} - V_t)}{\varepsilon_{si} t_{si}} \\ \psi_{n+1} - \left(\frac{kT}{q}\right) \ln\left(\frac{N_{S-D}}{n_i}\right) \end{pmatrix} = \mathbf{0} \quad (5.21)$$

The result is shown in Figure 2.2. For higher-order differential equations, the higher-order derivative $\frac{d^n z}{dx^n}$ has to be approximated by the corresponding finite difference. For example, for fourth-order derivative,

$$\frac{d^4 z}{dx^4}\Big|_{x=x_i} = \frac{z_{i+2} - 4z_{i+1} + 6z_i - 4z_{i-1} + z_{i-2}}{h^4} \quad (5.22)$$

For more complicate cases, like the system of differential equations with Neumann boundary condition[97] (e.g., the short-channel non-GCA high drain bias case with matching boundary conditions), similar approach can be applied.

5.3 Newton's Method

In subsection 5.2, we used finite-difference method to convert the ordinary differential equation into systems of equations. Those systems of equations are usually nonlinear and not easy to find the analytic solution. A useful method to find the root of systems of equations numerically is Newton's method[104]–[106]. Consider a simple case, given a function $z = f(x)$ and its derivative $f'(x) = \frac{dz}{dx}$, the tangent line of $f(x)$ at x_i is given:

$$z = f(x_i) + f'(x_i)(x - x_i) \tag{5.23}$$

Newton's method treats the x-intercept of this line as the next guess point to approach the root:

$$x_{i+1} = x_i - \frac{f(x_i)}{f'(x_i)} \tag{5.24}$$

Given an initial guess x_0, Equation (5.24) can be used to generate a sequence of points iteratively, which finally converge to the root of function (if the convergence conditions are satisfied). For the system of equations $\boldsymbol{F}(\boldsymbol{x}) = \boldsymbol{0}$, a similar form of iterative equation can be derived:

$$\boldsymbol{x_{i+1}} = \boldsymbol{x_i} - \boldsymbol{J}(\boldsymbol{x_i})^{-1}\boldsymbol{F}(\boldsymbol{x_i}) \tag{5.25}$$

where $\boldsymbol{J}(\boldsymbol{x})$ denotes the Jacobian matrix of $\boldsymbol{F}(\boldsymbol{x})$ [107]. By choosing a good initial guess $\boldsymbol{x_0}$, Equation (5.25) can be applied iteratively to get the approximate root of the equation system.

5.4 Experience and Improvement

In the previous subsections, we discussed Euler method and the finite difference method with Newton's method to solve the ordinary differential equations. The Euler method is easy to implement, when the differential equation is with initial condition, we can first try the Euler method. If the differential equation is with boundary condition, like Dirichlet or Neumann boundary conditions, the Shooting method can be considered.

For some complicate differential equations that contains some terms changing rapidly in the range, Euler method may fail to converge since it is numerically unstable. In this case, we should switch to consider the finite-difference method. This method works for various types of boundary conditions.

One difficulty for finite-difference method is how to set up appropriate initial guess required by Newton's method[98], [105]. The strategy is to choose a guess vector that is as close to the target solution as possible. For example, in our short-channel non-GCA model, when the drain bias is low, the potential $\psi(y)$ doesn't change rapidly in large part of the region and its value range is small (e.g., 0.55~0.65V). The upper bound is $\psi(0)\ and\ \psi(L)$ given by Equation (2.6); the lower bound is:

$$\psi\left(\frac{L}{2}\right) = \frac{kT}{q} ln\left[\frac{2C_{inv}\left(V_{gs} - V_t\right)}{qn_i t_{si}}\right] \tag{5.26}$$

We can set a constant initial guess $\psi_{initial}(y) = C_1$, where C_1 is a constant that is between $\psi(0)$ $(or\ \psi(L))$ and $\psi\left(\frac{L}{2}\right)$. Since most part of the derivative of potential $\frac{d\psi}{dy}$ and quasi-Fermi potential $V(y)$ are small in the low drain bias, we can also set a constant initial guess for $\left(\frac{d\psi}{dy}\right)_{initial}(y) = C_2$ and $V_{initial}(y) = C_3$, where C_2 and C_3 are constants of a small value (e.g., $\ll 10^{-3}$). However, those constant initial guesses are unable to work for high drain bias cases. The strategy is to use the result of previous bias point as the initial guess of the current I_{ds} point. For example, if we have solved the $\psi(y)$ and $V(y)$ at $I_{ds} = 5 \times 10^{-3} A/um$, then we can use those result as initial guess of $I_{ds} = (5 + C_4) \times 10^{-3} A/um$, where C_4 is a small increment of I_{ds}.

Another problem is how to select an appropriate increment of I_{ds}. When the increment of I_{ds} is too large, Newton's method will fail to converge to a correct solution based on the initial guess from the previous bias point, since the $\psi(y)$ and $V(y)$ change a lot with respective to a small variation of I_{ds}; When the increment of I_{ds} is too small, it is time-consuming and resource expensive since it has to repeat the solving process for more I_{ds} points than necessary. The strategy is to first set a large value of I_{ds} increment, if it doesn't work, then try a smaller increment until it works.

The final question is the implementation of finite difference method is cumbersome. Given a coupled differential equation set, we have to discretize the domain, convert the equations and boundary conditions into system of equations. In Newton's method, we are also required to write down the Jacobian matrix explicitly. It is easy to make mistake in the implementation process. It is good to know that the finite-difference method and Newton's method have been packaged as

built-in functions in some software, like MATLAB. We can use those function (e.g., bvp4c and bvp5c in MATLAB[57]–[61]) directly to carry out calculations.

5.5 Summary

In this Chapter, we discussed two useful methods for solving differential equations system in the models. Euler method is simple but numerically unstable. It is applicable to the problem with initial condition, rather than boundary conditions. Finite-difference method converts the ordinary differential equation sets into system of equations, which can be solved by Newton's method. It is powerful but requires appropriate initial guess. Some tradeoff considerations and strategy suggestion based on our experience are provided.

CHAPTER 6 CONCLUSION AND FUTURE WORK

6.1 Conclusion

In this dissertation, a short-channel non-GCA model framework is developed for DG MOSFETs by taking into account the encroachment of the source and drain bands into the channel. Interesting physical insights are obtained from the model: At low drain case, the source-drain encroachment effect results in a gate-dependent reduction of channel resistance, which is stronger at low gate voltage overdrive and weaker at high gate voltage overdrive; At high drain case, the intersection between the encroachment of source-drain bands (carrier spillover) and the gate-controlled channel potential gives rise to a point of "virtual cathode" at a small distance from the source; The effect of depletion in the source and drain region plays an important role on the channel potential in the short channel device at the scale of $L = 10nm$. The effect of the source-drain series resistance has been discussed. By incorporating the velocity saturation effect, the $I_{ds} - V_{ds}$ and $I_{ds} - V_{gs}$ characteristics are generated by the model and shown to be in good agreement with TCAD simulations.

We also apply the short-channel non-GCA model to bulk and the ground plane MOSFET. It shows that junction depth is an additional parameter that affect SCE of bulk MOSFETs, which is not taken into account in the short-channel non-GCA model for DG MOSFETs. The charge sheet model is not accurate enough to fit parameters like C_{inv}, V_t for long channel MOSFETs and

a modified charge sheet model is developed. For practical junction depths like $x_j = 25nm$, the model tends to underestimate the short channel effects.

6.2 Future Work

This work provides a useful $I - V$ model framework for modeling the above threshold behavior for short-channel DG MOSFETs. Some importance effects in the short-channel device, such as the source-drain encroachment effect, the effect of the depletion in the source and drain region, and the source-drain series resistant effect, are taken into account and good results are yielded. However, there are several aspects that can be further improved in the future works:

(1) This model is only applicable for above threshold region, it is worthwhile to extend it to cover the subthreshold region so that an all-region model can be constructed.

(2) When the physical dimension of the device shrinks into the deep nanometer regime, the quantum effect become prominent. It is good to incorporate the quantum effect into the model.

(3) When solving the model, we still have to carry out tedious numerical calculation, which is time consuming and resource expensive. Another improvement is to derive an analytic model that can be used in the practical EDA tools.

REFERENCES

[1] Y. Taur, “An analytical solution to a double-gate MOSFET with undoped body,” *IEEE Electron Device Lett.*, vol. 21, no. 5, pp. 245–247, 2000.

[2] Y. Taur, X. Liang, W. Wang, and H. Lu, “A continuous, analytic drain-current model for DG MOSFETs,” *IEEE Electron Device Lett.*, vol. 25, no. 2, pp. 107–109, 2004.

[3] H. Lu, B. Yu, and Y. Taur, “A unified charge model for symmetric double-gate and surrounding-gate MOSFETs,” *Solid. State. Electron.*, vol. 52, no. 1, pp. 67–72, 2008.

[4] F. Lime, B. Iniguez, and O. Moldovan, “A quasi-two-dimensional compact drain–current model for undoped symmetric double-gate MOSFETs including short-channel effects,” *IEEE Trans. Electron Devices*, vol. 55, no. 6, pp. 1441–1448, 2008.

[5] G. Dessai, A. Dey, G. Gildenblat, and G. D. J. Smit, “Symmetric linearization method for double-gate and surrounding-gate MOSFET models,” *Solid. State. Electron.*, vol. 53, no. 5, pp. 548–556, 2009.

[6] V. Hariharan, J. Vasi, and V. R. Rao, “Drain current model including velocity saturation for symmetric double-gate MOSFETs,” *IEEE Trans. Electron Devices*, vol. 55, no. 8, pp. 2173–2180, 2008.

[7] Y. S. Chauhan, S. Venugopalan, N. Paydavosi, P. Kushwaha, S. Jandhyala, J. P. Duarte, S. Agnihotri, C. Yadav, H. Agarwal, and A. Niknejad, “BSIM compact MOSFET models for SPICE simulation,” in *Proceedings of the 20th International Conference Mixed Design of Integrated Circuits and Systems-MIXDES 2013*, 2013, pp. 23–28.

[8] N. Paydavosi, S. Venugopalan, Y. S. Chauhan, J. P. Duarte, S. Jandhyala, A. M. Niknejad, and C. C. Hu, “BSIM—SPICE models enable FinFET and UTB IC designs,” *IEEE Access*, vol. 1, pp. 201–215, 2013.

[9] A. Ortiz-Conde, F. J. Garcia-Sanchez, J. Muci, S. Malobabic, and J. J. Liou, “A review of core compact models for undoped double-gate SOI MOSFETs,” *IEEE Trans. Electron Devices*, vol. 54, no. 1, pp. 131–140, 2006.

[10] Q. Chen, E. M. Harrell, and J. D. Meindl, "A physical short-channel threshold voltage model for undoped symmetric double-gate MOSFETs," *IEEE Trans. Electron Devices*, vol. 50, no. 7, pp. 1631–1637, 2003.

[11] B. Yu, H. Lu, M. Liu, and Y. Taur, "Explicit continuous models for double-gate and surrounding-gate MOSFETs," *IEEE Trans. Electron Devices*, vol. 54, no. 10, pp. 2715–2722, 2007.

[12] B. Iñiguez, T. A. Fjeldly, A. Lázaro, F. Danneville, and M. J. Deen, "Compact-modeling solutions for nanoscale double-gate and gate-all-around MOSFETs," *IEEE Trans. Electron Devices*, vol. 53, no. 9, pp. 2128–2142, 2006.

[13] M. Reyboz, O. Rozeau, T. Poiroux, P. Martin, and J. Jomaah, "An explicit analytical charge-based model of undoped independent double gate MOSFET," *Solid. State. Electron.*, vol. 50, no. 7–8, pp. 1276–1282, 2006.

[14] A. Cerdeira, B. Iniguez, and M. Estrada, "Compact model for short channel symmetric doped double-gate MOSFETs," *Solid. State. Electron.*, vol. 52, no. 7, pp. 1064–1070, 2008.

[15] J. Song, B. Yu, Y. Yuan, and Y. Taur, "A review on compact modeling of multiple-gate MOSFETs," *IEEE Trans. Circuits Syst. I Regul. Pap.*, vol. 56, no. 8, pp. 1858–1869, 2009.

[16] Y. S. Chauhan, S. Venugopalan, M. A. Karim, S. Khandelwal, N. Paydavosi, P. Thakur, A. M. Niknejad, and C. C. Hu, "BSIM—Industry standard compact MOSFET models," in *2012 Proceedings of the European Solid-State Device Research Conference (ESSDERC)*, 2012, pp. 46–49.

[17] X. J. Xi, J. He, M. Dunga, H. Wan, M. Chan, C.-H. Lin, B. Heydari, A. M. Niknejad, and C. Hu, "BSIM5 MOSFET Model," in *Proceedings. 7th International Conference on Solid-State and Integrated Circuits Technology, 2004.*, 2004, vol. 2, pp. 920–923.

[18] Y. Cheng and C. Hu, *MOSFET modeling & BSIM3 user's guide*. Springer Science & Business Media, 1999.

[19] D. P. Foty, *MOSFET modeling with SPICE: principles and practice*. Prentice-Hall, Inc., 1997.

[20] Y. S. Chauhan, R. Gillon, B. Bakeroot, F. Krummenacher, M. Declercq, and A. M. Ionescu, "An EKV-based high voltage MOSFET model with improved mobility and drift model,"

Solid. State. Electron., vol. 51, no. 11–12, pp. 1581–1588, 2007.

[21] M. Miura-Mattausch, U. Feldmann, A. Rahm, M. Bollu, and D. Savignac, "Unified complete MOSFET model for analysis of digital and analog circuits," *IEEE Trans. Comput. Des. Integr. circuits Syst.*, vol. 15, no. 1, pp. 1–7, 1996.

[22] T. Sakurai and A. R. Newton, "A simple MOSFET model for circuit analysis," *IEEE Trans. Electron Devices*, vol. 38, no. 4, pp. 887–894, 1991.

[23] M. Shur, T. A. Fjeldly, T. Ytterdal, and K. Lee, "Unified MOSFET model," *Solid. State. Electron.*, vol. 35, no. 12, pp. 1795–1802, 1992.

[24] G. Gildenblat, H. Wang, T.-L. Chen, X. Gu, and X. Cai, "SP: An advanced surface-potential-based compact MOSFET model," *IEEE J. Solid-State Circuits*, vol. 39, no. 9, pp. 1394–1406, 2004.

[25] K. Joardar, K. K. Gullapalli, C. C. McAndrew, M. E. Burnham, and A. Wild, "An improved MOSFET model for circuit simulation," *IEEE Trans. Electron Devices*, vol. 45, no. 1, pp. 134–148, 1998.

[26] G. Gildenblat, X. Li, W. Wu, H. Wang, A. Jha, R. Van Langevelde, G. D. J. Smit, A. J. Scholten, and D. B. M. Klaassen, "PSP: An advanced surface-potential-based MOSFET model for circuit simulation," *IEEE Trans. Electron Devices*, vol. 53, no. 9, pp. 1979–1993, 2006.

[27] R. Van Langevelde and F. M. Klaassen, "An explicit surface-potential-based MOSFET model for circuit simulation," *Solid. State. Electron.*, vol. 44, no. 3, pp. 409–418, 2000.

[28] N. Arora, *Mosfet modeling for VLSI simulation: theory and practice*. World Scientific, 2007.

[29] Y. S. Chauhan, M. A. Karim, S. Venugopalan, S. Khandelwal, P. Thakur, N. Paydavosi, A. B. Sachid, A. Niknejad, and C. Hu, "BSIM6: Symmetric bulk MOSFET model," in *Nanotechnology 2012: Electronics, Devices, Fabrication, MEMS, Fluidics and Computational-2012 NSTI Nanotechnology Conference and Expo, NSTI-Nanotech 2012*, 2012, pp. 724–729.

[30] M. Miura-Mattausch, H. Ueno, M. Tanaka, H. J. Mattausch, S. Kumashiro, T. Yamaguchi, K. Yamashita, and N. Nakayama, "HiSIM: A MOSFET model for circuit simulation

connecting circuit performance with technology," in *Digest. International Electron Devices Meeting,* 2002, pp. 109–112.

[31] T. L. Chen and G. Gildenblat, "Analytical approximation for the MOSFET surface potential," *Solid. State. Electron.*, vol. 45, no. 2, pp. 335–339, 2001.

[32] X. Liang and Y. Taur, "A 2-D analytical solution for SCEs in DG MOSFETs," *IEEE Trans. Electron Devices*, vol. 51, no. 9, pp. 1385–1391, 2004.

[33] H. Lu and Y. Taur, "An analytic potential model for symmetric and asymmetric DG MOSFETs," *IEEE Trans. Electron Devices*, vol. 53, no. 5, pp. 1161–1168, 2006.

[34] Y. Cheng, K. Chen, K. Imai, and C. Hu, "A unified MOSFET channel charge model for device modeling in circuit simulation," *IEEE Trans. Comput. Des. Integr. circuits Syst.*, vol. 17, no. 8, pp. 641–644, 1998.

[35] J. He, X. Xi, H. Wan, M. Dunga, M. Chan, and A. M. Niknejad, "BSIM5: An advanced charge-based MOSFET model for nanoscale VLSI circuit simulation," *Solid. State. Electron.*, vol. 51, no. 3, pp. 433–444, 2007.

[36] D. J. Frank, Y. Taur, and H.-S. Wong, "Generalized scale length for two-dimensional effects in MOSFETs," *IEEE Electron Device Lett.*, vol. 19, no. 10, pp. 385–387, 1998.

[37] Q. Xie, J. Xu, and Y. Taur, "Review and critique of analytic models of MOSFET short-channel effects in subthreshold," *IEEE Trans. Electron Devices*, vol. 59, no. 6, pp. 1569–1579, 2012.

[38] N. Pandey, H.-H. Lin, A. Nandi, and Y. Taur, "Modeling of short-channel effects in DG MOSFETs: Green's function method versus scale length model," *IEEE Trans. Electron Devices*, vol. 65, no. 8, pp. 3112–3119, 2018.

[39] S. M. Sze, Y. Li, and K. K. Ng, *Physics of semiconductor devices*. John wiley & sons, 2021.

[40] K. Seeger, *Semiconductor physics*. Springer Science & Business Media, 2013.

[41] W. W. DPG, L. S. EPS, R. Leturcq, S. Gustavsson, B. Simovic, R. Schleser, T. Ihn, P. Studerus, K. Ensslin, and D. C. Driscoll, "Semiconductor physics," 1978.

[42] C. Siu, “Semiconductor physics,” in *Electronic Devices, Circuits, and Applications*, Springer, 2022, pp. 35–39.

[43] Y. Taur and T. H. Ning, *Fundamentals of modern VLSI devices*. Cambridge university press, 2021.

[44] J. R. Brews, “A charge-sheet model of the MOSFET,” *Solid. State. Electron.*, vol. 21, no. 2, pp. 345–355, 1978.

[45] W. Shockley, “A unipolar" field-effect" transistor,” *Proc. IRE*, vol. 40, no. 11, pp. 1365–1376, 1952.

[46] H. C. Pao and C.-T. Sah, “Effects of diffusion current on characteristics of metal-oxide (insulator)-semiconductor transistors,” *Solid. State. Electron.*, vol. 9, no. 10, pp. 927–937, 1966.

[47] Y. Taur and H.-H. Lin, “Modeling of DG MOSFET $ I $–$ V $ Characteristics in the Saturation Region,” *IEEE Trans. Electron Devices*, vol. 65, no. 5, pp. 1714–1720, 2018.

[48] Y. A. El-Mansy and A. R. Boothroyd, “A simple two-dimensional model for IGFET operation in the saturation region,” *IEEE Trans. Electron Devices*, vol. 24, no. 3, pp. 254–262, 1977.

[49] P. K. Ko, R. S. Muller, and C. Hu, “A unified model for hot-electron currents in MOSFET’s,” in *1981 International Electron Devices Meeting*, 1981, pp. 600–603.

[50] Y. Taur, W. Choi, J. Zhang, and M. Su, “A non-GCA DG MOSFET model continuous into the velocity saturation region,” *IEEE Trans. Electron Devices*, vol. 66, no. 3, pp. 1160–1166, 2019.

[51] C.-T. Sah, “Characteristics of the metal-oxide-semiconductor transistors,” *IEEE Trans. Electron Devices*, vol. 11, no. 7, pp. 324–345, 1964.

[52] T. L. Chen and G. Gildenblat, “An extended analytical approximation for the MOSFET surface potential,” *Solid. State. Electron.*, vol. 49, no. 2, pp. 267–270, 2005.

[53] D. Jimenez, B. Iniguez, J. Sune, L. F. Marsal, J. Pallares, J. Roig, and D. Flores, “Continuous analytic IV model for surrounding-gate MOSFETs,” *IEEE Electron Device*

Lett., vol. 25, no. 8, pp. 571–573, 2004.

[54] B. Iniguez, D. Jimenez, J. Roig, H. A. Hamid, L. F. Marsal, and J. Pallarès, "Explicit continuous model for long-channel undoped surrounding gate MOSFETs," *IEEE Trans. Electron Devices*, vol. 52, no. 8, pp. 1868–1873, 2005.

[55] I. Silvaco, "ATLAS user's manual device simulation software," *St. Clara, CA*, 2010.

[56] R. J. LeVeque, *Finite difference methods for ordinary and partial differential equations: steady-state and time-dependent problems*. SIAM, 2007.

[57] D. J. Higham and N. J. Higham, *MATLAB guide*. SIAM, 2016.

[58] S. M. Toolbox, "Matlab," *Mathworks Inc*, 1993.

[59] N. Hale and D. R. Moore, "A sixth-order extension to the MATLAB package bvp4c of J. Kierzenka and L. Shampine," 2008.

[60] A. Ü. Keskin, "Solution of BVPs using bvp4c and bvp5c of MATLAB," in *Boundary value problems for engineers*, Springer, 2019, pp. 417–510.

[61] L. F. Shampine, J. Kierzenka, and M. W. Reichelt, "Solving boundary value problems for ordinary differential equations in MATLAB with bvp4c," *Tutor. notes*, vol. 2000, pp. 1–27, 2000.

[62] R. Troutman and S. Chakravarti, "Subthreshold characteristics of insulated-gate field-effect transistors," *IEEE Trans. Circuit Theory*, vol. 20, no. 6, pp. 659–665, 1973.

[63] D. M. Caughey and R. E. Thomas, "Carrier mobilities in silicon empirically related to doping and field," *Proc. IEEE*, vol. 55, no. 12, pp. 2192–2193, 1967.

[64] C. G. Sodini, P.-K. Ko, and J. L. Moll, "The effect of high fields on MOS device and circuit performance," *IEEE Trans. Electron Devices*, vol. 31, no. 10, pp. 1386–1393, 1984.

[65] G. W. Taylor, "Velocity-Saturated Characteristics of Short-Channel MOSFETs," *AT&T Bell Lab. Tech. J.*, vol. 63, no. 7, pp. 1325–1404, 1984.

[66] J. Min, J. Wu, and Y. Taur, "Analysis of source doping effect in tunnel FETs with staggered bandgap," *IEEE Electron Device Lett.*, vol. 36, no. 10, pp. 1094–1096, 2015.

[67] Y. Taur, C. H. Wann, and D. J. Frank, "25 nm CMOS design considerations," in *International Electron Devices Meeting 1998. Technical Digest (Cat. No. 98CH36217)*, 1998, pp. 789–792.

[68] H.-H. Lin and Y. Taur, "Effect of source–drain doping on subthreshold characteristics of short-channel DG MOSFETs," *IEEE Trans. Electron Devices*, vol. 64, no. 12, pp. 4856–4860, 2017.

[69] A. Nandi, A. K. Saxena, and S. Dasgupta, "Analytical modeling of a double gate MOSFET considering source/drain lateral Gaussian doping profile," *IEEE Trans. Electron Devices*, vol. 60, no. 11, pp. 3705–3709, 2013.

[70] M. Liu, M. Cai, B. Yu, and Y. Taur, "Effect of gate overlap and source/drain doping gradient on 10-nm CMOS performance," *IEEE Trans. Electron Devices*, vol. 53, no. 12, pp. 3146–3149, 2006.

[71] V. Vijayvargiya and S. K. Vishvakarma, "Effect of drain doping profile on double-gate tunnel field-effect transistor and its influence on device RF performance," *IEEE Trans. Nanotechnol.*, vol. 13, no. 5, pp. 974–981, 2014.

[72] V. P. Trivedi and J. G. Fossum, "Source/drain-doping engineering for optimal nanoscale FinFET design," in *2004 IEEE International SOI Conference (IEEE Cat. No. 04CH37573)*, 2004, pp. 192–194.

[73] K. K. Ng and W. T. Lynch, "Analysis of the gate-voltage-dependent series resistance of MOSFET's," *IEEE Trans. Electron Devices*, vol. 33, no. 7, pp. 965–972, 1986.

[74] D. Fleury, A. Cros, G. Bidal, J. Rosa, and G. Ghibaudo, "A new technique to extract the source/drain series resistance of MOSFETs," *IEEE Electron Device Lett.*, vol. 30, no. 9, pp. 975–977, 2009.

[75] G. J. Hu, C. Chang, and Y.-T. Chia, "Gate-voltage-dependent effective channel length and series resistance of LDD MOSFET's," *IEEE Trans. Electron Devices*, vol. 34, no. 12, pp. 2469–2475, 1987.

[76] S. Natarajan, M. Agostinelli, S. Akbar, M. Bost, A. Bowonder, V. Chikarmane, S.

Chouksey, A. Dasgupta, K. Fischer, and Q. Fu, “A 14nm logic technology featuring 2 nd-generation finfet, air-gapped interconnects, self-aligned double patterning and a 0.0588 μm 2 sram cell size,” in *2014 IEEE International Electron Devices Meeting*, 2014, pp. 3–7.

[77] K. Chen, H. C. Wann, J. Duster, D. Pramanik, S. Nariani, P. K. Ko, and C. Hu, “An accurate semi-empirical saturation drain current model for LDD N-MOSFET,” *IEEE Electron Device Lett.*, vol. 17, no. 3, pp. 145–147, 1996.

[78] J. B. Roldan, F. Gamiz, J. A. Lopez-Villanueva, and P. Cartujo-Cassinello, “Deep submicrometer SOI MOSFET drain current model including series resistance, self-heating and velocity overshoot effects,” *IEEE Electron Device Lett.*, vol. 21, no. 5, pp. 239–241, 2000.

[79] W. Xiong and J. P. Colinge, “Self-aligned implanted ground-plane fully depleted SOI MOSFET,” *Electron. Lett.*, vol. 35, no. 23, pp. 2059–2060, 1999.

[80] H.-S. Wong, D. J. Frank, and P. M. Solomon, “Device design considerations for double-gate, ground-plane, and single-gated ultra-thin SOI MOSFET’s at the 25 nm channel length generation,” in *International Electron Devices Meeting 1998. Technical Digest (Cat. No. 98CH36217)*, 1998, pp. 407–410.

[81] A. Ortiz-Conde, F. J. G. Sanchez, P. E. Schmidt, and A. Sa-Neto, “The foundation of a charge-sheet model for the thin-film MOSFET,” *Solid. State. Electron.*, vol. 31, no. 10, pp. 1497–1500, 1988.

[82] H.-J. Park, P. K. Ko, and C. Hu, “A charge sheet capacitance model of short channel MOSFETs for SPICE,” *IEEE Trans. Comput. Des. Integr. circuits Syst.*, vol. 10, no. 3, pp. 376–389, 1991.

[83] Y. Taur, “On the Log-Linear Inversion-Charge Relation for MOSFET Modeling,” *IEEE Trans. Electron Devices*, vol. 69, no. 1, pp. 427–429, 2021.

[84] S. Sleva and Y. Taur, “The influence of source and drain junction depth on the short-channel effect in MOSFETs,” *IEEE Trans. Electron Devices*, vol. 52, no. 12, pp. 2814–2816, 2005.

[85] R. Murali and J. D. Meindl, “Modeling the effect of source/drain junction depth on bulk-MOSFET scaling,” *Solid. State. Electron.*, vol. 51, no. 6, pp. 823–827, 2007.

[86] G. G. Shahidi, D. A. Antoniadis, and H. I. Smith, “Indium channel implants for improved

MOSFET behavior at the 100-nm channel length regime," *IEEE Trans. Electron Devices*, vol. 36, no. 11, p. 2605, 1989.

[87] J.-C. Sun, Y. Taur, R. H. Dennard, and S. P. Klepner, "Submicrometer-channel CMOS for low-temperature operation," *IEEE Trans. Electron Devices*, vol. 34, no. 1, pp. 19–27, 1987.

[88] M. J. Van Dort, P. H. Woerlee, and A. J. Walker, "A simple model for quantisation effects in heavily-doped silicon MOSFETs at inversion conditions," *Solid. State. Electron.*, vol. 37, no. 3, pp. 411–414, 1994.

[89] Q. Xie, J. Xu, T. Ren, and Y. Taur, "A 2D analytical model for SCEs in MOSFETs with high-k gate dielectric," *Semicond. Sci. Technol.*, vol. 25, no. 3, p. 35012, 2010.

[90] K. E. Atkinson, *An introduction to numerical analysis*. John wiley & sons, 2008.

[91] J. C. Butcher, *Numerical methods for ordinary differential equations*. John Wiley & Sons, 2016.

[92] D. Gonze and D. T. Gillespie, "Numerical methods for Ordinary Differential Equations." Teaching activities [online]. Belgium: Université Libre de Bruxelles, 2013.

[93] R. Alexander, "Solving ordinary differential equations I: Nonstiff problems (E. Hairer, SP Norsett, and G. Wanner)," *Siam Rev.*, vol. 32, no. 3, p. 485, 1990.

[94] H. Ernst and W. Gerhard, "Solving ordinary differential equations II: Stiff and differentialalgebraic problems." Springer-Verlag, New York, 1996.

[95] R. L. Burden, J. D. Faires, and A. M. Burden, *Numerical analysis*. Cengage learning, 2015.

[96] D. V. Griffith and L. M. Smith, "Numerical Methods for Engineers: A Programming Approach." Blackwell, Oxford, UK, 1991.

[97] A. H.-D. Cheng and D. T. Cheng, "Heritage and early history of the boundary element method," *Eng. Anal. Bound. Elem.*, vol. 29, no. 3, pp. 268–302, 2005.

[98] R. Bulirsch, J. Stoer, and J. Stoer, *Introduction to numerical analysis*, vol. 3. Springer, 2002.

[99] M. R. Osborne, “On shooting methods for boundary value problems,” *J. Math. Anal. Appl.*, vol. 27, no. 2, pp. 417–433, 1969.

[100] R. J. LeVeque, “Finite difference methods for differential equations,” *Draft version use AMath*, vol. 585, no. 6, p. 112, 1998.

[101] G. D. Smith, *Numerical solution of partial differential equations: finite difference methods*. Oxford university press, 1985.

[102] D. M. Causon and C. G. Mingham, *Introductory finite difference methods for PDEs*. Bookboon, 2010.

[103] C. Grossmann, H.-G. Roos, and M. Stynes, “Finite Difference Methods,” *Numer. Treat. Partial Differ. Equations Transl. Revis. by Martin Stynes*, pp. 23–124, 2007.

[104] A. Gil, J. Segura, and N. M. Temme, *Numerical methods for special functions*. SIAM, 2007.

[105] C. T. Kelley, *Solving nonlinear equations with Newton’s method*. SIAM, 2003.

[106] P. Deuflhard, *Newton methods for nonlinear problems: affine invariance and adaptive algorithms*, vol. 35. Springer Science & Business Media, 2005.

[107] A. M. Mathai, *Jacobians of matrix transformation and functions of matrix arguments*. World Scientific Publishing Company, 1997.